WEATHER AND DISPERSION MODELING OF THE FUKUSHIMA DAIICHI NUCLEAR POWER STATION ACCIDENT

A DISSERTATION SUBMITTED TO THE GRADUATE DIVISION OF THE UNIVERSITY OF HAWAIʻI AT MĀNOA IN PARTIAL FULFILLMENT OF THE REQUIREMENTS FOR THE DEGREE OF

DOCTOR OF PHILOSOPHY

IN

METEOROLOGY

December 2013

By

Thomas J. Dunn

Dissertation Committee:

Steven Businger, Chairperson
Gary M. Barnes
John N. Porter
Yuqing Wang
Mark A. Merrifield

ACKNOWLEDGMENTS

It is a pleasure to have reached the plateau in my Ph.D. program where I can express my gratitude to my committee, colleagues, family, and friends for their support and encouragement. I would like to offer my sincere thanks to Prof. Steven Businger for his enthusiastic support of my research goals and his patient guidance and collegial spirit in helping make them a reality over the long duration of my studies. I would like to thank Prof. Gary Barnes for his conscientious help and guidance in the preparation of my dissertation, but also for the knowledge I gained from his lectures as well as for many enjoyable conversations. I would also like to thank Prof. Yuqing Wang and Dr. John Porter for their reasoned insights and suggestions on the details of my numerical simulations and Prof. Mark Merrifield for his encouragement and support. At SOEST, I would like to thank Alex W. L. Lee for his help with the many administrative tasks associated with my program and Nancy Hulbirt for expertly preparing my figures.

It is indeed a pleasure to have the opportunity to thank Dr. David Bacon for his constant encouragement and support of my graduate studies and to my colleagues past and current at the Center for Atmospheric Physics for their help and friendship.

I would like to thank Prof. Asanobu Kitamoto and Dr. Jason Milbrandt for graciously sharing the fruits of their labor in the form of observational data and numerical algorithms that made this research possible. Dr. Genki Katata and Dr. Andreas Stohl are thanked for helpful comments during the course of my research.

Lastly, I can only sigh when I think of the many words of encouragement and support from my friends and family that have sustained me over the years. To my wife Elaine, my love and respect for her patience and understanding.

ABSTRACT

Contamination due to the surface deposition of radioactive material from the accident at the Fukushima Daiichi nuclear power station was investigated for 11 March to 17 March 2011. A coupled weather and dispersion modeling system was developed and simulations of the accident performed using two independent source terms that differed in emission rate and height and in the total amount of radioactive material released. Results show significant differences in the distribution of cumulative surface deposition of ^{137}Cs due to wet and dry removal processes. Parameterizations for precipitation scavenging by rain, snow, and graupel were implemented to investigate surface wet deposition fields . Results show aerosols from a source term with emission heights at 50, 300, and 1000 meters above ground level (AGL) were scavenged by rain (70%) and graupel (30%) compared with a source term with emission heights at 20 and 120 meters AGL in which material was scavenged preferentially by rain (95%). A sensitivity study was performed that broadened the particle size distribution (PSD) of the source terms during explosive events of the accident. Results for the source term with elevated emission heights show enhanced wet deposition due to scavenging by snow (5%, 35%, 51%) compared with scavenging by rain and graupel as the effluent PSD was increased (0.5, 1.0, and 10 μm, respectively). In contrast, the source term with relatively lower emission heights remained preferentially scavenged by rain (90%). A second study that investigated the complexity of the cloud microphysics scheme showed that precipitation scavenging of radioactive material was not very sensitive to the choice of single- vs. double-moment cloud microphysics parameterization. A comparison of ^{137}Cs deposition predicted by the

model with aircraft observations of surface-deposited gamma radiation showed reasonable agreement in surface contamination patterns during the dry phase of the accident. During the wet phase the pattern is not as well predicted. It is suggested that this discrepancy is because of differences between model predicted and observed precipitation distributions. Dry deposition was the dominant removal process, accounting for the majority of surface contamination (1–2 orders of magnitude over that due to wet deposition near the source).

TABLE OF CONTENTS

LIST OF TABLES

LIST OF FIGURES

CHAPTER 1. INTRODUCTION

1.1 Background

Following the 11 March 2011 Great East Japan Earthquake and Tsunami, the accident at the Fukushima Daiichi nuclear power station in Japan released a large amount of radioactive material to the atmosphere over a period of several months. Radioisotopes were dispersed circumglobally over the Northern Hemisphere by the end of March (Hsu et al. 2012). Nevertheless, a large fraction of radioactive debris was deposited on the surface adjoining the power station and over neighboring land, coastal, and off-shore areas of eastern Honshu during the first week of the accident (Chino et al. 2011).

In Japan the consequences of the accident comprised airborne and surface-deposited radionuclide concentrations much greater than background levels. In Fukushima prefecture, effective radiation doses estimated for the first year after the accident ranged from 1 to 10 milliSievert (mSv)[1], with localized maxima ranging from 10 to 50 mSv (World Health Organization [WHO] 2012). Prefectures neighboring Fukushima experienced effective doses in the range 0.1−10 mSv, whereas all other land areas in Japan that reported radioactivity from the accident were estimated to have received doses ranging from 0.1 to 1.0 mSv (WHO 2012). Gamma radiation, measured in kiloBecquerels per square meter ($kBqm^{-2}$)[2], from surface-deposited radioisotopes of iodine, tellurium, and cesium was observed in the coastal prefectures of Ibaraki and

[1] The Sievert (Sv) is a derived unit of measurement in the International System of Units (SI) for dose equivalent (J/kg) which expresses the biological damage to living tissue resulting from exposure to radiation; Nuclear Regulatory Commission (NRC) 2013.
[2] The Becquerel (Bq) is a derived unit of measurement in the SI for radioactivity (s^{-1}) denoting the rate of ionizing radiation released during the radioactive decay of an unstable atom; NRC 2013.

Fukushima (Figure 1.1) and has been associated with episodes of onshore flow (Katata et al. 2012a; Katata et al. 2012b).

Of the radioisotopes that were released during the accident, this study focuses on the atmospheric dispersion of cesium. Cesium (Cs) is an element that exists naturally and in low concentrations in the earth's crust as the stable isotope ^{133}Cs. In contrast, the radioactive isotope ^{137}Cs (radiocesium) is produced as a fission product during nuclear weapons tests and in the normal operation of nuclear power reactors. Uncontrolled releases of radiocesium that occur during accidents at nuclear power plants have the potential to cause widespread contamination. The half life of ^{137}Cs is 30.17 years, thus environmental contamination by radiocesium results in a persistent source of ionizing radiation. For example, within the exclusion zone surrounding the damaged Chernobyl nuclear power facility, it is estimated that environmental contamination by ^{137}Cs will be present for approximately 300 years (NEA 2002).

The health hazards of ^{137}Cs are not due to the toxicity of elemental cesium *per se*, but instead to the exposure of living tissue (internal and external) to ionizing radiation in the form of beta and gamma rays that are emitted by ^{137}Cs during radioactive decay (Agency for Toxic Substances and Disease Registry [ATSDR] 2004). Toxicological and epidemiological studies of acute exposure to ^{137}Cs are limited to a few documented incidents. The most notable incident occurred in 1987 in Goiania, Brazil where a number of people suffered acute radiation poisoning, including four deaths, due to external and internal exposures of up to 10 Sv hr^{-1} from a discarded medical source of $^{137}CsCl$ (ATSDR 1999).

Since the accident at the Fukushima Daiichi nuclear power station, progress has been made in estimating source terms of ^{137}Cs released to the atmosphere. However, important issues remain concerning the particle size distribution (PSD), the release rate and height of the radioactivity, and the relative contributions of wet and dry deposition processes on the surface distribution of radioactive material observed in Japan and the Northwest Pacific.

Previous studies of the Fukushima accident have produced two independent source terms that differ primarily in the time-dependent emission rate of the total radioactivity released during the accident. However, because the radioactivity was released in an uncontrolled and unmonitored manner, the estimated source terms of necessity relied on the use of dispersion models to reconstruct the release. Unfortunately, modeling the dispersion of radioactive material of unspecified composition and PSD that is released into a turbulent boundary layer of variable atmospheric stability from intermittent buoyant sources presents many challenges. That the plumes may disperse in the presence of precipitation and under the dynamical influence of local circulations and synoptic scale motions adds complexity because parameterizations for cloud microphysics and boundary layer physics are required to accurately model the temporal and spatial distributions of the precipitation and radioactivity fields.

Since the physical complexity and numerical resolution of dispersion models can vary, it is important to identify and understand how differences in model formulations translate to differences in the predicted radiological consequences of the event. For example, dispersion model predictions aimed at radionuclide transport on the global scale are integrated over time at relatively lower model grid spacing and often with less

physical detail than high-resolution mesoscale and cloud scale models applied to smaller geographic areas. The difference in grid spacing is important in resolving the underlying terrain and physical processes in the boundary layer that govern the transport and diffusion of the radioactive material.

The difference in grid spacing also affects the formation and distribution of precipitation since the saturation of water vapor, which is parameterized at relatively larger scales, is modeled explicitly as grid spacing is reduced to convection-permitting and convection-resolving scales. Precipitation scavenging, which together with dry deposition represent first-order processes controlling the amount of radioactive material reaching the surface, depends on the spatial and temporal accuracy of precipitation, whether obtained as a model prognostic variable or ingested from an analysis dataset.

While previous studies of the Fukushima accident point to the role of precipitation scavenging on the surface deposition field, wet deposition due to rain or an estimate thereof (e.g., model layers with relative humidity above a threshold amount) has received the most attention; hence, it is not clear whether precipitation type (e.g., rain, snow, graupel) was a factor in the surface deposition of radioactive material. Given that snow was observed intermittently at the surface in the vicinity of the accident and in the prefectures to the west and north of the accident, a determination of the role of scavenging by frozen precipitation is warranted and is addressed in this study.

Previous studies have constructed source terms for radioisotopes of xenon, iodine, and cesium based on an estimated chronology of the Fukushima accident and in particular assigned time-varying release heights around the observed explosions and fires at the facility. However, in the case of particle-bound radioisotopes (e.g., iodine and

cesium), the PSD of the modeled release in these studies was held constant for explosive and non-explosive periods of the accident. Thus, it is not clear whether changes in the PSD of aerosols accompanying explosive periods and fires had an influence on the character of the surface deposition field.

This study investigates the influence of using different source terms on the resulting surface deposition of radioactive material observed in Japan and the Northwest Pacific using a numerical weather prediction model coupled with a numerical model of atmospheric dispersion that has been enhanced with parameterizations of wet and dry removal processes. The study will highlight the differences in surface deposition fields obtained using two published source terms and will examine the sensitivity of the model predictions to changes in the PSD of the precipitation and radioactivity fields. A specific goal of the study is to construct an atmospheric modeling system to simulate the radioactive material released from the Fukushima accident and to compare the modeled surface deposition pattern with observations. The study will lead to a better understanding of the radiological consequences of the Fukushima accident and the atmospheric processes that governed the dispersal and surface deposition of the radioactive material.

The remainder of this chapter will discuss dispersion modeling in the context of nuclear reactor accidents before describing the objectives of the study and some methodology of the numerical experiments. Chapter 2 provides details of the models and model setups that were used for the study. Results from the model experiments are presented in Chapter 3. Chapter 4 is a summary that discusses the implications of the study and plans for future work.

That natural phenomena such as earthquakes, flash floods, and tornadoes could conceivably result in damage to a nuclear power rector to such an extent as to cause an uncontrolled release of radioactive material to the atmosphere was recognized in the early years of the U.S. atomic energy industry (U.S. Weather Bureau 1955). However, as the number, operators, types, and especially power levels of nuclear reactors continued to increase, the potential contamination hazard resulting from effluents released during normal operations and in the event of accidents spurred the development of specialized analytical tools to manage and assess impacts (Slade 1968). A key capability involved the creation of computer models to predict the transport and rate of diffusion, collectively the atmospheric dispersion of radioactive material.

Dispersion is an integral process of the atmospheric system and is active on spatial and temporal scales ranging over four orders of magnitude, from microscale to global. In the atmosphere, dispersion typically refers to a combination of the processes of advection and diffusion acting on an effluent and may include chemical transformations and removal mechanisms. The magnitude of turbulence kinetic energy (TKE) largely determines the mixing rate of an effluent (Pasquill 1974, Stull 1988), with the balance between the production of TKE by wind shears and convective motions and the destruction of TKE by viscous dissipation governed largely by the stable and unstable stratification of the boundary layer (Wyngaard 2010).

Models of atmospheric dispersion based on gradient transport, statistical, and similarity theories, in conjunction with diffusion data from field experiments (e.g., Barad 1958), led to the development of Gaussian plume computer models, used to predict effluent air concentrations with respect to fixed plume centerlines under uniform and

steady-state meteorological conditions (Arya 1999). Gaussian plume models exhibited skill in predicting the dispersion of effluents at relatively close-in distances and short time intervals over idealized surfaces and under stationary and horizontally homogeneous atmospheric conditions (Hanna 1982). Hence these models were limited in scope and applicability with respect to nuclear accident response. However, as knowledge of atmospheric dispersion progressed and computing power increased, Gaussian plume models were superseded by Gaussian puff models (e.g., Heffter 1975) and coupled particle-in-cell trajectory/mass-consistent wind models (e.g., Lang 1978). These models increased the level of sophistication of dispersion calculations by applying time-varying meteorological conditions to particle transport in a Lagrangian frame of reference, which increased the accuracy of the predicted activity gradients and extended the range of applicability from site-specific to long-range transport problems.

Recently, the ability to predict the movement, rate of diffusion, and removal of airborne radionuclides has been improved through the application of full-physics mesoscale models to the problem of atmospheric dispersion. Numerical weather prediction models coupled with Lagrangian dispersion has the capability to resolve the collective effects of evolving weather over complex terrain on plume characteristics and downwind activity concentrations (e.g., Boybeyi et al. 2001).

In a fully prognostic approach a mesoscale model can be augmented by the addition of an embedded particle/puff dispersion model, enabling transport and diffusion calculations at the temporal resolution of the mesoscale model's time step. A second approach (e.g., Draxler and Hess 1998; Stohl et al. 2005) ingests mesoscale model output

at fixed intervals to provide meteorological fields as input for a particle/puff dispersion model operating as a post processor.

Despite advances in computing power over the years, the mode of operation in which the Lagrangian frame of reference particle/puff model serves as a post processor of the mesoscale simulation output remains the preferred means to simulate atmospheric dispersion problems such as the accidental release of radioactive material. This preference is due to the fidelity with which source term configurations can be accommodated, the ease with which the Lagrangian framework can be adapted to a range of modeling scales (e.g., computational fluid dynamics [CFD], large eddy simulation [LES], cloud-scale, mesoscale, and global models), and ultimately, the computational balance that may be achieved between accuracy and efficiency.

Although the post processing approach is computationally efficient, the accuracy of the resulting dispersion and surface deposition calculations can be sensitive to the time interval that is used to feed meteorological data from the weather or climate model to the dispersion model. For example, Korsholm et al. (2009) showed that the choice of coupling interval could be a factor in resolving the influence of mesoscale disturbances and eddies on evolving plume structure, whereas Grell et al. (2004) showed that convective-scale vertical mixing could be constrained by the choice of coupling interval.

Nonetheless, the flexibility afforded source term specification, together with the Lagrangian puff model's capability to preserve gradients in tracer concentrations owing to minimal numerical diffusion compared with Eulerian frame of reference dispersion models (Lin et al. 2011), has favored the use of particle/puff models driven by mesoscale model output. This preference has resulted in the application of the Lagrangian puff

model to a diverse set of atmospheric dispersion problems ranging from the small-scale release of a dense gas (e.g., Sykes et al. 1999) to the relatively large-scale release of volcanic effluents (e.g., Hollingshead et al. 2003) and is the dispersion modeling approach used in this research.

The downwind concentration of radioactive material and deposited surface dose depends on the nature and stage of the accident, the height and total length of time of the release, atmospheric conditions, topography, vegetation and land use patterns, the relative distance from the source, and the amount and type of nuclides released (Kramer and Porch 1990). A prediction of the expected dose from a damaged nuclear power reactor is important for consequence decisions associated with emergency planning and preparedness and can be used to guide response activities such as the positioning of monitoring sensors and the relocation of population groups (Engleman and Wolff 1990).

In the recovery and analysis stage of an accident, an accurate map of the observed distribution of the deposited radioactive material provides a foundation for determining environmental and health impacts, estimating and refining the source term comprising the quantities of radionuclides released, and assessing the impact from future hazards such as the resuspension potential due to wind erosion or wildfire.

Historically, atmospheric radioactivity has been divided into three fields of study: 1) natural radioactivity in the troposphere resulting from radioactive elements released from the Earth's surface, principally emissions of radon isotopes and their progeny; 2) natural radioactivity generated in the upper troposphere and lower stratosphere resulting from the interaction of cosmic rays with atmospheric constituents; and 3) anthropogenic

radioactivity released through the troposphere and lower stratosphere from nuclear weapons tests (Junge, 1963; Sykora and Froehlich 2009).

Accidental releases of radioactive material have occurred from a diverse group of sources including nuclear, industrial, academic, research, and medical facilities as well as from transport accidents involving ships, submarines, aircraft, and spacecraft. In addition, several serious accidents at nuclear facilities over the past 60 years have been documented, of which seven caused off-site releases of radioactive material with potential for significant population exposures (United Nations Scientific Committee on the Effects of Atomic Radiation 2008). Hence, the traditional fields of study of atmospheric radioactivity have of necessity adapted to accommodate accidental releases of radioactive material. Among all reactor accidents prior to Fukushima, the accidents at Windscale in the United Kingdom and Chernobyl in the former Soviet Union are the most notable due to the resulting widespread dispersion of radioactive material and the extent to which the accidents were, and continue to be, assessed using atmospheric dispersion model simulations.

The Windscale works of the United Kingdom Atomic Energy Authority, formerly a plutonium production facility for military purposes located on the Cumberland coast of northwest England, was the site of the first major release of radioactive material from a damaged reactor (Eisenbud and Gesell 1997). The accidental release of fission products accompanied an intense fire that consumed 120 of the 3,440 graphite core fuel channels in Pile 1 during the period 10 to 11 October 1957 (Arnold 1992). The graphite pile that was used to moderate the fission process was of an air-cooled design that vented to the atmosphere through a filtered 120-m stack, hence significant releases of radioactivity

occurred as burning of the uranium fuel intensified over time and also after the pile was flooded with water to extinguish the flames (Arnold 1992).

Chamberlain (1959) assessed the resulting variation of measured surface activity deposition and noted that maxima in the fallout of ^{131}I and ^{137}Cs occurred within a narrow strip extending southeastward along the coastline. He attributed the narrow band to increased emissions, turbulence, and rainfall that may have accompanied the observed passage of a weak cold front over the accident site, but also hypothesized enhanced deposition resulting from the possible interaction of the Windscale plume with a cooling tower plume from a additional nearby power station. Stewart and Crooks (1958) extended the analysis of the airborne radioactivity to Western Europe and implicated a dry deposition pathway for surface contamination over southern England.

Crabtree (1959) combined measurements of ^{131}I air concentrations with a meteorological trajectory analysis to determine the spread of the radioactive cloud over the United Kingdom and Europe and deduced the amount of radioactive material released. His analysis showed the plume to be widely dispersed by the passage of a weak cold front over the accident site during the time of the accident.

Early modeling studies based on a Gaussian plume formulation of the Windscale release by Clarke (1974) reproduced the measured dispersion observations over short range distances of 50 km and provided the first model estimates of the quantity of radioisotopes released. ApSimon et al. (1985) used a Lagrangian puff dispersion model initialized with a dense array of surface and upper air meteorological data to extend the analysis of the radioactive plume across central and southern England to the European continent. The ApSimon et al. (1985) study was an important milestone in the use of

Lagrangian models applied to reactor accidents because it was able to verify model predictions of observed surface activity concentrations with long-range trajectories of the plume constructed from weather maps. More recently, Johnson et al. (2007) used a Lagrangian particle dispersion model forced by ERA-40 reanalysis data and coupled with the current best estimate of the radioactivity emissions profile to simulate the long-range dispersion of the Windscale plume. This work showed the impact of improved meteorological data in reducing uncertainties of the plume's behavior, albeit excluding the process of precipitation scavenging.

The Chernobyl power complex, comprising four graphite-moderated light-water reactors, is located approximately 125 km northwest of Kiev, Ukraine, near the border with Belarus. The complex became the source of a catastrophic trans-boundary nuclear accident during April and May 1986 when a test to determine whether cooling of the Unit 4 reactor could be maintained in the event of a loss of station power caused an uncontrolled power surge and explosions that destroyed the reactor core (Nuclear Energy Agency [NEA] 2002). The explosion lofted structural debris, radioactive gases and aerosols, and fragmented reactor fuel to the mid-troposphere (Gudiksen et al. 1989) and exposed the core of the reactor to the atmosphere. The momentum and buoyancy rise associated with the exposed core and a subsequent fire in the graphite moderator combined to produce a continuous source of radioactive particulates over roughly a ten-day period that was dispersed and deposited over Europe and throughout the Northern Hemisphere (De Cort et al. 1998).

ApSimon and Wilson (1987) assessed the dispersion of the Chernobyl radionuclides over Europe using a Lagrangian trajectory model initialized and integrated

with routine synoptic weather observations. Their work showed the importance of estimating the magnitude and time history of the release based on a knowledge of the radionuclide inventory in the reactor at the time of the explosion and fire. Using a Eulerian model to assess hemispheric transport, Pudykiewicz (1988) noted the need for a parameterization for precipitation scavenging, including the provision of variable scavenging rates. Results from the Atmospheric Transport Model Evaluation Study (ATMES) workshop (Klug et al. 1992) highlighted the need for improved characterization of the time-varying strength, height, and vertical distribution of the Chernobyl source term. The ATMES results were corroborated recently by Evangeliou et al. (2013) who showed the importance of the Chernobyl source term emission height on the dispersion and deposition of ^{137}Cs over Europe.

In modeling the atmospheric consequences of a nuclear reactor accident, the source term and the fidelity of the atmospheric simulation are the two factors that govern the accuracy of the predicted dispersion and deposition of the radioactive material. The source term defines the quantities of radionuclides released from the accident site over a period and serves as a principal input for any dispersion calculation. Key parameters associated with the source term are the composition and fractions of the radionuclides, the PSD, and the height of release. In a best-case scenario, all effluents released during an accident enter the atmosphere through stacks designed for this purpose, albeit likely with some measure of enhanced rise (the effective stack height) due to additional momentum and buoyancy caused by explosions, fires, and/or residual heating from the damaged core. In the Windscale accident, for example, radionuclides were vented from a 120-m stack attached to the reactor pile. In a worst-case scenario represented by the Chernobyl

accident, radioactive material is released directly to the atmosphere by fire and explosions.

The release of radioactive material from the Fukushima accident comprised characteristics of both release scenarios wherein unknown fractions of radionuclides were emitted simultaneously from 120-m stacks, diffused from the primary containment vessels, and lofted by fire and hydrogen explosions from within the containment buildings. The source term associated with such a complex release is not known accurately in time, space, or composition; thus, physically representative characteristics must be estimated or reconstructed.

A key characteristic of any source term composed of aerosols is the PSD since the aerosol PSD has a first order effect on the distribution of the fallout pattern. As a pretext to the discussion of the PSD that may be expected from a reactor accident, it is helpful to consider the PSD of the ambient aerosol occurring in both clean marine and polluted continental environments. In terms of surface area, the ambient aerosol is composed of three modes when differentiated by size for dry particles: 1) the nucleation mode (diameter $\leq$ ~0.1 μm), 2) the accumulation mode (~0.1 < diameter $\leq$ ~0.7 μm) , and 3) the coarse mode (diameter > ~ 0.7 μm; Porter and Clarke 1997).

Aerosols in the nucleation mode derive from gas-to-particle conversions, primary particle emissions, and the condensation of vapors (Seinfeld and Pandis 2006). The ubiquitous nature of the accumulation and coarse aerosol modes is due to naturally occurring processes in the atmosphere. The accumulation mode aerosols are maintained by the coagulation of nucleation mode aerosols into the accumulation mode, a decrease in the coagulation efficiency at larger sizes, gas-to-particle conversion, the lofting of coarse

mode aerosols by the ambient wind, and removal processes due to gravitational settling and scavenging by cloud and precipitation (Porter and Clarke 1997). The coarse mode aerosols (e.g., dusts, sea salt, spores, pollens, and bacteria) are produced through mechanical processes such as the action of wind on water, land, and vegetation surfaces, with the upper range of the size spectrum governed by gravitational settling (Twomey 1977).

An estimate of the particulate material and characteristic particle sizes expected from a reactor accident was described by Lewellen et al. (1983), from which the following description is taken: "Particulate material within the containment vessel will include radionuclides attached to atmospheric aerosols (submicron to a few microns), particles formed by homogeneous condensation of volatile species (submicron), larger particles formed by agglomeration of aerosols in regions of high concentrations (micron), water droplets formed in a steam environment using the smaller particles as condensation nuclei (10–20 μm), and some large particles produced due to possible fuel rod rupture (10–100 μm)" (p. 865).

After the Fukushima accident, two independent source terms that differ primarily in the time-dependent emission rate and height, as well as in the total amount of radioactive material released, have been published that are used in contemporary studies of the resulting surface contamination. The first study by Terada et al. (2012; hereinafter, the "Terada source term") refined and verified the earlier results of Chino et al. (2011) using an atmospheric dispersion system based on the MM5 mesoscale model running at a grid spacing of 3 km applied to a small region of northeast Japan. A second study by Stohl et al. (2012; hereinafter, the "Stohl source term") used an atmospheric dispersion

system based on three-hourly operational meteorological analysis data from the National Centers for Environmental Prediction (NCEP) Global Forecast System (GFS) to produce global estimates of the time-varying surface concentrations of ^{133}Xe and the total surface deposition of ^{137}Cs. Both studies produced estimates of the emission rate and release height of the radioactive material released during the accident. The present study uses the final emissions of aerosol-bound ^{137}Cs estimated by Stohl et al. (2012) and the revised emissions of aerosol-bound ^{137}Cs estimated by Terada et al. (2012), which are presented in Figure 1.2.

1.2 Objectives and methods

Radioactive releases represent a life-threatening hazard to local populations and the environment. Moreover, understanding and accurately predicting the dispersion of radioactive material can provide critical guidance to government agencies dealing with emergency response and mitigation. Motivated by the hazards from exposure to radioactive releases, the objectives of this study are to 1) construct a coupled weather and dispersion modeling system that can reproduce the observed pattern of surface contamination from the Fukushima accident; 2) compare the Terada and Stohl source terms results to help assess which is more realistic; and 3) perform studies on the cloud microphysics parameterization and aerosol PSD used in the source comparison study to assess the sensitivity of the model predictions.

This study is the first to compare the Terada and Stohl source terms using a common atmospheric modeling framework (i.e., use of identical weather simulations to drive the dispersion of different emissions estimates). Therefore, the main research questions are aimed at the prediction of the surface contamination: Do the model-

simulated surface deposition patterns agree with observed surface patterns? Are the simulated surface wet and dry deposition fields sensitive to differences in the source terms?

The surface deposition of radioactive material proceeds through wet and dry processes in the atmosphere. Motivated by early results from exploratory numerical weather simulations of the Fukushima accident by the author that suggested the presence of mixed-phase precipitation in the boundary layer, an additional aspect of this study is focused on differential precipitation scavenging of the radioactive plume by rain, snow, and graupel. This focus seeks to gauge the relative contribution of each type of precipitation to the total surface wet and dry deposition fields. The main research question of this inquiry is concerned with the distribution of the radioactive material that was deposited by wet removal processes: Does the distribution of the surface wet deposition field depend on whether the radioactive material of each source term was scavenged by rain, snow, or graupel? If so, in what proportions?

Since mixed-phase microphysics is requisite for modeling the formation and growth of graupel, the author implemented a multi-moment cloud microphysics parameterization in the weather model and a scavenging parameterization for the interaction of particles with rain, snow, and graupel fields in the dispersion model. The scavenging parameterization developed for this study depends on the mass-mean diameter of the modeled rain, snow, and graupel distributions. In turn, the rain, snow, and graupel distributions may depend in the aggregate on the choice of using a single-moment vs. a double-moment cloud microphysics scheme. Thus, a sensitivity study was performed with the goal of determining whether the modeled surface wet (and dry)

deposition fields are sensitive to the choice of using single-moment vs. double-moment descriptions of cloud microphysical interactions.

Lastly, although the Terada and Stohl source terms estimated the total amount and release rate and height of the radioactivity from the Fukushima accident, the aerosol PSD was not prescribed and hence is an independent parameter that should be tested for the range of effluent conditions present during the accident. The present study assumes that the radioactivity is partitioned among particle size bins using a log normal PSD. During the Fukushima accident, however, emissions were of a continuous nature punctuated by relatively brief explosive events and fires. Since explosions and fires have the potential to loft a relatively broader range of particle sizes to relatively greater altitudes, a second sensitivity study was completed to investigate the influence of changing the aerosol PSD of the plume during observed explosive events on the wet and dry surface deposition process.

Given a representative perturbation source term, the fidelity of the atmospheric simulation is the second factor that governs the dispersion and deposition of the radioactive material. Therefore, a viable simulation schema was required to span the six-day period of the initial atmospheric release of radioactivity from the Fukushima accident site. Numerical weather prediction is an initial-value problem which requires that the model provide a realistic representation of the atmosphere and its processes. Furthermore, initial conditions used to start the simulation should be known as accurately as possible to minimize the growth and propagation of errors (Kalnay 2003). Given the accuracy of the physical parameterizations used in the atmospheric model to simulate unresolved processes and the relatively sparse and incomplete meteorological information available

to determine the state of the atmosphere at the time of the accident, a single simulation integrated over six days at relatively high resolution would likely contain a large error component that would be reflected in the dispersion estimates.

To overcome this hurdle, the author developed a simulation schema comprising a series of short-duration (e.g., 30 hour) weather simulations that were used to create a relatively seamless input stream for the dispersion calculations. In this schema, each weather simulation was initialized at 00 UTC and run for 30 hours for each day of the six-day period March 11–16, 2011. The first 6 hours of each simulation was consigned to model spin up and discarded, hence the remaining 24 hours of each simulation comprised viable output fields for the dispersion simulations. After all of the weather simulations were completed, the viable output files from each simulation were linked together in succession to create 144 hours of continuous weather output for use in the dispersion model.

Next, a 144-hour dispersion model simulation was performed using 1) the linked weather output files that provided the interpolated wind and turbulence fields and 2) the time-varying source terms that provided the release rate and height of the radioactive material. With this schema, the release of radioactivity was not constrained by attempts to bound the explosive events of the accident with individual simulations; rather, the atmospheric release was continuous in time and space, commencing at 00 UTC 11 March 2011, before the first release of radioactivity and ending at 00 UTC 17 March 2011.

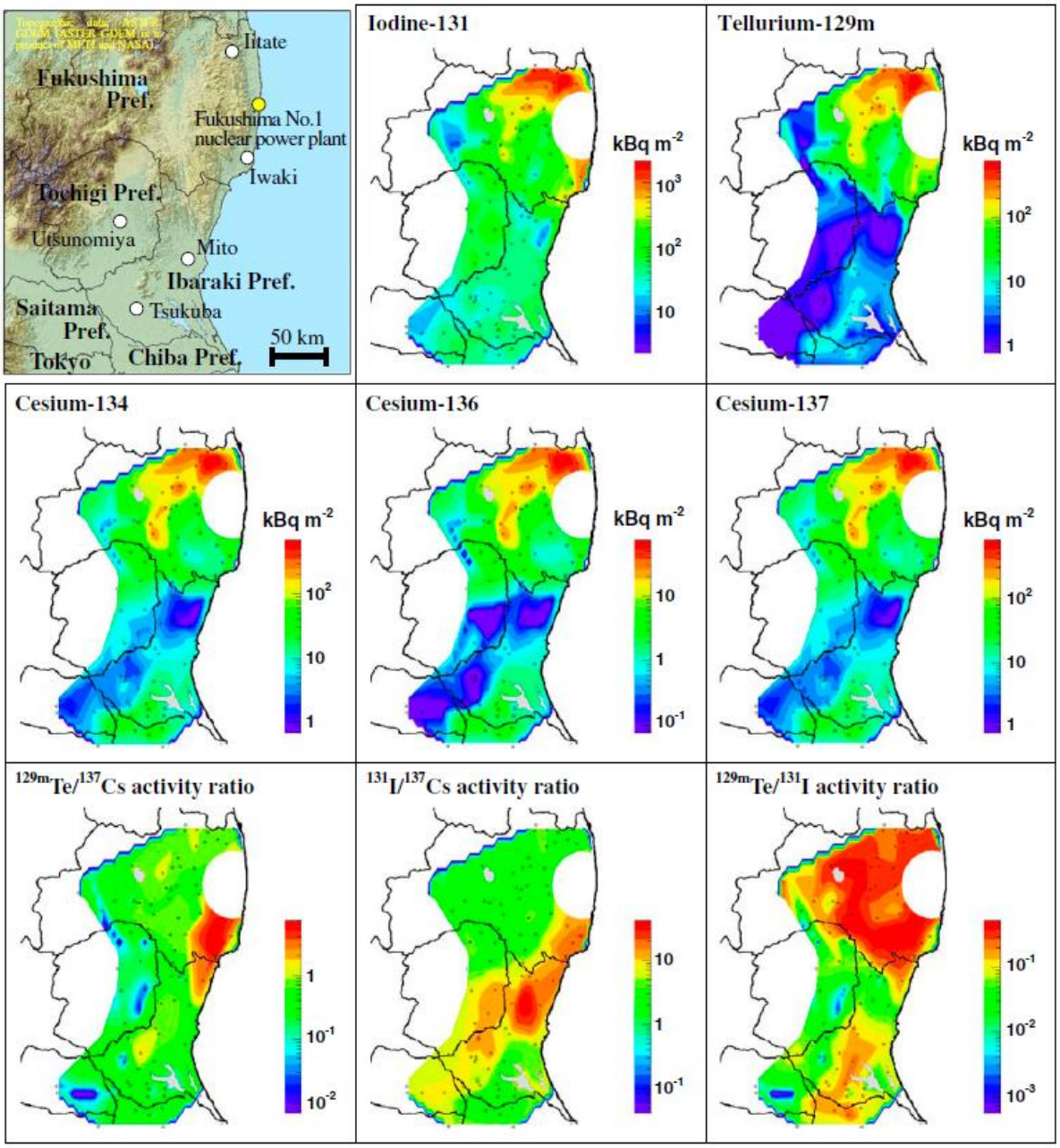

Figure 1.1 Geographic distribution of surface-deposited radioisotopes ($kBqm^{-2}$) and activity ratios in soil samples observed on 29 March 2011. White semicircle depicts 30 km evacuation/sheltering zone. Topographic map of the surveyed area is shown in the upper left hand corner (from Kinoshita et al. 2011).

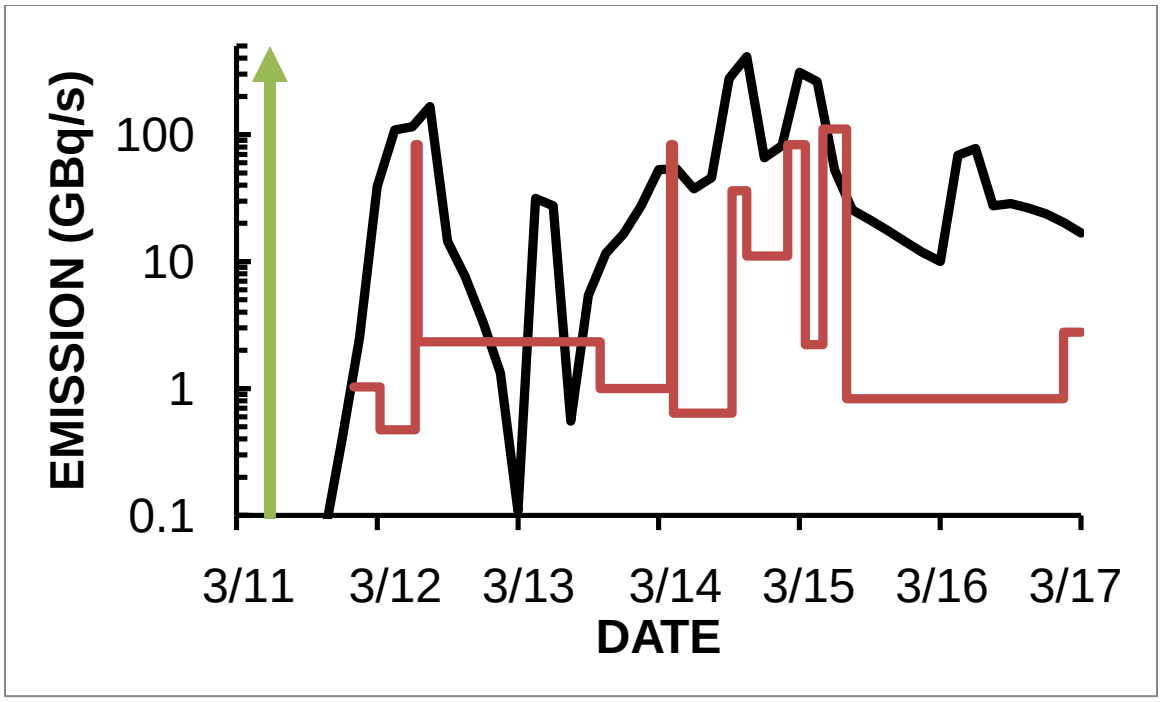

Figure 1.2 Emission rates (GBq/s) of ^{137}Cs estimated by Stohl et al. (2012) (solid black line) and Terada et al. (2012) (solid red line) for the period 00 UTC 11 March to 00 UTC 17 March 2011 comprising the source terms used for this study. Green arrow indicates the time of the earthquake. Adapted from Stohl et al. (2012) and Terada et al. (2012).

CHAPTER 2. MODEL AND DATA DESCRIPTIONS

2.1 Weather model

Weather simulations were performed with the Operational Multiscale Environment model with Grid Adaptivity (OMEGA), a numerical weather prediction system based on unstructured grid techniques. The governing equations and physical parameterizations of the OMEGA model were described in Bacon et al. (2000), whereas attributes and applications of the modeling system have been described in Boybeyi et al. (2001), Gopalakrishnan et al. (2002), Pielke (2002), Cox et al. (2003), Ahmad et al. (2006), Bacon et al. (2008), and Kaplan et al. (2009).

The model is based on a three-dimensional computational mesh composed of truncated triangular prisms referenced to a rotating Cartesian coordinate system (Figure 2.1) that accommodates horizontal grid spacing in the range ~1 km to ~100 km. The initial horizontal grid resolves fixed surface features (e.g., coastlines, terrain gradients) in a scale-spanning manner in which grid spacing varies continuously over the domain. In addition, the grid spacing can remain unchanged (static) or allowed to change automatically (dynamic adaptation) during the course of the simulation. The mesh is structured in the vertical dimension and terrain following, with a layer spacing that ranges typically from a few tens of meters in the boundary layer to ~1 km in the free atmosphere (Figure 2.2).

OMEGA is a nonhydrostatic model that uses a finite-volume flux-based numerical advection algorithm to advance the primitive equations over time. In addition, detailed physical parameterizations are used to model the time evolution of the planetary boundary layer, solar and terrestrial radiation, cumulus convection, and cloud

microphysical interactions. A schematic of the major components of the OMEGA modeling system is presented in Figure 2.3.

Simulation results were obtained using OMEGA version 9.1.2, but with the following improvements implemented by the author for this research. First, the Anthes-Kuo cumulus parameterization (Anthes 1977) was replaced with a version of the Tiedtke cumulus parameterization developed by Zhang et al. (2011). Second, the single-moment bulk-water cloud microphysics parameterization based on Lin et al. (1983), but originally implemented in OMEGA (Bacon et al. 2000) such that liquid and solid phases of water were not allowed to coexist, was replaced with the double-moment, mixed-phase, bulk-water cloud microphysics parameterization developed by Milbrandt and Yau (2005).

2.2 Dispersion model

A model was developed by the author to simulate the dispersion of radioactive material accompanying the evolving weather fields produced by the OMEGA simulations. The dispersion model is a post processor implementation of OMEGA's embedded atmospheric dispersion model and has the following attributes: 1) Meteorological output at constant time intervals from an OMEGA simulation representing the effects of transport by the mean wind and diffusion due to turbulent velocity fluctuations is used to disperse the effluent. 2) Lagrangian turbulence statistics are combined with a Gaussian puff formulation of the effluent to produce time-dependent surface concentration and deposition fields. 3) All meteorological fields that interact with the Gaussian puffs (e.g., dynamical, thermodynamical, turbulence, and microphysical) are interpolated linearly in time between successive OMEGA output files. 4) The dispersion model uses the same unstructured mesh that was used in the OMEGA

simulation. 5) The dispersion model is fully parallelized with the Message Passing Interface (MPI) and employs domain decomposition in which each processor controls a single subdomain. 6) The dispersion model time step is determined by the CFL (Courant-Friedrichs-Lewy) restriction on the interpolated wind field. 7) The material properties of Gaussian puffs (e.g., location, height, time, and interval of release, puff volume, particle density, diameter, and radioactive decay rate) are pre-specified in an input data file, which contains an entry for each puff injection source term. 8) Gaussian puffs are allowed to fall relative to the surface at their size-dependent gravitational settling velocities. 9) A surface resistance model for particulate material based on Seinfeld and Pandis (2006) was implemented by the author and is used for the calculation of dry deposition. 10) A precipitation scavenging model for particulate material was adapted from Slinn (1984) by the author and is used to facilitate the calculation of wet deposition by rain, snow, and graupel.

Radioactive material released to the atmosphere is modeled using a Gaussian puff approach in which the radionuclides are partitioned among a collection of puffs of prescribed initial volume. Over time, each puff expands as it is advected by the mean wind field. Advection of the puff centroid is governed by resolved components of the interpolated wind field while diffusional growth about the centroid reflects the unresolved effects of turbulence following the methodology of Uliasz (1990). At any given instant in time, the radioactivity concentration in each puff is assumed to follow a Gaussian distribution in each of three component directions, x, y, and z, with the mean square distance to which the activity has diffused represented by the respective standard deviations of the distribution (Arya 1999).

The PSD for the Fukushima ^{137}Cs source term is unknown, hence a log normal PSD was used in this study. A log normal PSD was chosen given the preponderance of log normal PSDs observed and modeled in studies of Light Water Reactor (LWR) severe accident conditions (NEA 2009), a similar PSD used in Stohl et al. (2012), and activity size distributions observed during the accident (Kaneyasu et al. 2012) and under background conditions (El-Hussein and Ahmed 1994). The log normal PSD is represented in the dispersion model by a discrete number of size bins. Each size bin is characterized by a representative particle diameter, d_p, so that the mass or activity distribution as a function of diameter is:

$$\rho_{mass}(\mathrm{d}_p) = \frac{1}{\sqrt{2\pi}\ln\sigma_g}\exp\left[-\frac{1}{2}\left(\frac{\ln(\mathrm{d}_p/\mathrm{MMD})}{\ln\sigma_g}\right)^2\right] \qquad (2.1)$$

where σ_g is the geometric standard deviation and MMD is the mass mean diameter. The bounded log normal distribution:

$$\int_{d1}^{d2}\rho_{mass}dd_p = \frac{1}{2}\left(erf\left(\frac{\ln\left(d_2/MMD\right)}{\sqrt{2}\ln\sigma_g}\right) - erf\left(\frac{\ln\left(d_1/MMD\right)}{\sqrt{2}\ln\sigma_g}\right)\right) \qquad (2.2)$$

represents the fractional mass of particles between d_1 and d_2 and is used to partition the total released mass or radioactivity among individual size intervals. Each size interval is characterized by a representative particle size, d_p, which is the geometric mean diameter of the size bin. Thus, given an amount of mass or radioactivity released during some discrete time interval, a collection of puffs of prescribed volumes and material properties, each characterized by a unique particle size, are initialized to model the resulting plume of material.

In the absence of precipitation, particulate material is removed from the atmosphere explicitly by gravitational settling, which depends on the terminal settling velocity of the representative particle size:

$$v_t(\mathrm{d}_p) = \frac{d_p^2 \rho_p g C_c}{18\mu} \tag{2.3}$$

where ρ_p is the particle density, g is the acceleration due to gravity, μ is the viscosity of air, and C_c is a slip correction factor for particles, which becomes important as the particle diameter approaches the mean free path of air molecules (Seinfeld and Pandis 2006).

In this study, the minimum aerosol diameter size is 0.14 μm, hence settling speeds are very small and dry deposition from Gaussian puffs is also modeled implicitly following a surface resistance formulation for particulate material that is based on the work of Seinfeld and Pandis (2006). This approach is used to calculate surface radioactivity concentrations resulting from unresolved processes for surface interaction such as impaction and transfer by turbulent eddies to surface elements and is expressed in terms of a deposition velocity:

$$v_d(\mathrm{d}_d) = \frac{F_d}{X_d} \tag{2.4}$$

where F_d represents the vertical dry deposition flux and X_d is the concentration of material or activity in a puff. The deposition velocity is calculated assuming a resistance model described by:

$$v_d(\mathrm{d}_p) = \frac{1}{r_a + r_b + r_a r_b v_t(\mathrm{d}_p)} + v_t(\mathrm{d}_p) \tag{2.5}$$

Where r_a represents an aerodynamic resistance associated with turbulent transport through the surface layer to the quasi-laminar sublayer adjacent to the underlying surface, and r_b represents a resistance associated with Brownian diffusion of material through the sublayer to the surface. Finally, the amount of material that is removed from a puff and deposited on the surface in a time step, Δt, is:

$$m(\mathrm{d}_p) = m(\mathrm{d}_p)\left(1 - \exp\left(\frac{-v_d \Delta t}{Z_{agl}}\right)\right) \tag{2.6}$$

where Z_{agi} is the altitude of the puff above the surface. In this study, the dry deposition model was active for puffs with centroid altitudes (AGL) that were below a threshold distance of 100 m AGL from the surface.

When hydrometeors (e.g., cloud drops, cloud ice, rain, snow, graupel, hail) are present and collocated with airborne particulate material, the particulates may be removed from the atmosphere by wet deposition pathways. Two pathways that are usually differentiated with respect to cloud base are in-cloud or nucleation scavenging and below-cloud or impaction scavenging. Nucleation scavenging includes the processes of deposition, condensation followed by freezing, immersion, and contact nucleation for primary ice particles and heterogeneous nucleation by cloud drops. Brownian diffusion, thermophoresis, diffusiophoresis, and electrical charging effects can also influence the process of nucleation scavenging (Pruppacher and Klett 1980; Rogers and Yau 1989).

In this study, precipitation scavenging is restricted to impaction scavenging by rain, snow, and graupel, with the stipulation that this scavenging process is active wherever these species are collocated with aerosol puffs; precipitation scavenging is not

confined to altitudes below cloud base. Electrical charging effects and the processes of thermophoresis and diffusiophoresis are ignored.

In the process of impaction scavenging of particles by precipitation, the rate of removal of particulates of diameter d_p and size distribution n_p:

$$\frac{dn_p(\mathrm{d}_p)}{dt} = -\lambda(\mathrm{d}_p)n_p(\mathrm{d}_p) \tag{2.7}$$

is a function of the scavenging coefficient:

$$\lambda(\mathrm{d}_p) = \frac{\pi}{4}\int_0^\infty D^2 v_t(\mathrm{D})E(\mathrm{D},\mathrm{d}_p)N(\mathrm{D})dD \tag{2.8}$$

where D, $v_t(D)$, and $N(D)$ are the diameter, terminal settling velocity, and PSD of the hydrometeors, respectively, and $E(D, d_{p)}$ is the collection efficiency between the hydrometeor and the particle.

Greenfield (1957) showed that precipitation scavenging of aerosols by rain below cloud base is an important removal mechanism for aerosols of diameter less than 0.1 μm and greater than 1 μm and relatively negligible for aerosol diameters in the size range 0.1–1 μm. Slinn (1984) developed a semi-empirical equation for the collection efficiency of rain by combining the effects of Brownian diffusion, interception, and inertial capture that replicated Greenfield's observations. This formulation is used in contemporary studies of precipitation scavenging (e.g., Garcia Nieto et al. 1994; Chate et al. 2003; Sportisse 2007; Berthet et al. 2010) and is implemented by the author for the present study:

$$E(\mathrm{D},\mathrm{d}_p) = \frac{4}{R_e S_c}\left[1 + 0.4R_e^{1/2}S_c^{1/3} + 0.16R_e^{1/2}S_c^{1/2}\right]$$
$$+4\varphi\left[\omega^{-1} + (1 + 2\mathrm{R}_e^{1/2})\varphi\right] + \left[\frac{St - S_*}{St - S_* + 2/3}\right]^{3/2}\left(\frac{\rho_d}{\rho_w}\right)^{1/2} \qquad (2.9)$$

where the first term represents the process of Brownian diffusion, the second term represents the process of interception, and the third term represents the process of inertial capture; R_e, S_c, S_*, S_t are the Reynolds, Schmidt, critical Schmidt, and Stokes numbers, respectively; ϕ is the ratio of the particle diameter to the hydrometeor diameter; ω is the ratio of the viscosity of water to air; and ρ_d and ρ_w are the densities of the particle and water/ice, respectively.

Following suggestions by Slinn (1984), Loosmore and Cederwell (2004) and Seinfeld and Pandis (2006) reduced the complexity of Slinn's scavenging model by substituting a single representative diameter (e.g., the mass-mean diameter) for the full hydrometeor PSD in the scavenging coefficient formulation. This methodology is adopted in the present study, in which the integral form of the scavenging coefficient in equation 2.8 is expressed in terms of the precipitation rate, *P*, as:

$$\lambda(\mathrm{d}_p) = \frac{3}{2}\frac{E(D, d_p)P}{D} \qquad (2.10)$$

The scavenging of aerosols by frozen precipitation has received much less attention by researchers compared with the scavenging of aerosols by rain (Wang 2002). However, since snow was observed intermittently in Fukushima prefecture during the first week of the accident and a melting layer was noted in the boundary layer in the vicinity of the site in exploratory simulations of the accident performed by the author, scavenging pathways involving frozen precipitation should be considered. Slinn (1984)

developed an approximation for the scavenging of aerosol by frozen precipitation (e.g., snow, sleet, graupel, rimed crystals, dendrites), which is similar in form to the approximation for rain scavenging presented in equation 2.9:

$$E(\mathrm{D}, \mathrm{d}_p) \sim \left(\frac{B_p}{\nu} \right)^{\alpha} + \left\{ 1 - \exp\left[-(1 + \mathrm{R}_e^{1/2}) \frac{d_p^2}{D^2} \right] \right\} + \left[\frac{St - S_*}{St - S_* + 2/3} \right]^{3/2} \quad (2.11)$$

where B_p is the Brownian diffusivity of the aerosol, ν is the kinematic viscosity of air, and α is a constant that varies between 0.67 and unity for graupel and snow, respectively. This approximation is used in the present study to include the effects of aerosol scavenging by snow and graupel. Feng (2009) presented a scheme for the scavenging of aerosols by snow and ice crystals; however, to the author's knowledge the present study is the first to incorporate precipitation scavenging of aerosol by graupel using Slinn's approximation.

New parameterizations for moist physics were implemented in OMEGA for this study. Specifically, the single-moment bulk-water cloud microphysics parameterization based on Lin et al. (1983), but originally implemented in OMEGA (Bacon et al. 2000) such that liquid and solid phases of water were not allowed to coexist (Figure 2.4), was replaced by the author with the double-moment, mixed-phase, bulk-water cloud microphysics parameterization developed by Milbrandt and Yau (2005).

The new cloud microphysics parameterization was obtained from J. Milbrandt (personal communication, September 30, 2011) and added to OMEGA for this research to facilitate the simulation of precipitation scavenging by rain, snow, and graupel. The double-moment scheme uses a three-parameter gamma distribution:

$$N(\mathrm{D}) = N_0 D^{\alpha} e^{-\lambda D} \quad (2.12)$$

to describe the PSD of the cloud, ice, rain, snow, graupel, and hail fields where $N(D)$ is the total number concentration per unit volume of a given species of diameter D, N_0, λ, and α are the intercept, slope, and dispersion or shape parameters, respectively (Straka 2009).

The Milbrandt & Yau scheme requires the user to specify the cloud condensation number density (CCN) as a basic parameter for warm microphysical processes and the homogeneous freezing of cloud to ice. Because a large amount of the computational domain is covered by ocean, the author also implemented a scheme that initializes the CCN to values representative of maritime (80 cm^{-3}) or continental (200 cm^{-3}) influences automatically depending on whether the surface computational cell represents a water or land surface, respectively. A flow diagram of the microphysical processes parameterized in the Milbrandt & Yau scheme is presented in Figure 2.5 and each process notation referenced with the source and sink terms in Table 2.1.

A version of the Tiedtke cumulus parameterization developed by Zhang et al. (2011) was extracted from a publically available version (V3.4.1) of the Advanced Research Weather Research and Forecasting model (ARW-WRF; Skamarock et al. 2008) and implemented in OMEGA by the author to improve the representation of sub-grid scale convection over areas of the ocean with relatively coarse grid spacing. The computational mesh used in an OMEGA simulation spans a continuous range of horizontal grid scales, hence the influence of the cumulus parameterization (e.g., thermodynamical and dynamical feedback) is weighted inversely by cell area in the range 3–100 km^2 while the cloud microphysics parameterization is active over the entire domain.

2.3 Data

The initial and lateral boundary conditions for the weather simulations were derived from seven different global operational forecast and analysis fields and global archived reanalysis products that are described in Table 2.2. In addition, each forecast and analysis initial condition was augmented with all available radiosonde (METAR) and surface observations (National Climatic Data Center Integrated Surface Hourly) contained within the simulation domain at each respective initialization time.

The suite of seven initialization datasets described in Table 2.2 was used to create initial and lateral boundary conditions for the OMEGA simulations. Prior to beginning the simulation schema described in section 1.2, a 30-hour test simulation centered on the accident site commencing 00 UTC 15 March 2011, was performed using each of the seven initial conditions, holding all other model parameters constant. The results were compared qualitatively to determine which initialization dataset produced the most accurate OMEGA simulation of the ensuing weather. The period 00 UTC 15 March–06 UTC 16 March was chosen for testing because observed atmospheric conditions that followed the model start date and time included an intensifying synoptic scale coastal low pressure system with precipitation.

Of the seven initialization datasets, the OMEGA simulation that used the ECMWF $0.141° \times 0.141°$ horizontal resolution operational analysis and 6-hourly analysis boundary conditions was judged qualitatively to have produced the most accurate weather simulation in terms of surface winds and precipitation in the vicinity of the accident site, hence the ECMWF initial conditions were selected to perform the series of

short-duration (e.g., 30 hour) OMEGA weather simulations that were used for the dispersion calculations.

Radiation data collected by the U.S. Department of Energy were obtained from the National Nuclear Security Administration (NNSA) Japan Response data repository portal to verify the cumulative deposition fields calculated by the model simulations. The NNSA dataset comprised observations of surface contamination due to ^{137}Cs that were collected from fixed-wing aircraft during the period 2 April–9 May 2011. The observations were altitude-corrected, converted to exposure rates at 1 meter AGL, and projected to a common date of 30 June 2011. The intensity of surface-deposited radiation falls off approximately exponentially with height, thus it is important to ensure that the observations are corrected for the altitude of the detector. Altitude correction is performed by flying over defined areas at multiple altitudes and employing empirical corrections to reduce the measurements to ground concentrations (Minty 1997).

Lastly, a time series of surface precipitation observations for Japan during the accident study period were obtained by the author during a visit to the National Institute of Informatics (NII), Tokyo (A. Kitamoto, personal communication, November 24, 2011). The precipitation observations were created by correcting a composite radar precipitation analysis constructed at 1 km spatial resolution and 10 minute time resolution from approximately 40 C-band and Doppler radars with surface precipitation observations obtained from approximately 9300 rain gauges. This radar-rain gauge analyzed precipitation data is used operationally for very short range forecasts of precipitation in Japan and provides an ideal observational dataset to verify the OMEGA surface precipitation predictions.

2.4 Setup

The atmospheric release phase of the Fukushima accident spanned several months, with the largest fraction of radioisotopes released during the first week; therefore, a methodology to simulate the dispersion continuously over the period 11–17 March 2011 was required that struck a balance between accuracy and efficiency. Implementing the dispersion model as a post processor, as opposed to embedding the dispersion calculations within the meteorological simulation, achieved the goal of creating a simulation system that balanced physical fidelity, or the degree to which the phenomena of interest are modeled, numerical accuracy of the algorithms, and operational constraints of the computer system that, for this research, were governed by fixed limits on the maximum amount of time allowed to complete a simulation (i.e., 12 hours) and the total number of CPU hours allocated for the research project.

The weather and dispersion simulations were performed on the National Center for Atmospheric Research–Wyoming Supercomputer Center (NWSC) Yellowstone system. Simulations were completed by implementing a processing stream composed of three parts. The first part of the processing stream comprised the OMEGA weather simulation. The second part of the processing stream comprised the dispersion model simulation, which was based on the output of the OMEGA weather simulations. Finally, the third part of the processing stream comprised post processing and visualization of the weather and dispersion results.

A single unstructured mesh was generated that was used for each of the OMEGA weather simulations. The mesh filled a horizontal domain that spanned 120°E–170°E and 20°N–60°N (Figure 2.6). The unstructured mesh was adapted to coastlines and terrain

gradients (Figure 2.7) resulting in minimum edge lengths that spanned 3 to 80 km over land and ocean areas, respectively. The mesh was composed of 112,000 computational cells in each of 51 vertical layers, with 24 levels below 1 km to resolve processes in the atmospheric boundary layer. The separation distance between vertical layers was stretched in the lowest 48 levels such that vertical layer spacing ranged from 10 meters in the surface layer to 100 meters at 1 km AGL, increasing to approximately 1.5 km at the top of the domain, which was set at 23 km AGL. The OMEGA weather simulations used the USGS topographic database at 30 arc seconds (~1 km) horizontal resolution to build the underlying terrain for land areas (Figure 2.8) and the daily FNMOC High Resolution SST/Sea Ice Analysis database at ~10 km horizontal resolution to derive sea surface temperatures over ocean areas.

The set of OMEGA weather simulations that served as meteorological input for the dispersion calculations comprised six separate 30-hour model runs. An examination of the model results corresponding to the first week of the accident revealed a natural grouping between a dry weather period that spanned 12, 13, and 14 March and a wet weather period that spanned 15 and 16 March. The grouping provided a convenient validation period to compare the upper air observations located nearest the accident site (Figure 2.9) with the OMEGA predictions and also allowed comparisons of synoptic scale weather features from the ECMWF analyses with the OMEGA predictions. Specifically, winds and temperatures at 500 hPa and 850 hPa, a cross section analysis of winds and temperatures along 140°E, and SkewT-logP diagrams at the location of the Tateno, Japan upper air station (Figure 2.9) from the ECMWF 0.141° x 0.141° analysis are compared with OMEGA 30-hour forecasts valid at 00 UTC 12, 13, 15, and 16 March

in Figure 2.10–Figure 2.21. The surface weather of 12 and 13 March were fully in the dry period of the accident and influenced by high pressure. In contrast, the surface weather of 15 and 16 March were fully in the wet period of the accident and influenced by a developing area of low pressure along the east coast of Japan. The surface weather of 14 March was transitional between the two periods and thus not included in the validation comparisons that follow.

Compared with the analysis in Figure 2.10a, the OMEGA 500 hPa forecast valid 00 12 March (Figure 2.10b) shows that the model accurately predicted the position of the trough to the east of northern Japan and Hokkaido, but otherwise under predicted its amplitude and lifted the trough too quickly. As a result, the forecast position of the low center over the eastern Kamchatka Peninsula is too far downstream compared with the analysis. At 850 hPa, the OMEGA prediction of the high and low centers and temperature fields (Figure 2.10d) are in good agreement with the analysis (Figure 2.10c), however the forecast under predicted the magnitude and coverage of the jet core that extends southeastward from the Pacific coast of central and northern Japan to the low center at 160°E. A cross section that extends along 140°E from 50°N to 25°N (Figure 2.11) shows that the OMEGA predictions of the jet maximum (Figure 2.11b) and vertical temperature structure (Figure 2.11d) are in good agreement with the analyses shown in Figure 2.11a and Figure 2.11c, respectively.

A comparison of the Tateno, Japan sounding from the ECMWF analysis and the OMEGA forecast is shown in Figure 2.12. The temperature profile predicted by the OMEGA simulation (Figure 2.12b) has a cold bias near the surface and is capped by a weak inversion at 1000 hPa compared with the analysis shown in Figure 2.12a. In the

layer extending above the inversion to 750 hPa, the OMEGA prediction exhibits a warm and moist bias in the boundary layer compared with the analysis. Wind speeds are under predicted by OMEGA in the boundary layer and there is a considerable difference in the wind direction near the surface. Above the boundary layer, the OMEGA prediction of wind speed and direction is in good agreement with the analysis for this location.

Apart from missing the position of the low center east of the southern tip of the Kamchatka Peninsula and over predicting the jet core max traversing northeastern China (i.e., Manchuria), the OMEGA 500 hPa forecast fields valid 00 13 March (Figure 2.13b) are in good agreement with the analysis (Figure 2.13a). At 850 hPa, the OMEGA prediction (Figure 2.13d) exhibits a more zonal flow over northern Japan, under develops the low center northeast of Hokkaido, and misses the development of the low center south of Japan at 130°E compared with the analysis shown in Figure 2.13c. In addition, the OMEGA forecast lags the eastward progression of the anticyclonic circulation along 30°N. However, a cross section that extends along 140°E from 50°N to 25°N (Figure 2.14) shows that the OMEGA predictions of the jet maximum (Figure 2.14b) and vertical temperature structure (Figure 2.14d) are in good agreement with the analyses shown in Figure 2.14a and Figure 2.14c, respectively.

A comparison of the Tateno, Japan sounding from the ECMWF analysis and the OMEGA forecast is shown in Figure 2.15. The temperature profile predicted by the OMEGA simulation (Figure 2.15b) shows an inversion to approximately 950 hPa that is not supported by the analysis shown in Figure 2.15a. However, above the inversion the temperature and winds are in good agreement with the analysis. There is also a

significant dry bias in the near-surface moisture profile and a significant moist bias to near 750 hPa in the OMEGA prediction at this location.

The OMEGA 500 hPa forecast valid 00 15 March (Figure 2.16b) shows that the model predicted the position of the low centers over the east coast of Russia west of Sakhalin Island and over the Kamchatka Peninsula in agreement with the analysis (Figure 2.16a). However, the model prediction missed the closed low circulations over northeastern China and off the southeast coast of Kamchatka. Elsewhere the model prediction of the wind and temperature fields are generally in good agreement with the analysis. At 850 hPa, the OMEGA prediction (Figure 2.16d) is also in good agreement with the analysis shown in Figure 2.16c with the exception of the low center at 35°N, 145°E that is under developed. A cross section that extends along 140°E from 50°N to 25°N (Figure 2.17) shows that the OMEGA predictions of the jet maximum (Figure 2.17b) and vertical temperature structure (Figure 2.17d) are in good agreement with the analyses shown in Figure 2.17a and Figure 2.17c, respectively, although the OMEGA forecast under predicted the wind maximum at 12 km MSL by 20 knots south of Japan.

A comparison of the Tateno, Japan sounding from the ECMWF analysis and the OMEGA forecast is shown in Figure 2.18. The temperature and wind profiles are in good agreement with the analysis for this location. The predicted boundary layer wind profile is in very good agreement with the analysis in depicting onshore flow. The omega simulation produced a drier layer in the lower portion of the boundary layer extending from the surface to approximately 950 hPa.

The OMEGA 500 hPa wind and temperature field forecast valid 00 16 March shown in Figure 2.19b is in good agreement with the analysis, although the strength of

the closed circulation located over the east coast of Russia is under predicted. At 850 hPa, the OMEGA prediction (Figure 2.19d) is also in good agreement with the analysis with the exception of the low center east of Japan. Although the OMEGA forecast and ECMWF analysis position the low center at 40°N, the OMEGA forecast develops a relatively weaker circulation that is located closer to the east coast of Japan compared with the analysis shown in Figure 2.19c. A cross section that extends along 140°E from 50°N to 25°N (Figure 2.20) shows that the OMEGA predictions of the jet maximum (Figure 2.20b) and vertical temperature structure (Figure 2.20d) are in good agreement with the analyses shown in Figure 2.20a and Figure 2.20c, respectively.

A comparison of the Tateno, Japan sounding from the ECMWF analysis and the OMEGA forecast is shown in Figure 2.21. The predicted temperature, moisture, and wind profiles (Figure 2.21b) are in good agreement with the analysis for this location, although the OMEGA simulation produced a colder surface temperature and drier boundary layer compared with the analysis shown in Figure 2.21a.

The dispersion model setup involved specifying the puff radioactive material properties as a function of time for the duration of the release and setting the time interval at which dry deposition and precipitation scavenging processes would be calculated. The amount of radioactive material released during an interval of time (i.e., the release rate) was defined explicitly in Stohl et al. (2012) and Terada et al. (2012). In the Stohl source term, the time interval was 3-hourly for the duration of the release, whereas in the Terada source term, the time interval varied from 30 minutes when bounding an explosive event to nearly 40 hours during relatively quiescent periods. The Terada source term release heights were fixed at 20 m and 120 m AGL for non-explosive periods and increased to

100 or 300 m AGL during two relatively short (e.g., 30 minutes) periods corresponding to explosions that were observed at the containment structures. In contrast, the release heights used in the Stohl source term assumed average heights of 50, 300, and 1000 m AGL for the duration of the release, with the relative amounts of radioactive material injected at each height determined largely by the timing of explosive events at the containment structures and fires in spent fuel pools.

For each source term, the radioactive material was partitioned into size bins following a log normal PSD as described in Section 2.2. Taking into consideration the ambient aerosol size modes discussed in Section 1.2, particle size bin boundaries were set at: 0.01–0.02, 0.02–0.04, 0.04–0.08, 0.08–0.16, 0.16–0.32, 0.32–0.64, 0.64–1.28, 1.28–2.56, 2.56–5.12, 5.12–10.24, and 10.24–20.48 μm. The MMD and σ_g of the PSD, which determined the fractional amount of radioactive material in each size bin, were set at 0.5 and 1.5 μm, respectively. The cumulative distributions for the log normal distributed PSDs used in the present study are shown in Figure 2.22.

The density of particulate material released to the atmosphere during a reactor accident is important because it is used in the calculation of settling velocities and precipitation scavenging. Lewellen (1983) noted that the density of particles from a reactor accident will range from atmospheric aerosol density to the density of heavy elements. As the present study is focused on the release of aerosol-bound ^{137}Cs, the particle density used in defining the puff material properties is that of elemental Cesium, 1900 kg/m^3, following Stohl et al. (2012).

Finally, during a dispersion simulation, puff injection to the atmosphere and precipitation scavenging due to rain, snow, and graupel were calculated at 10-minute time

intervals to limit the number of particles in the domain for the purpose of reducing the CPU time. Dry deposition was calculated at every time step.

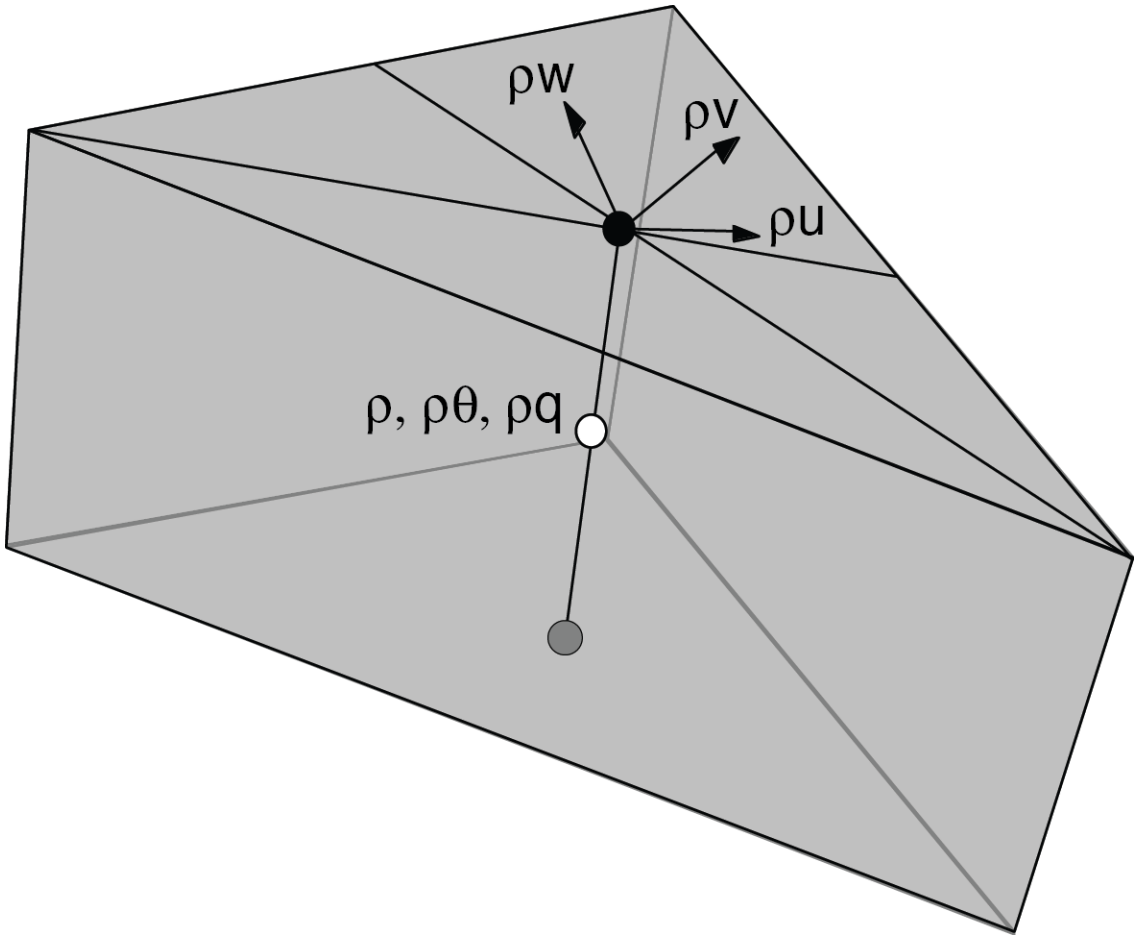

Figure 2.1 A depiction of a single OMEGA mesh element showing the dimensional structures that describe the properties of the unstructured volumetric mesh. Lowest-order structures are the vertices, which are specified by position (x, y, z). Edges convey connectivity of the mesh and are defined by the indices of starting and terminating vertices. Faces represent the area between adjacent volumetric cells and are described by the bounding edges. The cell or control volume is specified by the elemental list of faces. Scalar quantities (density, energy density, mixing ratio) are defined at the cell centroid. Vector quantities (u, v, and w-momentum) are defined at the center of vertically-stacked faces (from Bacon et al. 2000).

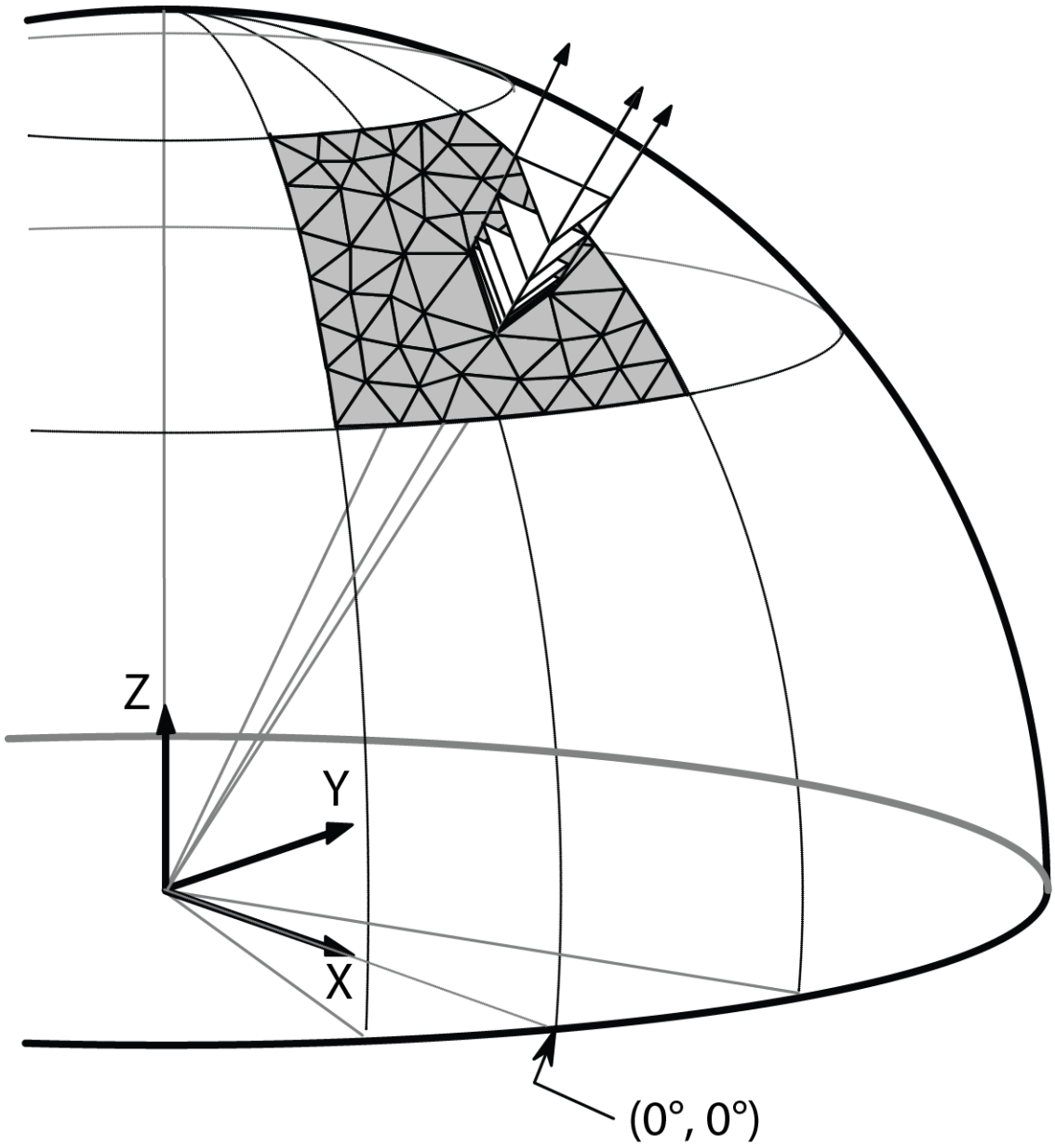

Figure 2.2 A depiction of the OMEGA coordinate system showing the Cartesian framework with origin placed at the center of the Earth, z-axis passing through the North Pole, x-axis passing through the intersection of the equator and the Prime Meridian, and y-axis orthogonal to both (from Bacon et al. 2000).

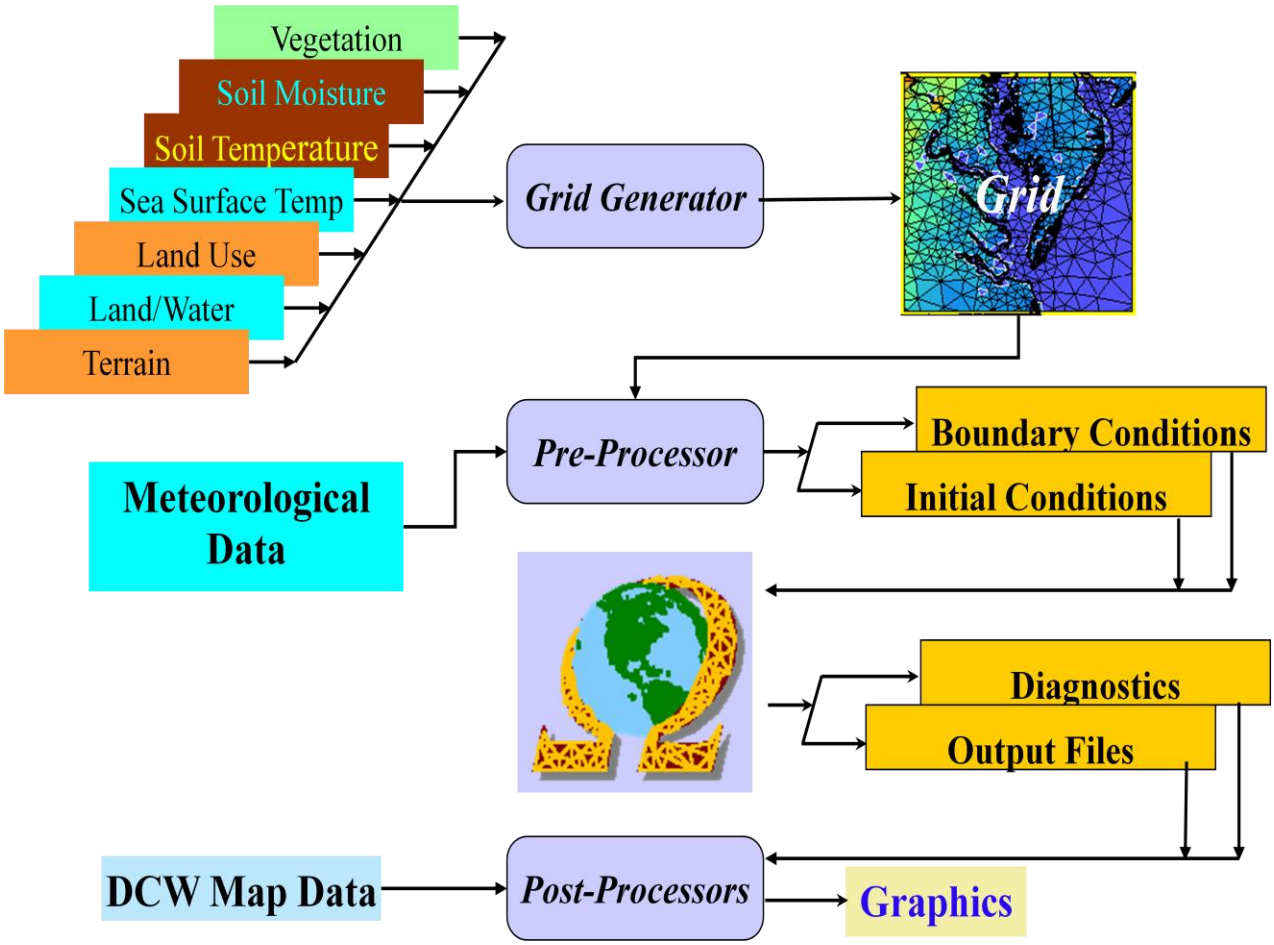

Figure 2.3 Schematic of the OMEGA numerical weather prediction system depicting its major components. The system comprises input datasets for surface properties and meteorological observations, a grid generator that produces the unstructured mesh, a preprocessor that ingests and interpolates the meteorological observations to the mesh to create initial and boundary conditions, and the OMEGA model. Model output is analyzed and visualized by a number of specialized postprocessors and serves as input for the atmospheric dispersion model (from Sarma 2001).

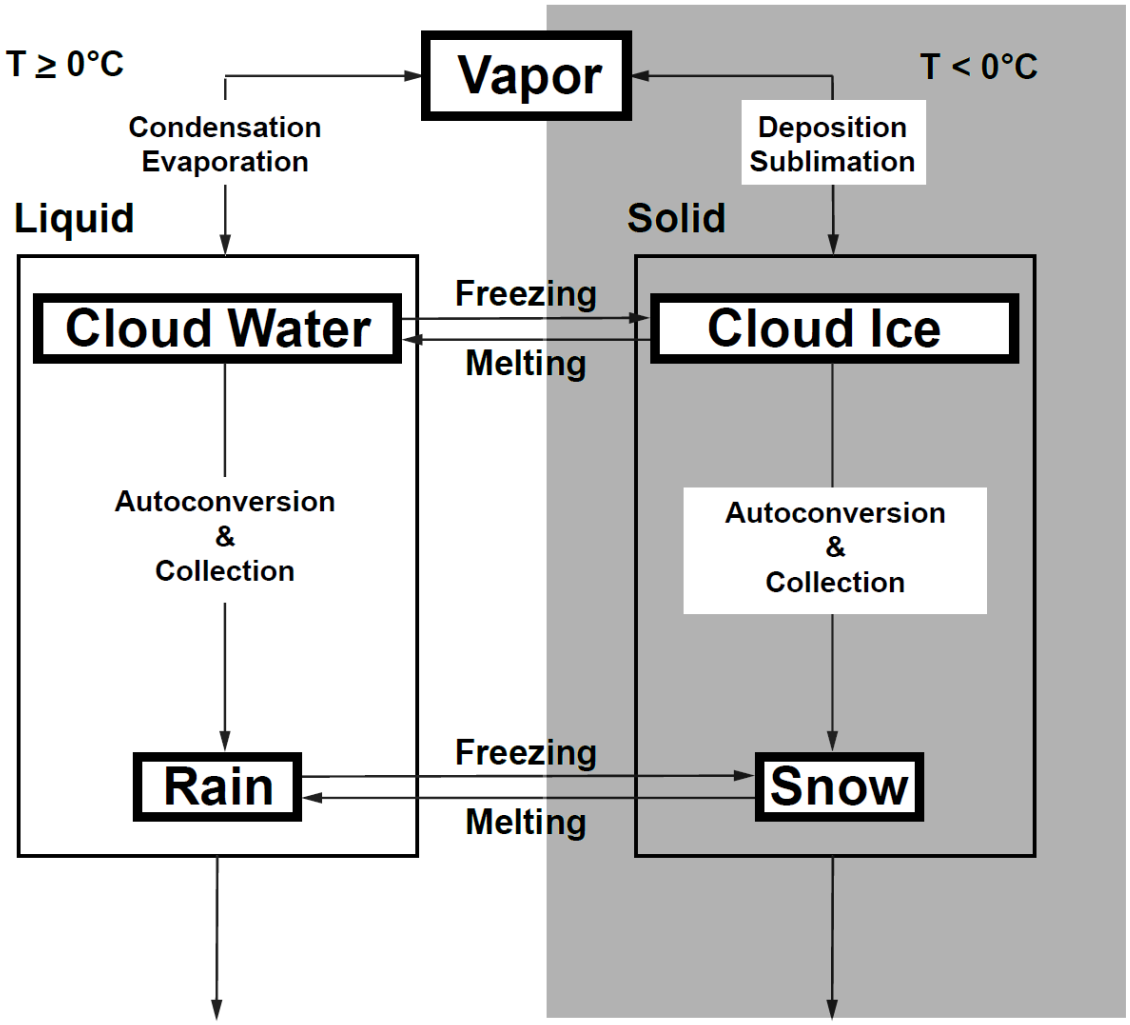

Figure 2.4 Diagram of the cloud and precipitation processes contained in the original OMEGA single-moment, bulk-water cloud microphysics parameterization (after Bacon et al. 2000).

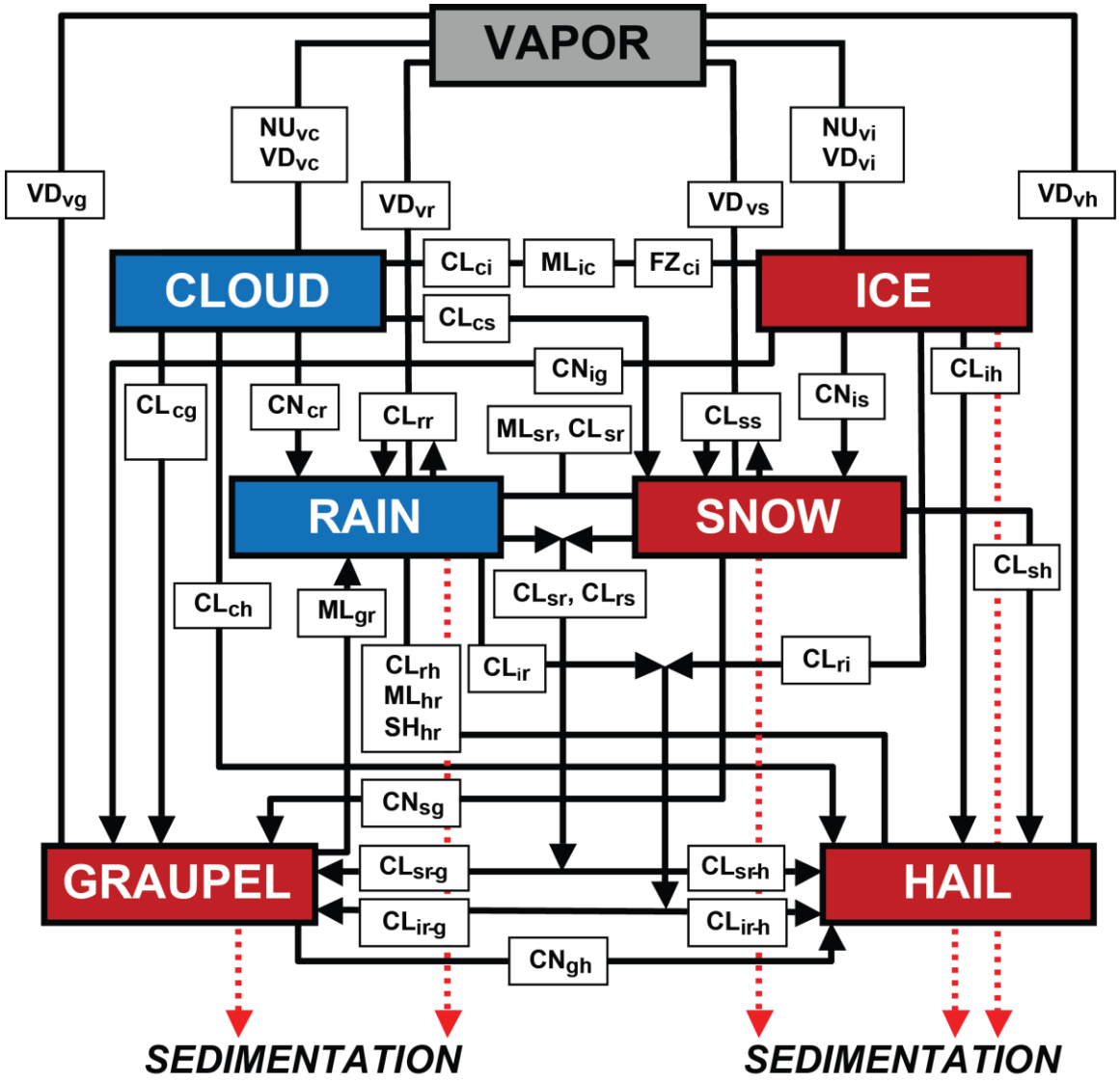

Figure 2.5 Diagram of cloud and precipitation processes modeled in OMEGA using the Milbrandt and Yau (2005) double-moment, mixed-phase, bulk-water cloud microphysics parameterization (after Milbrandt and McTaggart-Cowan 2008).

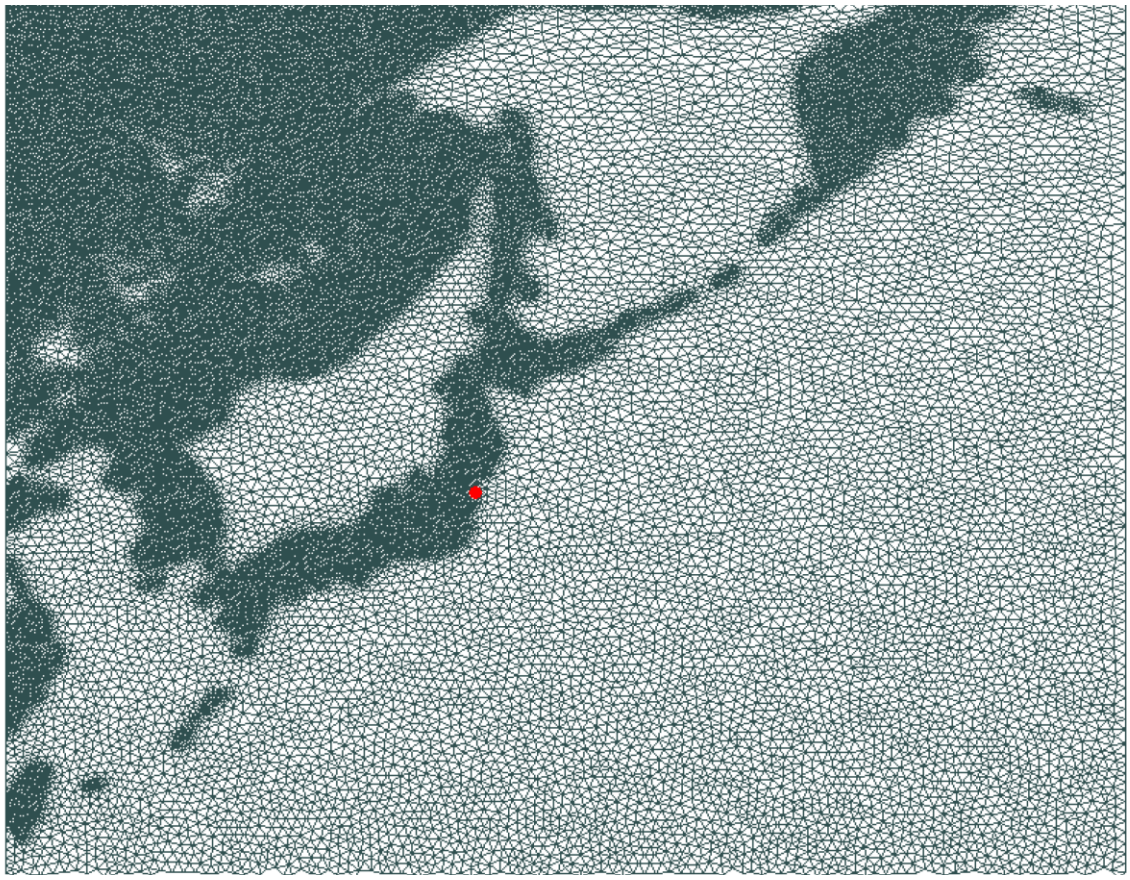

Figure 2.6 Unstructured mesh used in the OMEGA weather simulations. Horizontal domain covers 120°E–170°E and 20°N–60°N. Triangles show the horizontal configuration of the OMEGA computational cells. Red dot indicates the location of the Fukushima Daiichi nuclear power station.

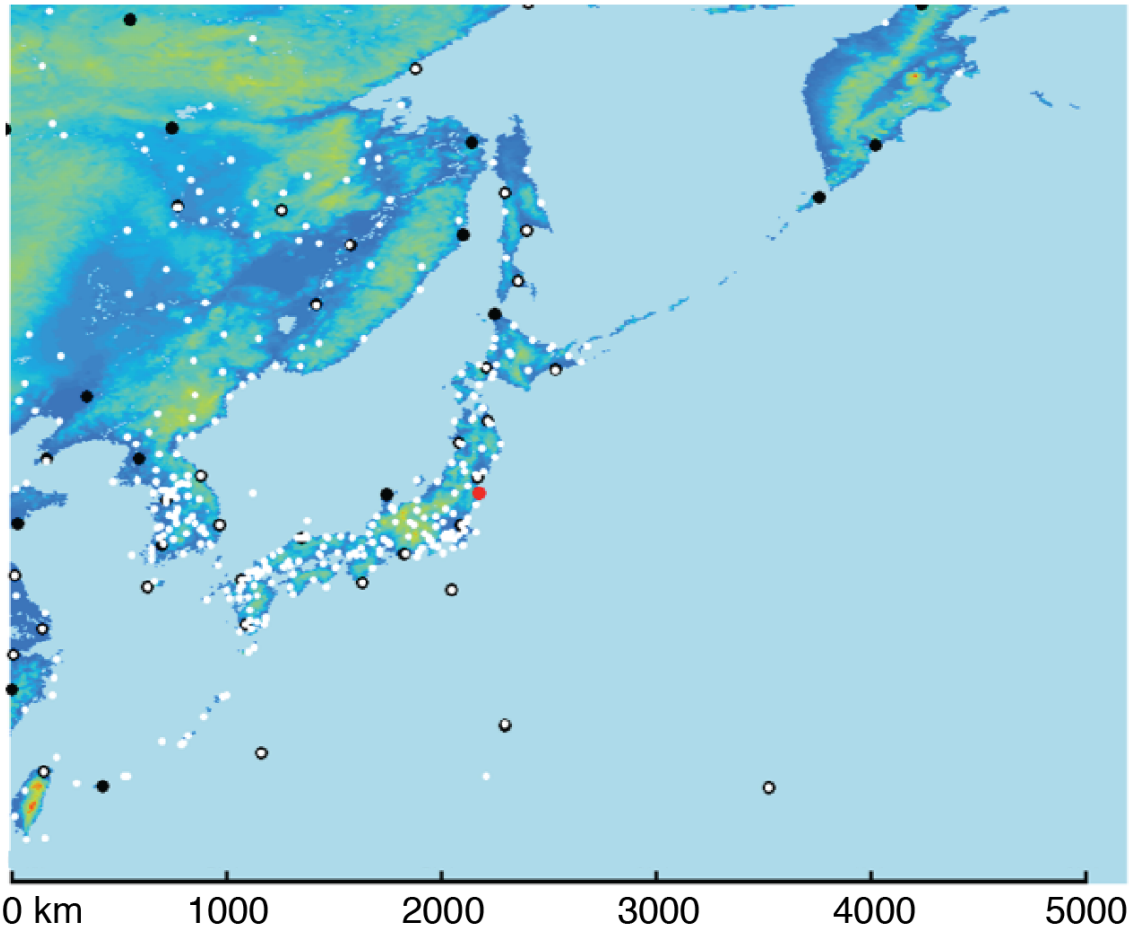

Figure 2.7 Terrain height (m) above MSL corresponding to the unstructured mesh shown in Figure 2.6. Locations of radiosonde observations are represented by large black circles. Locations of surface observations are represented by smaller white circles. Red circle indicates the location of the Fukushima Daiichi nuclear power station. Horizontal scale (km) is shown at bottom. Upper air and surface observation coverage is shown for 00 UTC 11 March 2011.

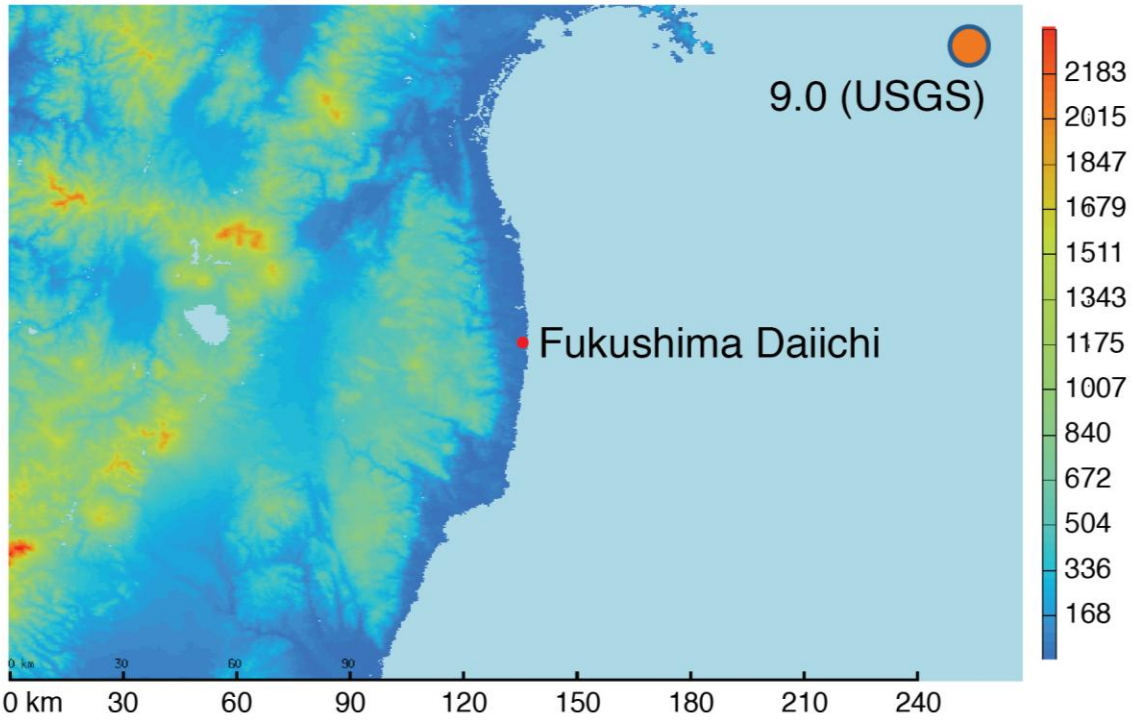

Figure 2.8 OMEGA terrain height at ~1 km horizontal resolution for a subset of the computational domain centered on the accident site. Orange circle depicts the epicenter of the 11 March 2011 earthquake. Red circle indicates the location of the Fukushima Daiichi nuclear power station. Horizontal scale (km) is shown at bottom. Vertical scale of terrain height (m MSL) is shown at right.

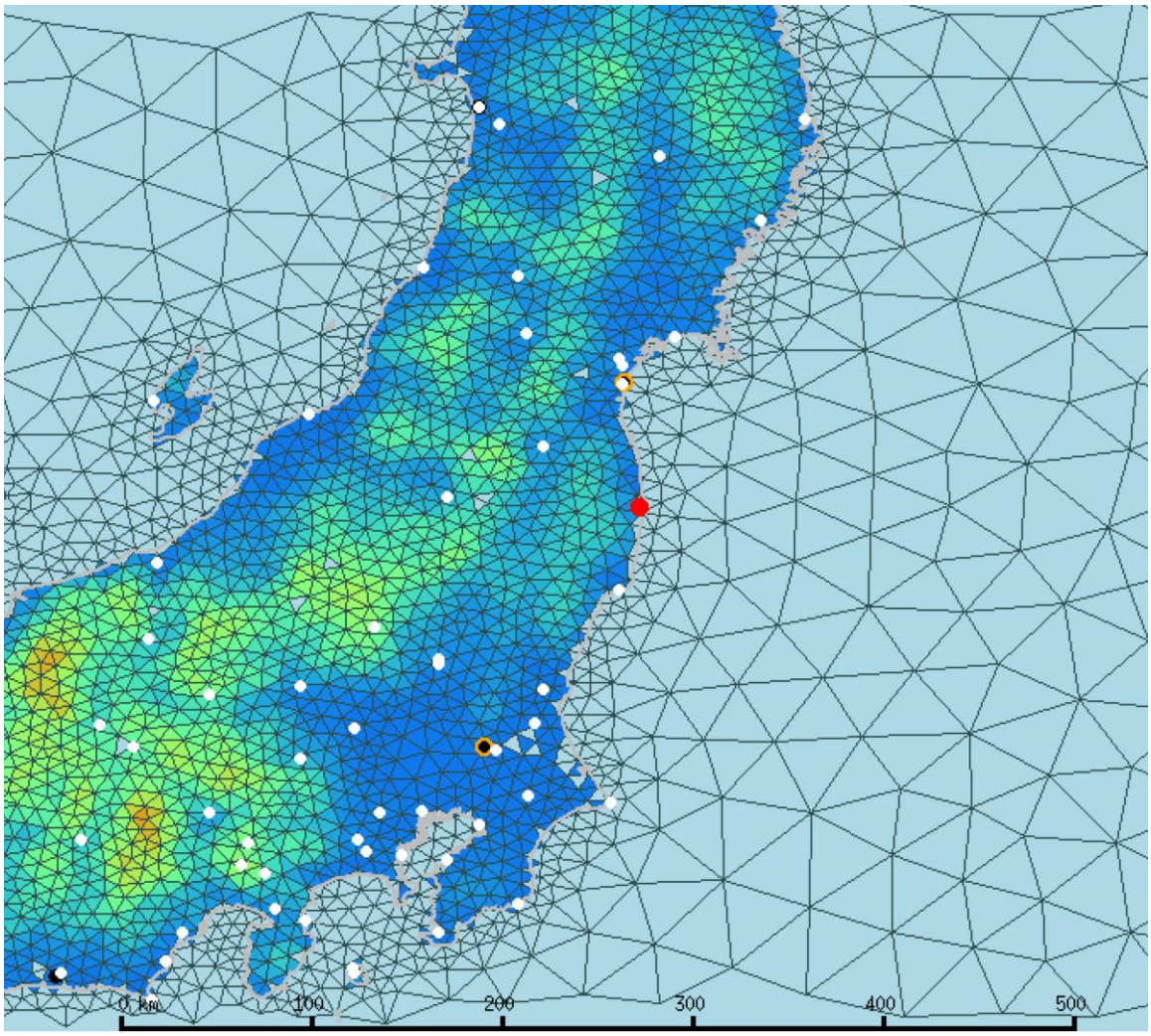

Figure 2.9 OMEGA terrain height and unstructured mesh for a subset of the computational domain centered on the accident site. Locations of radiosonde and surface observations are represented by large black circles and smaller white circles, respectively. Red circle indicates the location of the Fukushima Daiichi nuclear power station. Southern-most orange and black circle shows the location of the Tateno radiosonde observation. Horizontal scale (km) is shown at bottom. Upper air and surface observation coverage is shown for 00 UTC 11 March 2011.

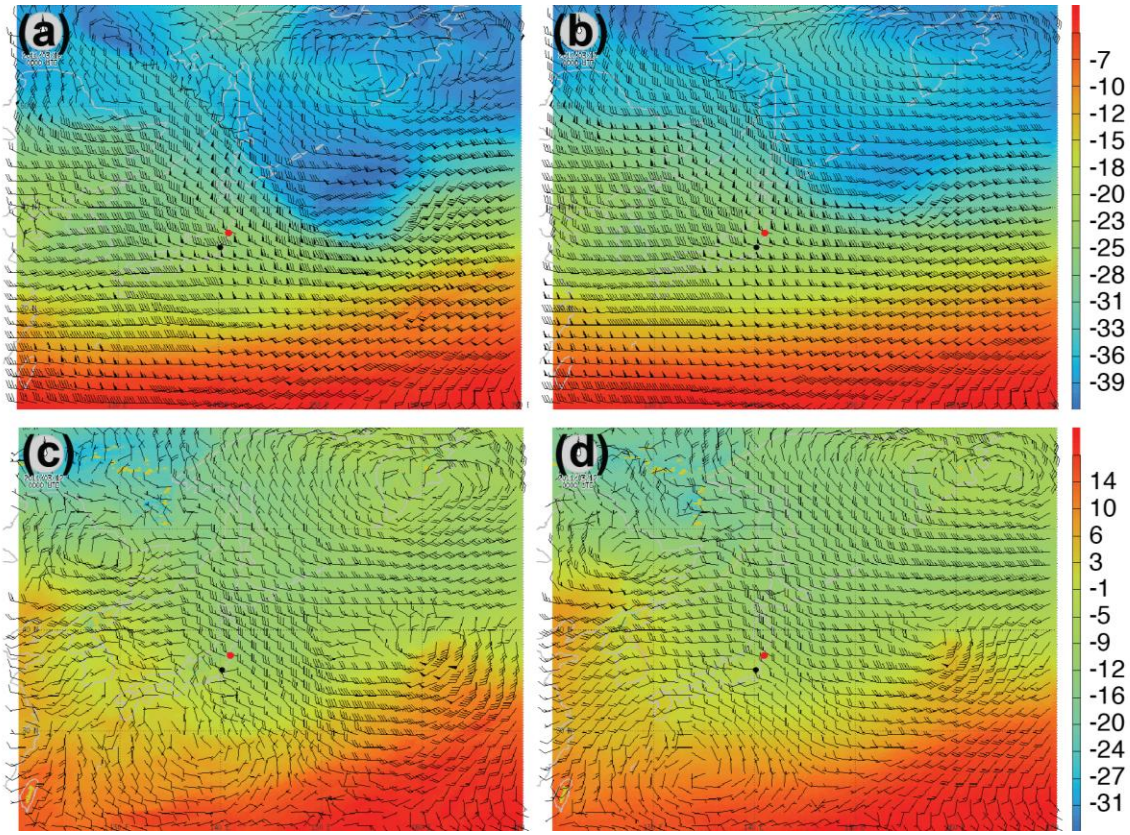

Figure 2.10 Comparison of ECMWF 0.141° x 0.141° analysis with OMEGA 30-hour forecast at 00 UTC 12 March 2011. (a) ECMWF 500 hPa wind (knots) and temperature (°C). (b) OMEGA 500 hPa wind (knots) and temperature (°C). (c) ECMWF 850 hPa wind (knots) and temperature (°C). (d) OMEGA 850 hPa wind (knots) and temperature (°C). Red circle shows the location of the Fukushima Daiichi nuclear power station. Black circle shows the location of the Tateno radiosonde release.

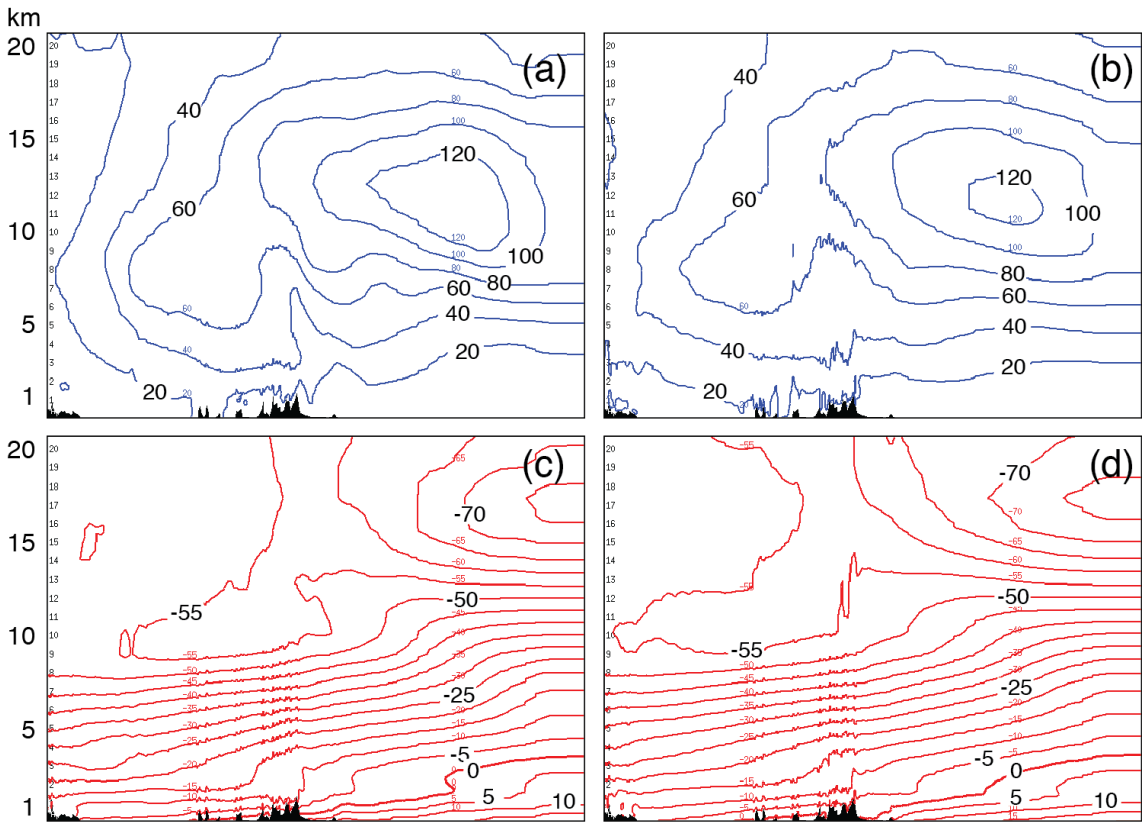

Figure 2.11 Comparison of ECMWF 0.141° x 0.141° analysis with OMEGA 30-hour forecast at 00 UTC 12 March 2011 along a north-south cross section at140°E from 50°N (LHS) to 25°N (RHS). (a) ECMWF wind (knots). (b) OMEGA wind (knots). (c) ECMWF temperature (°C). (d) OMEGA temperature (°C). Contour interval is 20 knots for wind, 5°C for temperature.

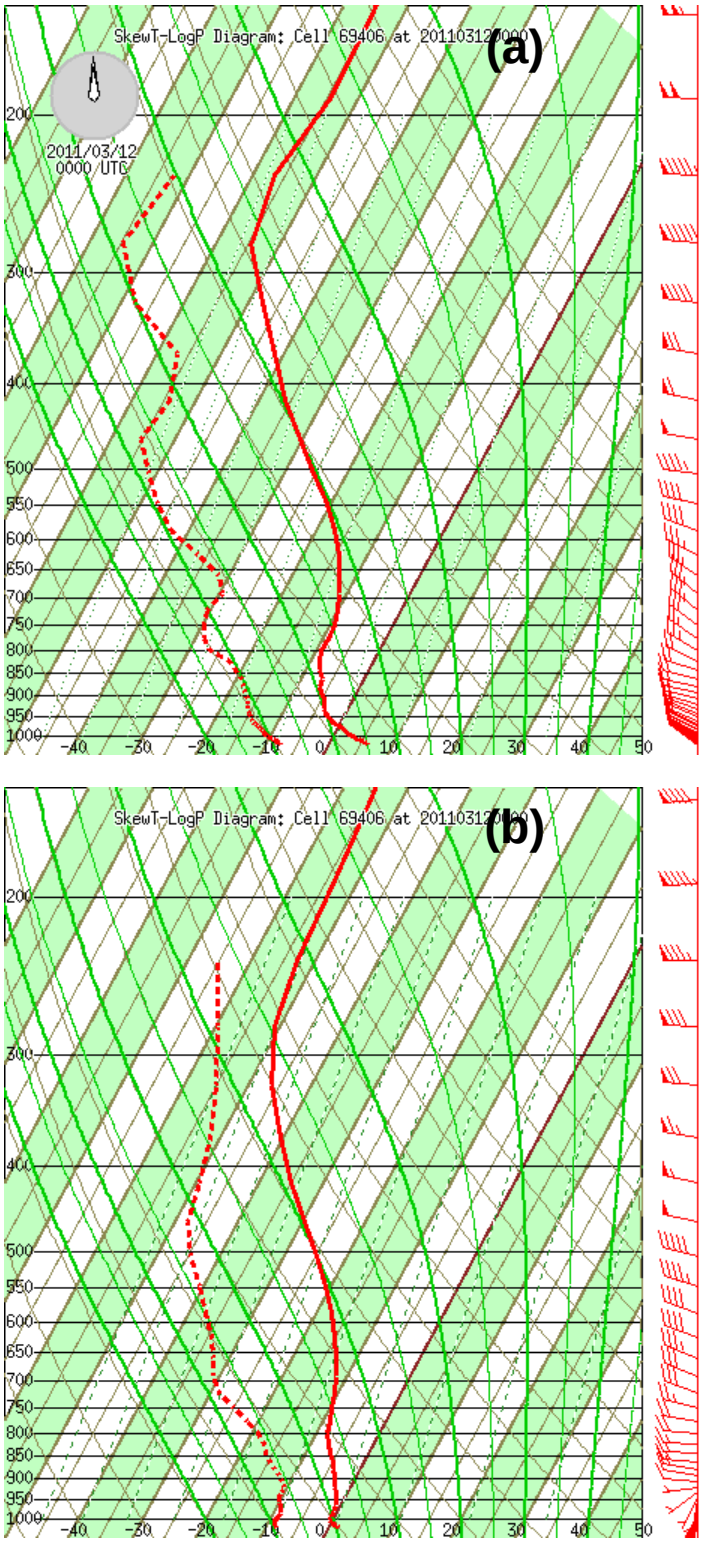

Figure 2.12 Comparison of Tateno sounding at 00 UTC 12 March 2011. (a) ECMWF 0.141° x 0.141° analysis. (b) OMEGA 30-hour forecast.

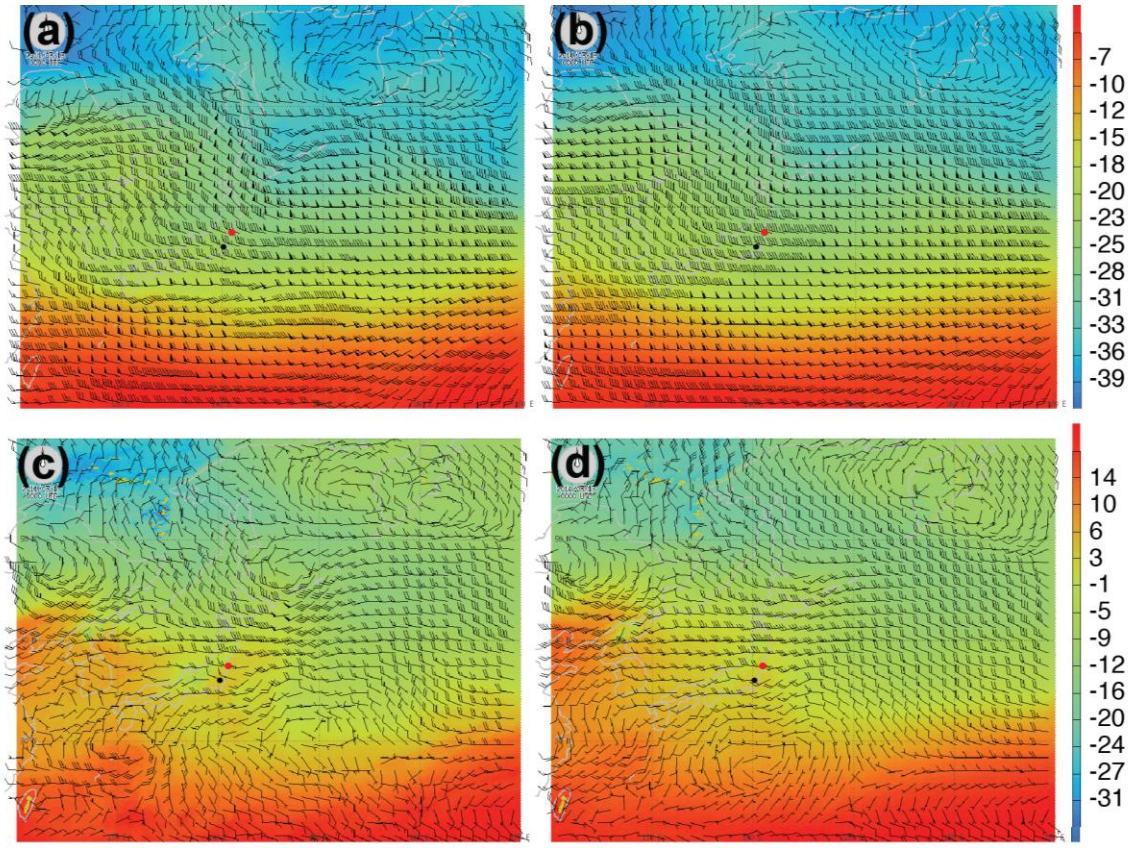

Figure 2.13 Comparison of ECMWF 0.141° x 0.141° analysis with OMEGA 30-hour forecast at 00 UTC 13 March 2011. (a) ECMWF 500 hPa wind (knots) and temperature (°C). (b) OMEGA 500 hPa wind (knots) and temperature (°C). (c) ECMWF 850 hPa wind (knots) and temperature (°C). (d) OMEGA 850 hPa wind (knots) and temperature (°C). Red circle shows the location of the Fukushima Daiichi nuclear power station. Black circle shows the location of the Tateno radiosonde release.

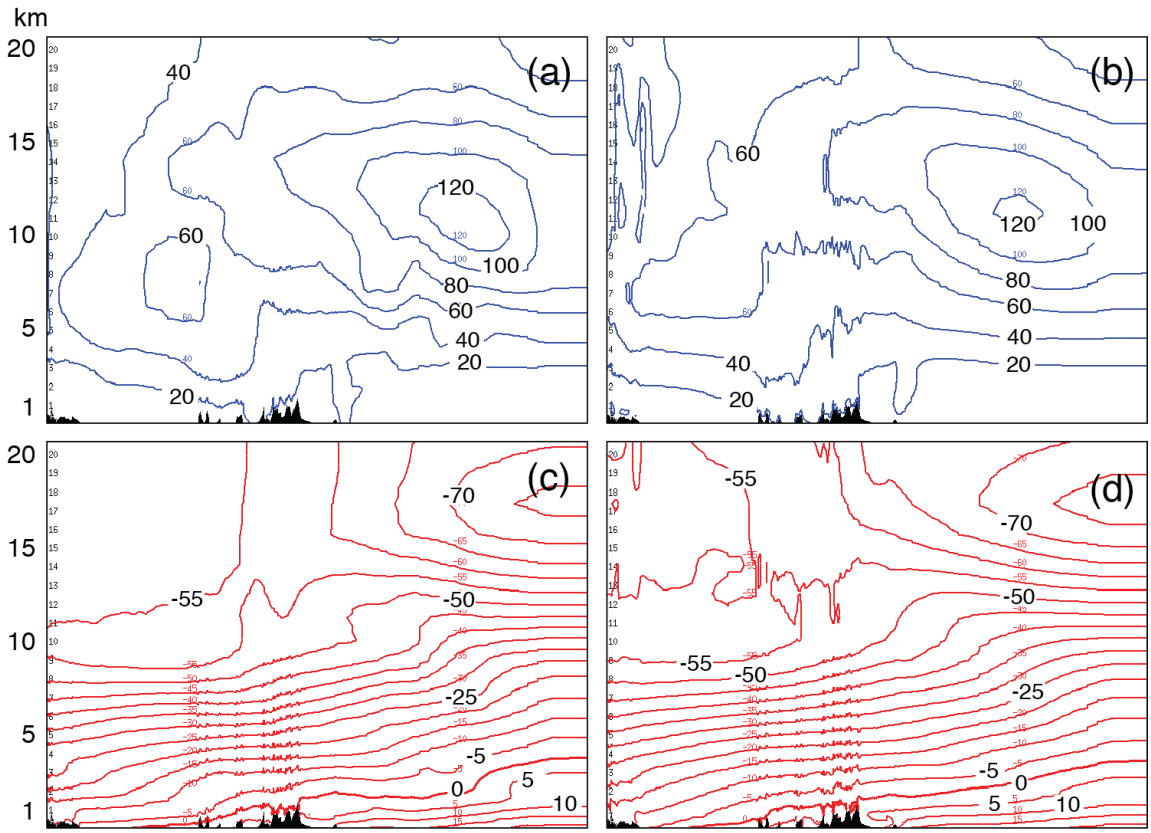

Figure 2.14 Comparison of ECMWF 0.141° x 0.141° analysis with OMEGA 30-hour forecast at 00 UTC 13 March 2011 along a north-south cross section at140°E from 50°N (LHS) to 25°N (RHS). (a) ECMWF wind (knots). (b) OMEGA wind (knots). (c) ECMWF temperature (°C). (d) OMEGA temperature (°C). Contour interval is 20 knots for wind, 5°C for temperature.

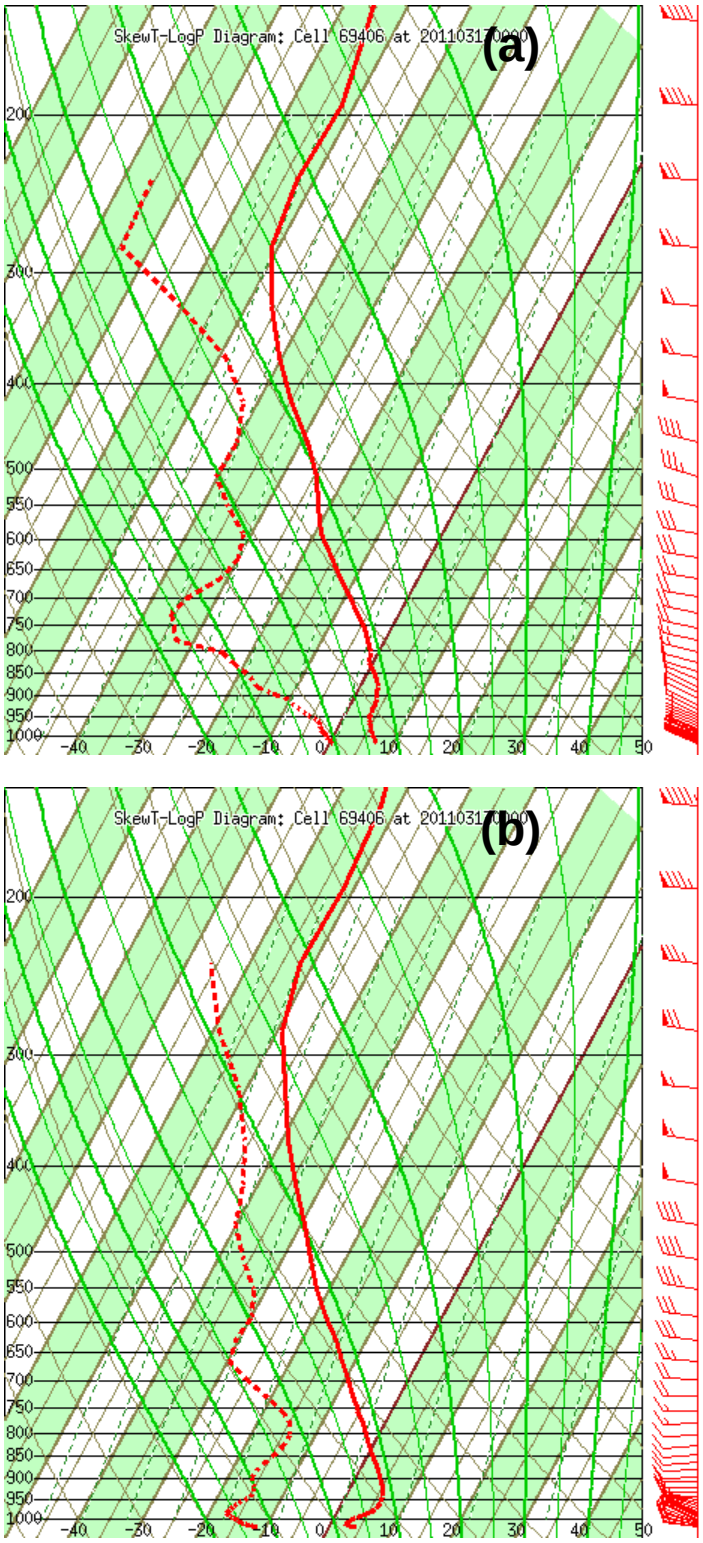

Figure 2.15 Comparison of Tateno sounding at 00 UTC 13 March 2011. (a) ECMWF 0.141° x 0.141° analysis. (b) OMEGA 30-hour forecast.

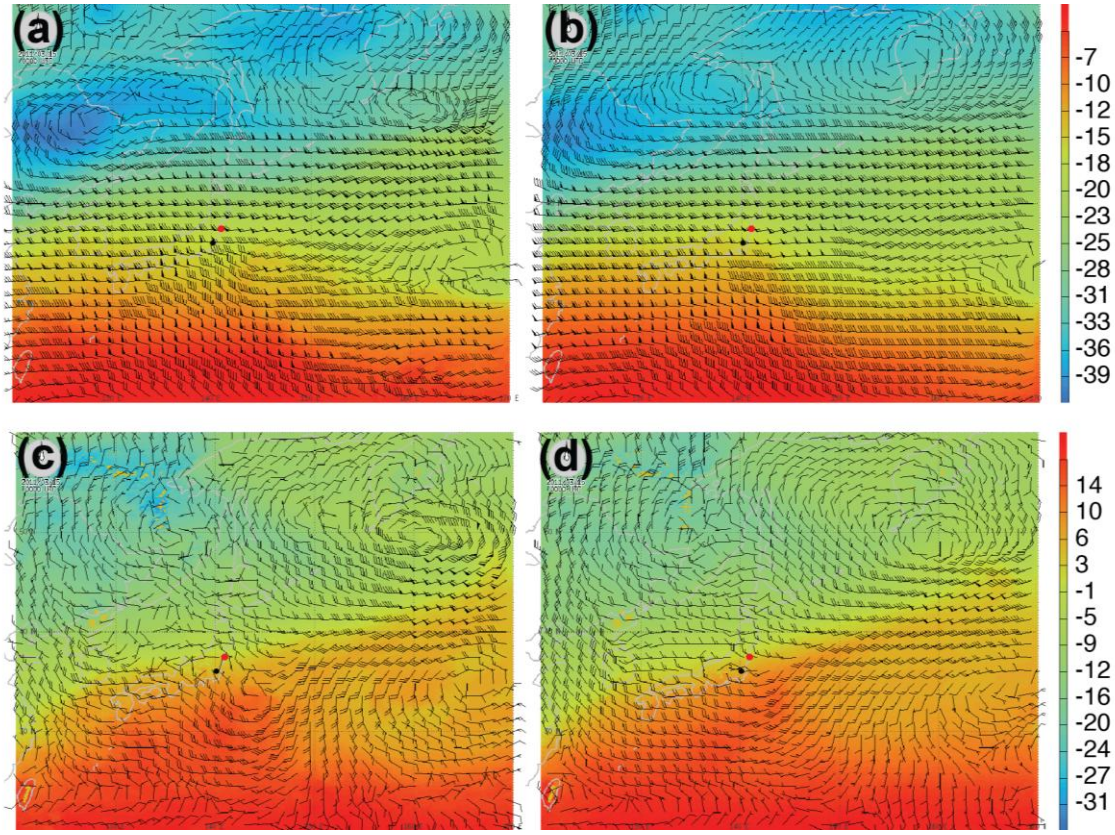

Figure 2.16 Comparison of ECMWF 0.141° x 0.141° analysis with OMEGA 30-hour forecast at 00 UTC 15 March 2011. (a) ECMWF 500 hPa wind (knots) and temperature (°C). (b) OMEGA 500 hPa wind (knots) and temperature (°C). (c) ECMWF 850 hPa wind (knots) and temperature (°C). (d) OMEGA 850 hPa wind (knots) and temperature (°C). Red circle shows the location of the Fukushima Daiichi nuclear power station. Black circle shows the location of the Tateno radiosonde release.

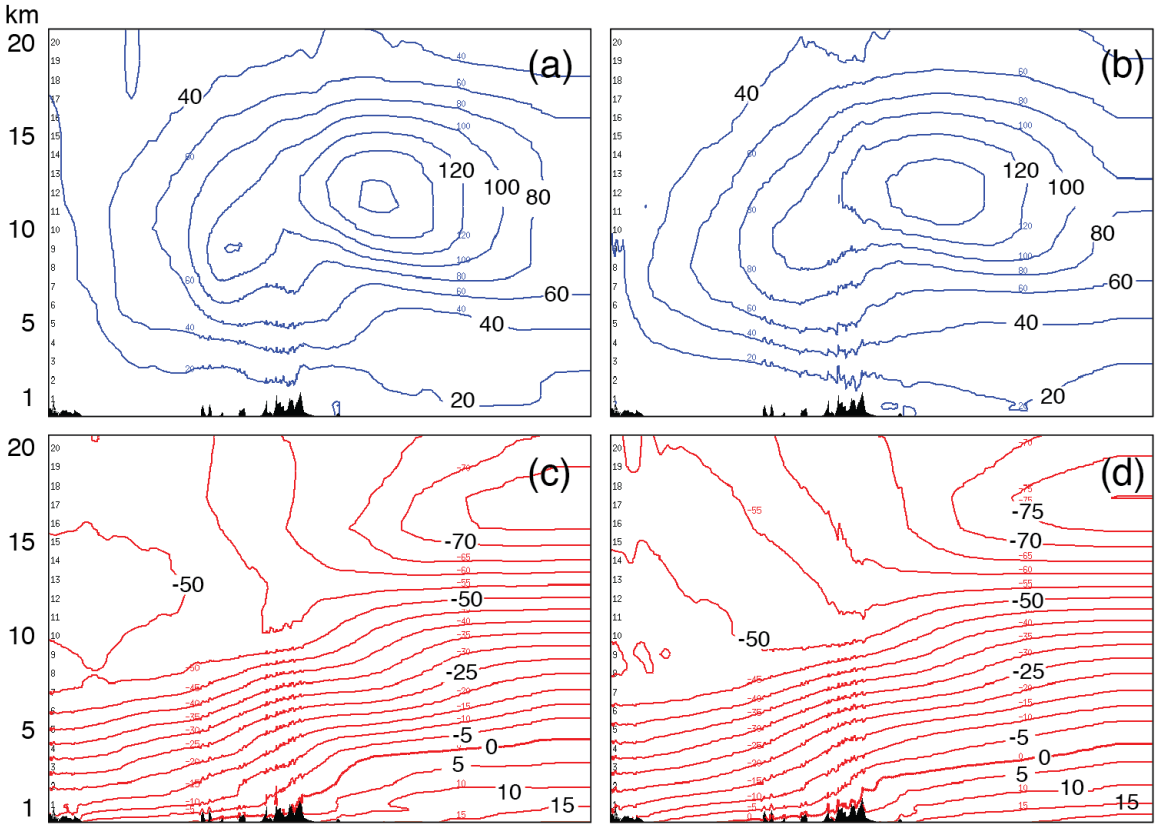

Figure 2.17 Comparison of ECMWF 0.141° x 0.141° analysis with OMEGA 30-hour forecast at 00 UTC 15 March 2011 along a north-south cross section at140°E from 50°N (LHS) to 25°N (RHS). (a) ECMWF wind (knots). (b) OMEGA wind (knots). (c) ECMWF temperature (°C). (d) OMEGA temperature (°C). Contour interval is 20 knots for wind, 5°C for temperature.

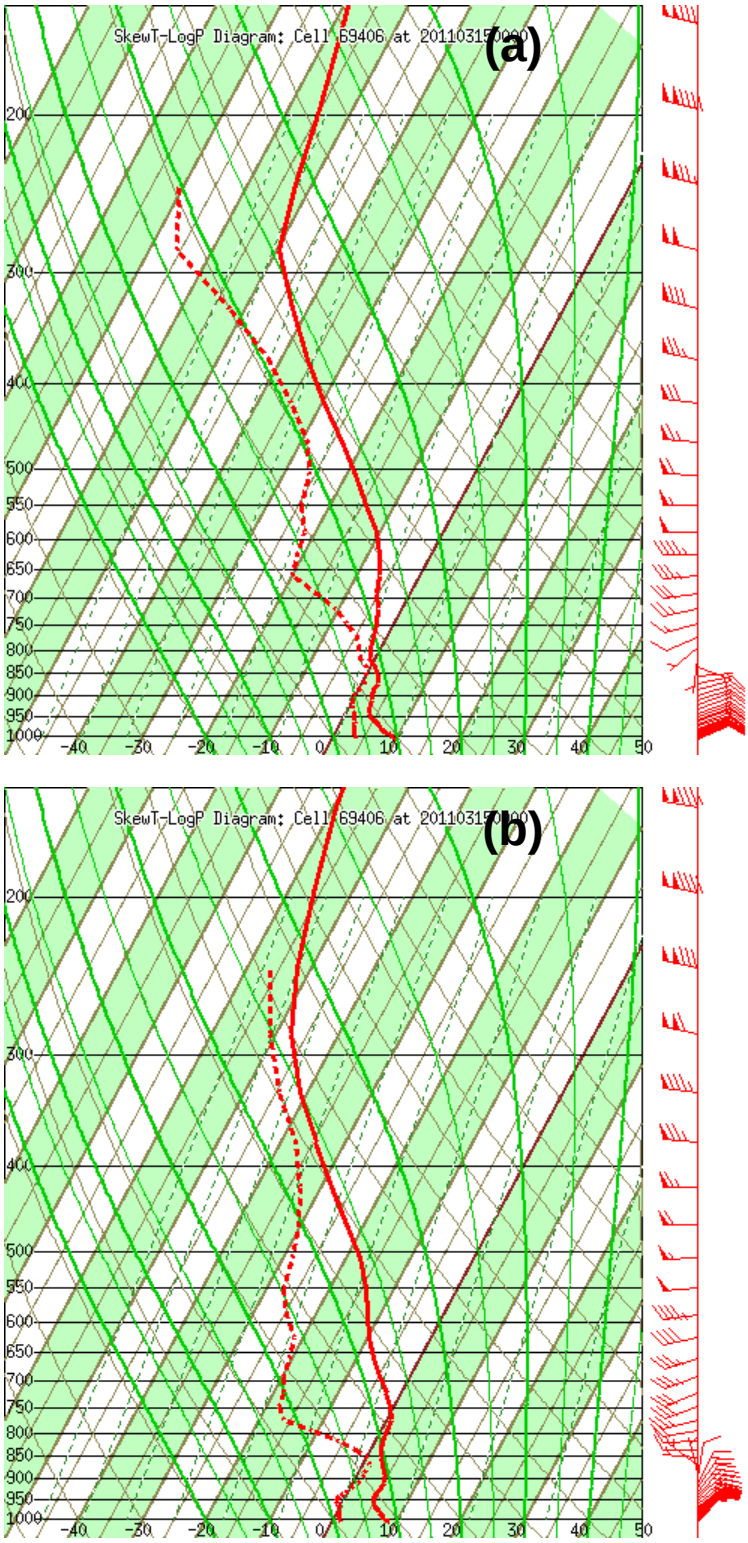

Figure 2.18 Comparison of Tateno sounding at 00 UTC 15 March 2011. (a) ECMWF 0.141° x 0.141° analysis. (b) OMEGA 30-hour forecast.

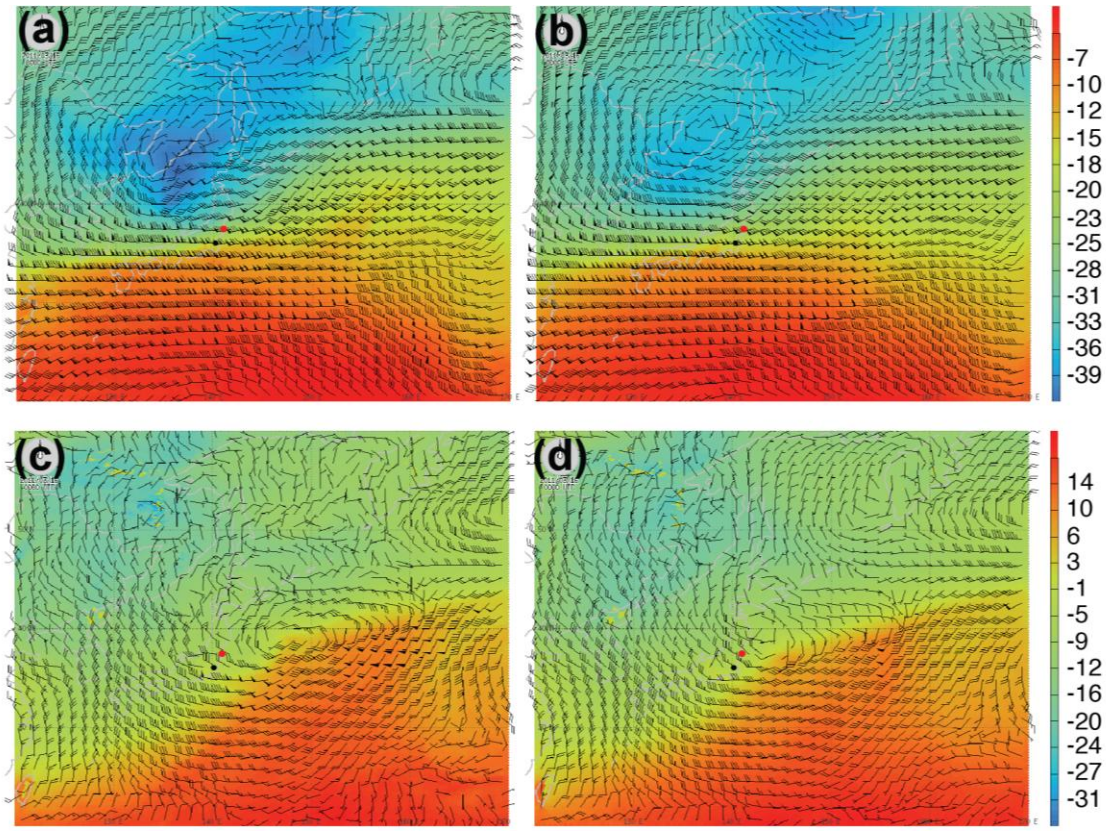

Figure 2.19 Comparison of ECMWF 0.141° x 0.141° analysis with OMEGA 30-hour forecast at 00 UTC 16 March 2011. (a) ECMWF 500 hPa wind (knots) and temperature (°C). (b) OMEGA 500 hPa wind (knots) and temperature (°C). (c) ECMWF 850 hPa wind (knots) and temperature (°C). (d) OMEGA 850 hPa wind (knots) and temperature (°C). Red circle shows the location of the Fukushima Daiichi nuclear power station. Black circle shows the location of the Tateno radiosonde release.

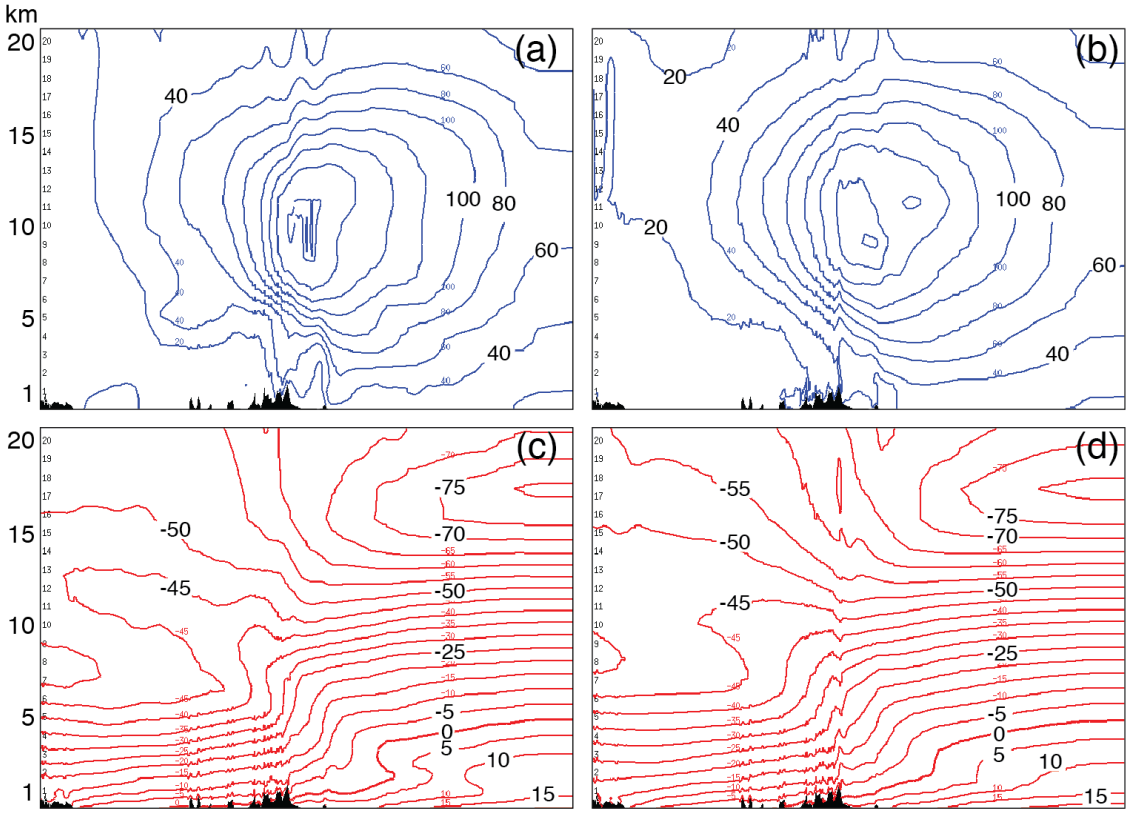

Figure 2.20 Comparison of ECMWF 0.141° x 0.141° analysis with OMEGA 30-hour forecast at 00 UTC 16 March 2011 along a north-south cross section at140°E from 50°N (LHS) to 25°N (RHS). (a) ECMWF wind (knots). (b) OMEGA wind (knots). (c) ECMWF temperature (°C). (d) OMEGA temperature (°C). Contour interval is 20 knots for wind, 5°C for temperature.

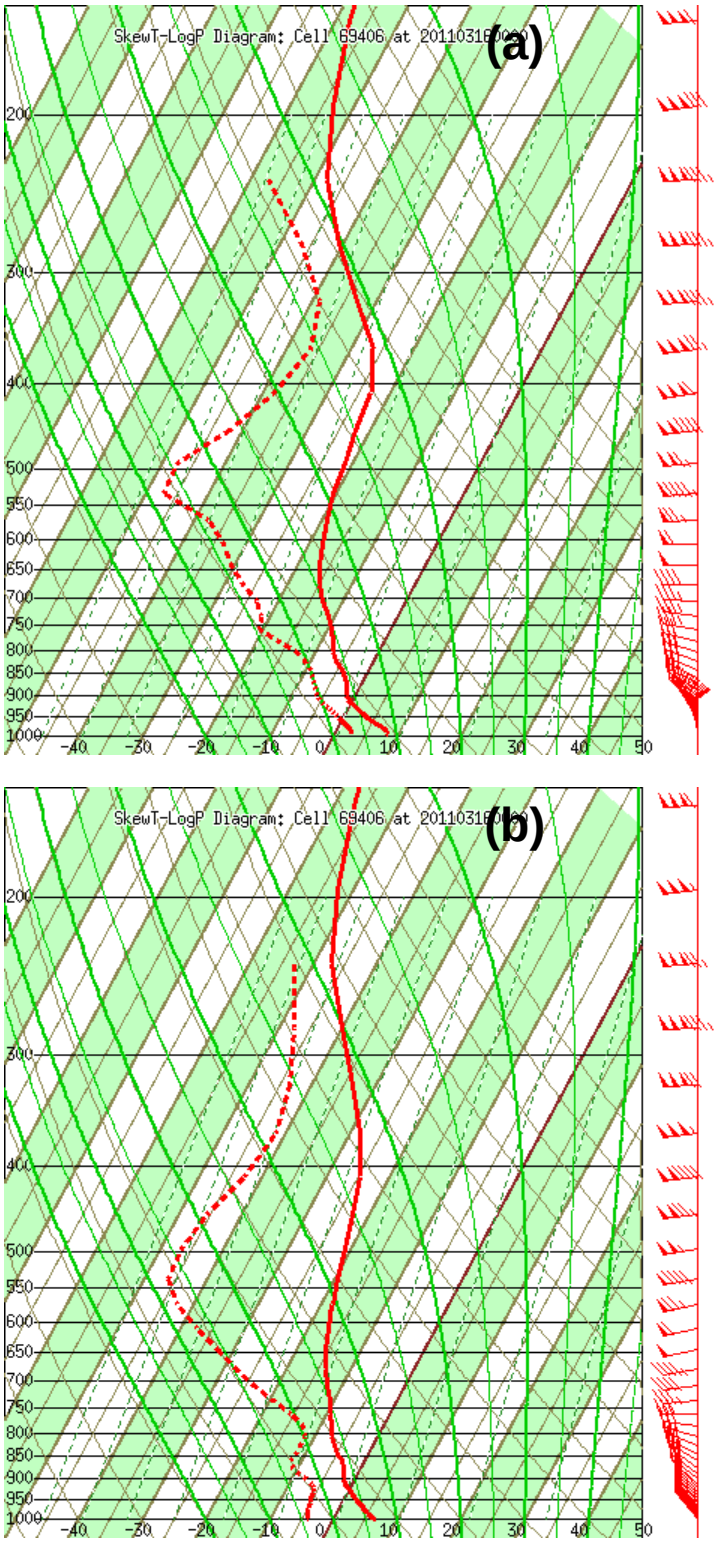

Figure 2.21 Comparison of Tateno sounding at 00 UTC 16 March 2011. (a) ECMWF 0.141° x 0.141° analysis. (b) OMEGA 30-hour forecast.

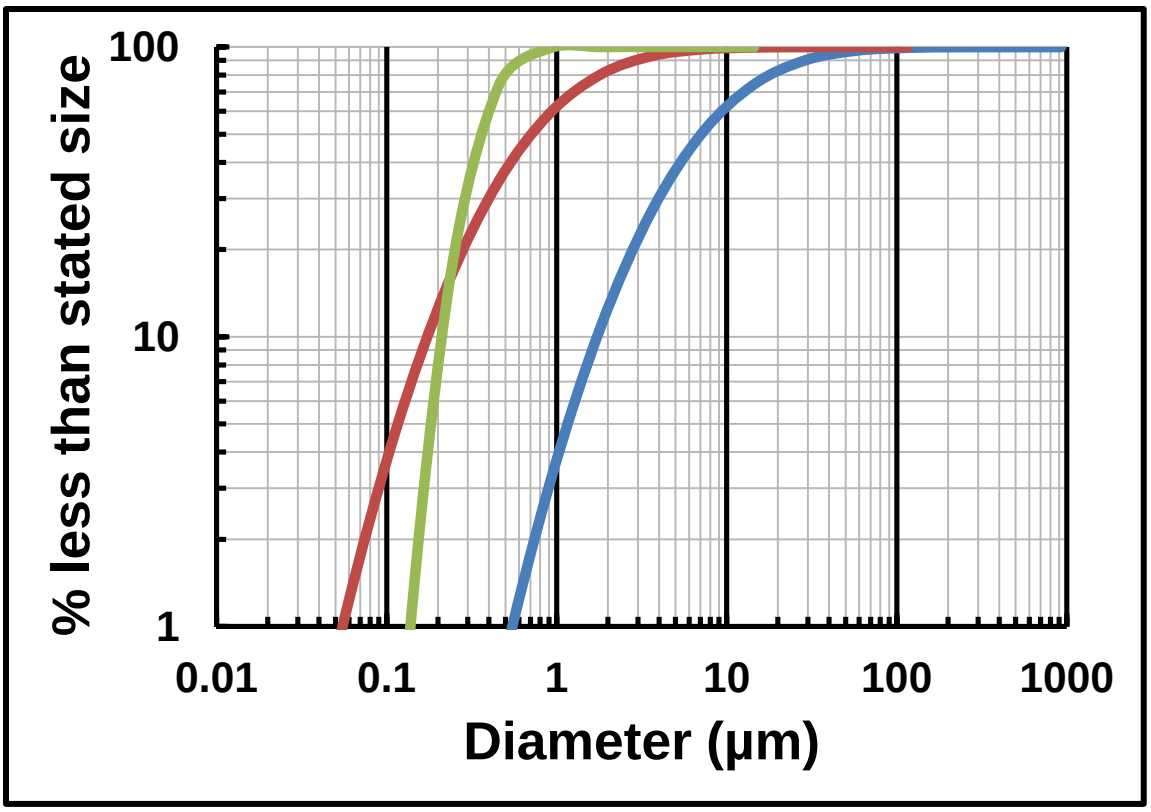

Figure 2.22 Cumulative distributions for the log normal-distributed PSDs used in the Terada and Stohl source terms (after Seinfeld and Pandis 2006). The MMD and σ_g of the PSDs are depicted by colored lines. Green line shows the PSD used for all emission periods in the baseline simulation and cloud microphysics sensitivity study and for all non-explosive periods in the aerosol sensitivity study (MMD=0.5 μm, σ_g= 1.5). Red and blue lines show the PSDs used for the explosive periods in the aerosol PSD sensitivity study (MMD=1.0 μm, σ_g = 3.0 and MMD=10.0 μm, σ_g = 3.0, respectively).

Table 2.1 Process notations referenced with the source and sink terms parameterized in the Milbrandt & Yau scheme used in OMEGA.

Process Notation	Description of source / sink terms
NU_{vc}	Nucleation of cloud water
VD_{vc}	Condensation and evaporation of cloud water
NU_{vi}	Primary nucleation of cloud ice
VD_{vi}	Deposition and sublimation of cloud ice
VD_{vr}	Condensation and evaporation of rain
VD_{vs}	Deposition and sublimation of snow
CL_{ci}	Collection of cloud water by ice
ML_{ic}	Melting of cloud ice to form cloud water
FZ_{ci}	Homogeneous freezing of cloud ice
CL_{cs}	Collection of cloud water by snow
CN_{ig}	Conversion of cloud ice to graupel
VD_{vg}	Deposition and sublimation of graupel
VD_{vh}	Deposition and sublimation of hail
CL_{sh}	Collection of snow by hail
CN_{cr}	Autoconversion of cloud water to rain
CN_{is}	Autoconversion of cloud ice to snow
CL_{cg}	Collection of cloud water by graupel
CL_{ih}	Collection of cloud ice by hail
ML_{gr}	Melting of graupel to rain
CN_{gh}	Conversion of graupel to hail
ML_{sr}	Melting of snow to rain
CL_{sr}	Collection of snow by rain
CL_{ch}	Collection of cloud water by hail
CN_{sg}	Conversion of snow to graupel
CL_{rs}	Collection of rain by snow
CL_{rh}	Collection of rain by hail
ML_{hr}	Melting of hail to rain
SH_{hr}	Shedding from hail to rain
CL_{ri}	Collection of rain by ice
CL_{ir}	Collection of ice by rain
$CL_{sr\text{-}g}$	Collection of snow by rain for graupel
$CL_{sr\text{-}h}$	Collection of snow by rain for hail
$CL_{ir\text{-}q}$	Collection of ice by rain for graupel
$CL_{ir\text{-}h}$	Collection of ice by rain for hail
CL_{rr}	Rain self-collection
CL_{ss}	Snow self-collection

Table 2.2 Suite of seven global meteorological datasets used to create and test initial and lateral boundary conditions for the OMEGA simulations.

Global Meteorological Dataset	Horizontal Resolution	Time Resolution
GFS Operational Analysis	1.0°	3-hourly
GFS Operational Analysis	0.5°	6-hourly
GFS Final Analysis	1.0°	"
NOGAPS Operational Analysis	1.0°	"
ECMWF Operational Analysis	0.141°	"
JMA GPV Operational Analysis	0.5°	"
NCEP/NCAR Reanalysis	2.5°	"

CHAPTER 3. MODEL RESULTS

3.1 March 11−17, 2011 simulation

Two baseline dispersion simulations were performed that were identical in all respects (i.e., identical OMEGA weather input and dispersion model setup parameters) except for the input source terms used to specify the amount, rate, and release height of the radioactive material. The Stohl baseline simulation used the estimated emissions of ^{137}Cs obtained a posteriori by the inversion method reported in Stohl et al. (2012). The Terada baseline simulation used the estimated emissions of ^{137}Cs comprising the "refined" source term reported in Terada et al. (2012).

Synoptic scale plots of the cumulative surface wet and dry deposition patterns at 24-hour intervals from the Stohl and Terada baseline simulations are presented in the following figures, where the cumulative surface wet deposition fields reflect surface deposition due to precipitation scavenging of radioactive material by rain, snow, and graupel. The deposition plots are accompanied by the corresponding Japan Meteorological Agency (JMA) mean sea level pressure analyses to orient the reader and provide a graphical depiction of the evolving synoptic weather features.

The cumulative surface dry deposition field shown in Figure 3.1 reflects the difference in emission start times and release altitudes between the two source terms in the first 24-hour period of the release. The Terada source term emission starts at 2000 UTC 11 March and injects material from 20 m AGL. The Stohl source term emission commences five hours earlier at 1500 UTC 11 March and injects material from three altitudes (50, 300, and 1000 m AGL), which is subsequently borne by offshore flow associated with synoptic scale high pressure building from the southwest over Japan

shown in Figure 3.2. Stohl et al. (2012) associate the initial release of radioactive material less than eight hours after the power blackout at the Fukushima Daiichi facility with increased radiation observed in the turbine hall of Unit 1 and with manual venting activities that were aimed at reducing the pressure inside the containment structure. In contrast, Terada et al. (2012) based the start of their emissions on estimates made by Kitata et al. (2012), which incorporated the earliest available dust sampling data from locations near the accident site in Takase, Kawazoe, and Otabashi.

During the 24-hour period ending 00 UTC 13 March, the signature of the first hydrogen explosion in each source term is reflected in the respective surface deposition fields in Figure 3.3. The onset of a sea breeze circulation in relatively weak surface flow associated with high pressure (Figure 3.4) at the time of the explosion (06 UTC 12 March) caused the plume of explosion debris to veer inland over time and deposit on the surface in a well-defined pattern extending northwestward from the power station. Afterwards, the plume continued to veer northward and eventually seaward as a land breeze circulation set in. The relatively larger area of surface deposition associated with the Stohl source term is due to the explosion debris being lofted through the boundary layer from emission heights at 50, 300, and 1000 m AGL over several hours compared with the Terada source term simulation, which confined the emissions of the explosion debris to heights at and below 100 m AGL over a period of 30 minutes.

The cumulative deposition fields for the next 24-hour period ending 00 UTC 14 March shown in Figure 3.5 largely reflect the influence of continuous offshore flow relative to the site of the accident as the high pressure center that was located over Japan moved east of 150°E as shown in Figure 3.6.

The dry and wet deposition fields for the 24-hour period ending 00 UTC 15 March in Figure 3.7 and Figure 3.8, respectively, show the influence of three events. The first event is the strong hydrogen explosion observed in Unit 3 (~02 UTC 14 March), which again lofted explosion debris through the boundary layer in the Stohl source term simulation but which was confined to relatively lower injection altitudes (≤300 m AGL) in the Terada source term simulation. The second event was an internal explosion in the Unit 2 reactor (~21 UTC 14 March) that released a relatively large amount of radioactive material, but at low altitude in both simulations. The third event involved the interaction of the emissions with the changing character of the synoptic scale flow affecting southern and eastern Japan. The synoptic scale flow transitioned during 14 March from the waning influence of surface high pressure to a synoptic pattern governed by a developing area of low pressure along and east of the Pacific coast (Figure 3.9). The influence of the developing low pressure system on the surface wind field and emissions is reflected in the distinct extension of the dry deposition patterns in both simulations southwestward toward Tokyo and in the wet deposition patterns far offshore.

Dry and wet deposition of radioactive material increased offshore and spread inland for the period ending 00 UTC 16 March (Figure 3.10 and Figure 3.11, respectively). During this period widespread precipitation developed over central Japan in association with a surface low pressure area, which migrated eastward through Honshu and intensified offshore (Figure 3.12). The interaction of the plumes with the precipitation area suggests that the higher emission rates and heights associated with the Stohl source term dispersed radioactive material through a greater depth of the atmosphere where it was scavenged by rain, snow, and graupel. In contrast, the plume

dispersing from the Terada source term is relatively lower and scavenged preferentially by rain.

By the 24-hour period ending 00 UTC 17 March, the low pressure area that traversed Honshu had merged with a broad area of low pressure off of the eastern coast of Japan and intensified rapidly as it moved northeastward toward Kamchatka. In response to the rapid intensification of the low pressure center over the open ocean northeast of Hokkaido shown in Figure 3.15, central and northern Japan experienced reduced precipitation and cold advection accompanying strong northwesterly winds.

Due to the strong offshore winds and reduced emissions and precipitation, wet and dry deposition decreased over inland areas while dry deposition continued offshore. The sustained dry deposition in offshore flow resulted in a prominent lobe of surface deposition over the ocean in Figure 3.13 that extends southeastward from the accident site in both the Stohl and Terada simulations. By contrast, wet deposition had largely ceased in the computational domain as evidenced by the relatively small change in cumulative surface deposition from the previous 24-hour period in Figure 3.14.

The percentage contributions of cumulative surface wet deposition at 00 UTC 17 March 2011 due to scavenging of ^{137}Cs by rain, snow, and graupel are presented in Figure 3.16. It is interesting to note that the emissions from the Stohl source term are scavenged preferentially by rain (70%) and graupel (30%), with very little scavenging by snow compared with the Terada source term, which was scavenged preferentially by rain. Although the Stohl source term releases a factor of seven more radioactive material into the atmosphere compared with the Terada source term, when differentiated by release height, 40%, 55%, and 5% of this material is released from 50, 300, and 1000 m AGL,

respectively. By comparison, all of the material in the Terada source term was released at or below 300 m AGL (e.g., ~70%, 5%, 20%, and 5% from 20, 100, 120, and 300 m AGL, respectively). Considering the comparatively high percentage of scavenging by rain using the Terada source term, it would appear that the release height is the driving factor for differentiating between rain, snow, and graupel scavenging.

An analysis of the cumulative wet vs. dry deposition for the six-day simulation period showed surface deposition of radioactive material due to dry deposition to be two orders of magnitude larger than that from wet deposition and hence the dominant removal process during the first week of the accident. The relative contributions from wet and dry deposition should be viewed in light of the fact that deposition is a continuous removal process and the first four days of the accident were free of precipitation in the area surrounding the nuclear plant.

In addition, as shown in Figure 3.17, the percentage of wet versus dry deposition over time depends on the source term used and on the threshold value of the cumulative surface deposition used to evaluate the percentage. For example, assuming a threshold maximum cumulative surface deposition of 10^1, 10^2, 10^3, 10^4, and 10^5 Bqm^{-2} for the Stohl source term, wet deposition comprises a maximum of approximately 90, 70, 40, 10, and 1%, respectively of the total surface deposition over time. At threshold values of 10^6 and 10^7 Bqm^{-2} however, dry deposition dominates wet deposition by 220:1 and 287:1, respectively. For the Terada source term, threshold values of 10^1, 10^2, 10^3, and 10^4 result in wet deposition percentages of 60, 20, 10, and 2%, respectively. Threshold values of 10^5, 10^6, and 10^7 Bgm^{-2} reveal that dry deposition is also the dominant process compared with wet deposition for the Terada source term with dry to wet ratios of 120:1, 195;1, and

263:1, respectively. Dry processes result in relatively large fractions of surface deposition near the source in the OMEGA simulations, where the large contribution by dry deposition at higher threshold maximum surface cumulative depositions (e.g., 10^6, 10^7 Bqm^{-2}) masks the percentage of wet deposition at relatively lower thresholds. This analysis shows that at lower threshold maximum values of surface deposition, wet deposition can be a dominant removal process. In fact, in regions with very small amounts of surface deposition, wet deposition appears to play a bigger role, while in high deposition zones, wet processes are somewhat inconsequential.

A comparison of the observed deposition pattern of ^{137}Cs shown in Figure 3.18 with the simulated cumulative surface wet and dry deposition patterns presented in Figure 3.19 and Figure 3.20 shows that the model did a reasonably good job in predicting the deposition pattern using both source terms during the dry phase of the accident (11 March–14 March) when dry deposition was the dominant removal process. It is suggested that this agreement is because of the weather model's ability to simulate the extent and timing of onshore flow associated with a sea breeze circulation that developed around the time of the first reactor explosion.

Figure 3.21 shows a simulated surface meteogram located at the Fukushima Daiichi nuclear power station. Onshore flow during the period 00 to 12 UTC 12 March is evident in the time series of wind direction. Three-hourly snapshots of the predicted surface winds and dispersing plumes for the same period, together with the accompanying cumulative surface dry deposition patterns shown in Figures 3.22–Figure 3.26, suggest that the surface pattern of explosion debris was deposited in association with the simulated inland penetration of the sea breeze. Due to power outages after the

earthquake, Fukushima is the only station with observational data for this period; however, the observation station is located in an inland valley and the surface meteogram (Figure 3.28) does not reflect the influence of onshore flow.

During the wet phase of the accident (March 15–March 16), Figure 3.20 shows that the pattern is not as well predicted. It is suggested that this discrepancy is because of differences between model predicted and observed precipitation distributions. Figure 3.34 shows the cumulative surface wet and dry deposition at 00 UTC 16 March at the end of the wet phase of the accident. It is apparent that dry deposition was the dominant process contributing to the overall surface pattern of radioactive material. In spite of a fair prediction of the onset of precipitation at Iitate (Figure 3.27), Fukushima (Figure 3.28), and Koriyama (Figure 3.30) on 15 March, a comparison of the observed precipitation distribution (Figure 3.31 and Figure 3.32) with model-predicted surface precipitation fields (Figure 3.33) shows that the model develops precipitation much earlier. As a result, the plume of radioactive material encounters precipitation earlier and over a broad area and the resulting wet deposition pattern shown in Figure 3.34 is very diffuse.

Nonetheless, as shown in Figure 3.35, precipitation scavenging was active near the source on the grid defined by the NNSA aircraft observations during the wet phase of the accident, and it is interesting to note that radioactive material is deposited preferentially by rain and graupel for both source terms. The lack of scavenging by snow may be explained by the relatively lower heights of the emissions nearer the source.

The OMEGA prediction of the surface deposition pattern during the dry phase of the accident was in reasonably good agreement with the observed surface deposition pattern shown in Figure 3.18. In order to assess whether the magnitude of the simulated

pattern was also in agreement with observations, a subset of four NNSA aircraft transects of roughly north/south orientation that comprise a portion of the observed surface deposition pattern (Figure 3.18) were extracted and evaluated. The four transects are shown in Figure 3.36. Transect T1 was chosen because it crosses the site of the accident. Transect T2 crosses the observed surface pattern to the northwest of the accident site. Transect T3 crosses the pattern at the location (depicted by a black triangle) of the observed maximum value of the surface deposition. Finally, transect T4 crosses the surface pattern at a substantial distance downwind of the accident site. Transects T1 and T2 started over the ocean north of the accident and were flown in a southwesterly direction whereas transects T3 and T4 started over land south of the accident site and were flown in a northerly direction. A comparison of the transects reveals that both OMEGA patterns are shifted northward of the observed surface pattern, with the Terada source term depositing less material than the Stohl source term.

Figure 3.37 shows comparisons of the magnitudes of surface deposition along each of the four transects. For example, Figure 3.37a, Figure 3.37b, Figure 3.37c, and Figure 3.37d compare the magnitude of the surface deposition from the NNSA observations with results from the OMEGA Stohl and Terada source terms for transects T1, T2, T3, and T4, respectively.

The deposition signature at the accident site is apparent in both OMEGA results in Figure 3.37a, however the maximum is over and under predicted by the OMEGA Stohl and Terada source terms, respectively, by approximately an order of magnitude. Also, the OMEGA surface depositions along transect T1 fall off more rapidly compared with the NNSA observations. The OMEGA surface depositions are in good agreement with the

observations on transect T2 in Figure 3.37b until reaching the location of the observed maximum, but again fall off too rapidly thereafter. Figure 3.37c shows that the OMEGA Stohl result was within an order of magnitude or better of the NNSA observations for most of transect T3. In contrast, the Terada result significantly under predicted the observation for more than half of the transect. Finally, Figure 3.37d shows that both source terms under predicted the observed surface deposition along transect T4 by up to three orders of magnitude at some locations.

The OMEGA predictions are sensitive to the amount and emission height of the radioactive material. Other factors such as the atmospheric stability and wind speed in the boundary layer or the model resolution of the underlying topography may also influence the distribution of the simulated surface deposition patterns. Since the OMEGA surface patterns resulting from dry deposition during the dry phase of the accident were shifted northward from the observed pattern, the structure of the boundary layer was examined.

Figure 3.38 shows a time series at hourly intervals of the temperature, dewpoint, and winds at and below 700 hPa for the period 00–06 UTC 12 March. The time series is a subset of the 3-hourly snapshots in Figure 3.22–Figure 3.24 that show the inland dispersion of the puff centroids in onshore flow. For comparison, Figure 3.39 and Figure 3.40 show hourly time series of potential temperature and wind speed, respectively, in the lowest 3 km of the troposphere centered on the accident site.

The SkewT-logP diagrams indicate that the boundary layer became capped by a cloud layer over time while the cross sections of potential temperature clearly show the influence of the onshore flow on the thermal structure. On closer examination of the model results, the static stability of the boundary layer was found to be weakly unstable

below approximately 600 m AGL and statically stable above. Also, in response to a time-varying land-sea surface temperature difference that reached a maximum of 4°C during the time series, a logarithmic wind profile developed near the surface (Figure 3.40). The evolved structure of the boundary layer during this time period, including subtle features in the profile of virtual potential temperature at 04 UTC, suggests that a thermal internal boundary layer developed over land in onshore flow (Hsu 1988, Stull 1988) that may have promoted fumigation or looping of the effluent plume of radioactive materials. Hence, the stability of the boundary layer was such that surface deposition by dry processes would be likely, if not enhanced.

The northward shift in the OMEGA surface patterns may simply be due to the fact that the OMEGA model minimum grid spacing of 3 km was insufficient to resolve the influence of the terrain and roughness length, and therefore the effects of surface friction, on the structure of the boundary layer wind field west and northwest of the accident site. As a result, the inland dispersing plume likely veered with time too rapidly, which displaced the modeled surface deposition pattern northward compared with observations.

3.2 Cloud microphysics sensitivity

Two simulations were performed that were identical in all respects (i.e., identical OMEGA weather input and dispersion model setup parameters) except that the first simulation used a single-moment option of the cloud microphysics scheme whereas the second simulation used a double-moment option of the scheme. The test was performed to gauge the sensitivity of the surface deposition fields to a change in the manner in which the total number distribution per unit volume of the hydrometeor fields is calculated. The number distribution is an important parameter because it is used to

determine the mass-mean diameter used in the calculation of the precipitation rates for rain, snow, and graupel fields in the precipitation scavenging parameterization.

Synoptic scale plots of the cumulative surface wet and dry deposition patterns at 00 UTC 17 March 2011 from the Stohl and Terada microphysics sensitivity simulations are presented in the following figures, where the cumulative surface wet deposition fields reflect surface deposition due to precipitation scavenging of radioactive material by rain, snow, and graupel.

A comparison of the cumulative dry deposition patterns (Figure 3.13 vs. Figure 3.41) shows that neither of the inland patterns are sensitive to the choice of using the double-moment cloud microphysics parameterization. Over the open ocean, only the Terada source term appears to show some sensitivity, which is manifested in enhanced dry deposition east of the Fukushima site to 148°E.

The physical processes in the cloud microphysics and cumulus parameterizations can have an impact on storm and cloud dynamics through latent heating. Additionally, the use of a parameterization for explicit microphysics may have an impact on the cloud and storm environment through the process of mass loading by precipitation. Hence, one can speculate that the use of the double-moment scheme affects the atmospheric stability in the boundary layer over the ocean leading to enhanced dispersion and deposition.

A comparison of the cumulative wet deposition patterns at synoptic scale (Figure 3.14 vs. Figure 3.42) shows that neither the inland nor open ocean patterns are sensitive to the choice of using the double-moment cloud microphysics parameterization. However, a quantitative comparison of the percentage contributions of cumulative surface wet deposition (Figure 3.16 vs. Figure 3.43) shows that scavenging of radioactive

material by rain and snow are somewhat enhanced at the expense of the graupel field for the Stohl source term.

On the scale of the NNSA aircraft grid (Figure 3.18), the results show more sensitivity to the choice of microphysics scheme (Figure 3.35 vs. Figure 3.44). For example, the Terada source term result, which showed roughly a 50% split between rain and graupel scavenging using the single-moment scheme, shifted to 70% rain and 30% graupel for the double-moment scheme.

3.3 Aerosol PSD sensitivity

Two simulations were performed that were identical in all respects (i.e., identical OMEGA weather input and dispersion model setup parameters) except that the ^{137}Cs release in the first set of simulations (hereinafter, PSDE1) used a PSD characterized by MMD = 1.0 μm, σ_g = 3.0 while the ^{137}Cs release in the second set of simulations (hereinafter, PSDE2) used a PSD characterized by MMD = 10.0 μm, σ_g = 3.0. In each of these simulations, the PSD was broadened (Figure 2.22) at all emission heights during explosive periods of the accident to represent a postulated increase in the number of particle sizes associated with an explosive particulate cloud. Both simulations used the double-moment option of the cloud microphysics scheme.

A test was performed to gauge the sensitivity of the surface deposition fields to a change in the PSD of the source during explosive events. The timing of the explosive events are discussed at length in Stohl et al. (2012) and Terada et al. (2012) and spanned roughly 0600–0900 UTC 12 March, 0000–0300 UTC 14 March, and 2100 UTC 14 March–0000 UTC 15 March in the Stohl source term and 0630–0700 UTC 12 March and

0200–0230 UTC 14 March in the Terada source term.

Synoptic scale plots of the cumulative surface wet and dry deposition patterns at 00 UTC 17 March 2011 from the Stohl and Terada explosion sensitivity simulations are presented in the following figures, where the cumulative surface wet deposition fields reflect surface deposition due to precipitation scavenging of radioactive material by rain, snow, and graupel.

A comparison of Figure 3.13 (no explosion PSD) vs. Figure 3.45 (PSDE1) vs. Figure 3.48 (PSDE2) reveals that broadening the effluent PSD during explosive events has little impact on the cumulative surface dry deposition patterns at this scale. Only the Terada source term dry deposition pattern shows reduced deposition east of the Fukushima facility out over the ocean.

The cumulative wet deposition patterns using the Stohl source term exhibit a high degree of sensitivity (Figure 3.14 vs. Figure 3.47 vs. Figure 3.49) when considering the change in PSD due to explosive periods of the accident. In contrast, the Terada source term shows very little sensitivity. In fact, a comparison of the percentage contributions of cumulative surface wet deposition (Figure 3.16 vs. Figure 3.47 vs. Figure 3.50) reveals that 1) for the Stohl source term, as the MMD of the PSD increases and the PSD is broadened, precipitation scavenging by snow increases dramatically, from 5% to 50%, primarily at the expense of scavenging by rain, which decreases from 80% to 30%; and 2) for the Terada source term, radioactive material is scavenged preferentially by rain despite the change in effluent PSD.

Increasing the MMD and σ_g during explosive periods ostensibly extends the effluent PSD to smaller and larger aerosol size categories, which promotes wet deposition

by the processes of diffusion and inertial capture when using Slinn's scavenging parameterization. In addition, the emission height likely controls what type of precipitation (rain, snow, or graupel) is encountered by a lofted aerosol-bound radionuclide, at least nearer the source. Hence, the results of the explosion PSD sensitivity study show that including precipitation scavenging that is differentiated by precipitation type is as important as specifying the correct emission height.

Figure 3.51 and Figure 3.52 show that the percentage of wet versus dry deposition over time depends on the PSD used and on the threshold value of the cumulative surface deposition used to evaluate the percentage. For example, assuming a threshold maximum cumulative surface deposition of 10^1, 10^2, 10^3, 10^4, and 10^5, 10^6, and 10^7 Bqm^{-2}, wet deposition in the non-explosion PSD case comprises a maximum of approximately 90, 70, 40, 10, and 1%, respectively of the total surface deposition over time. For the Terada source term, threshold values of 10^1, 10^2, 10^3, and 10^4 result in wet deposition percentages of 60, 20, 10, and 2%, respectively. For the PSDE1 and PSDE2 explosion cases, the percentage of wet deposition in the smaller threshold categories remains relatively unchanged for both the Stohl and Terada source terms in contrast to the larger threshold categories. The larger categories in general show small increases in the percentage of wet deposition. The increased percentages of wet deposition at larger thresholds may be due to the increase of radioactive material bound to aerosols in larger size categories and the abrupt increase in the collision efficiency in the Slinn scavenging model for aerosol sizes above 10 microns.

It is evident in Figure 3.17, Figure 3.51, and Figure 3.52 that the percentage of wet to dry deposition has a very large spatial variation. In order to gauge the time

variation of the wet to dry percentage, a point downwind from the accident site was evaluated for surface deposition by wet and dry processes for each of the explosion PSD cases. Figure 3.53 and Figure 3.54 show the time-varying cumulative wet and dry deposition at the location of the NNSA observed surface deposition maximum on Transect T3 shown in figure 3.36c. The Stohl source term result shows that dry deposition remains relatively unchanged at this location given the change in the PSD due to explosions. In contrast, wet deposition increases by an order of magnitude. Comparatively, the Terada source term shows no increase in wet deposition and small changes in dry deposition.

On the horizontal scale of the NNSA aircraft deposition grid, precipitation scavenging of the Terada source term again shows little sensitivity to the change in PSD accompanying explosive periods (Figure 3.35 vs. Figure 3.55 vs. Figure 3.56), with wet deposition due preferentially to rain. Since the NNSA observations are confined to the area surrounding the accident site, the Terada results suggest that the relatively lower emission heights play a factor in determining the type of precipitation that scavenges the plume.

The results for the Stohl source term on the NNSA grid suggest that the influence of emission height is also a factor. The maximum emission height in the Stohl source term during explosive periods is 1000 m AGL. Hence, it appears that the radioactive material is scavenged preferentially by snow over rain as the explosion PSD increases (10% vs. 60%).

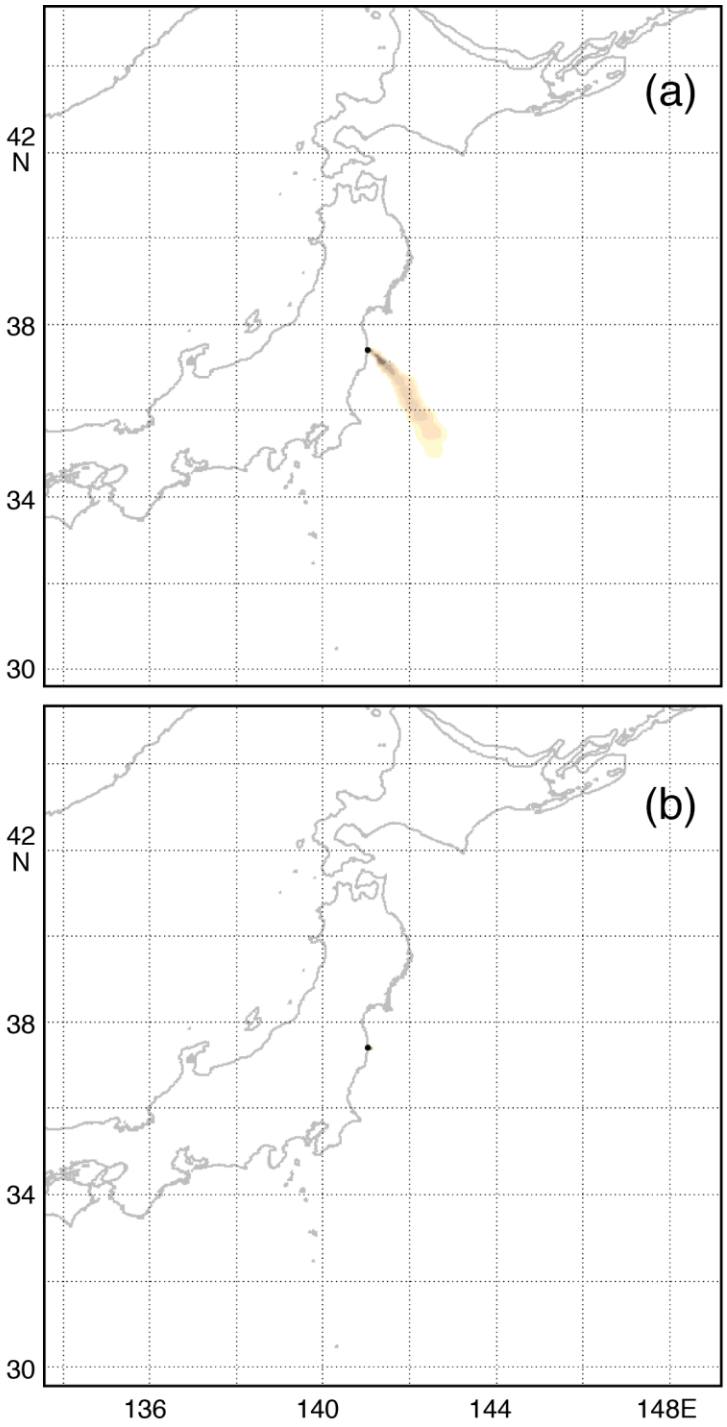

Figure 3.1 Cumulative surface deposition at 00 UTC 12 March 2011 due to dry deposition for (a) Stohl source term and (b) Terada source term. Contours intervals are 10^1, 10^2, 10^3, 10^4, 10^5, 10^6, 10^7 Bqm^{-2}. Black circle indicates the location of the Fukushima Daiichi nuclear power station.

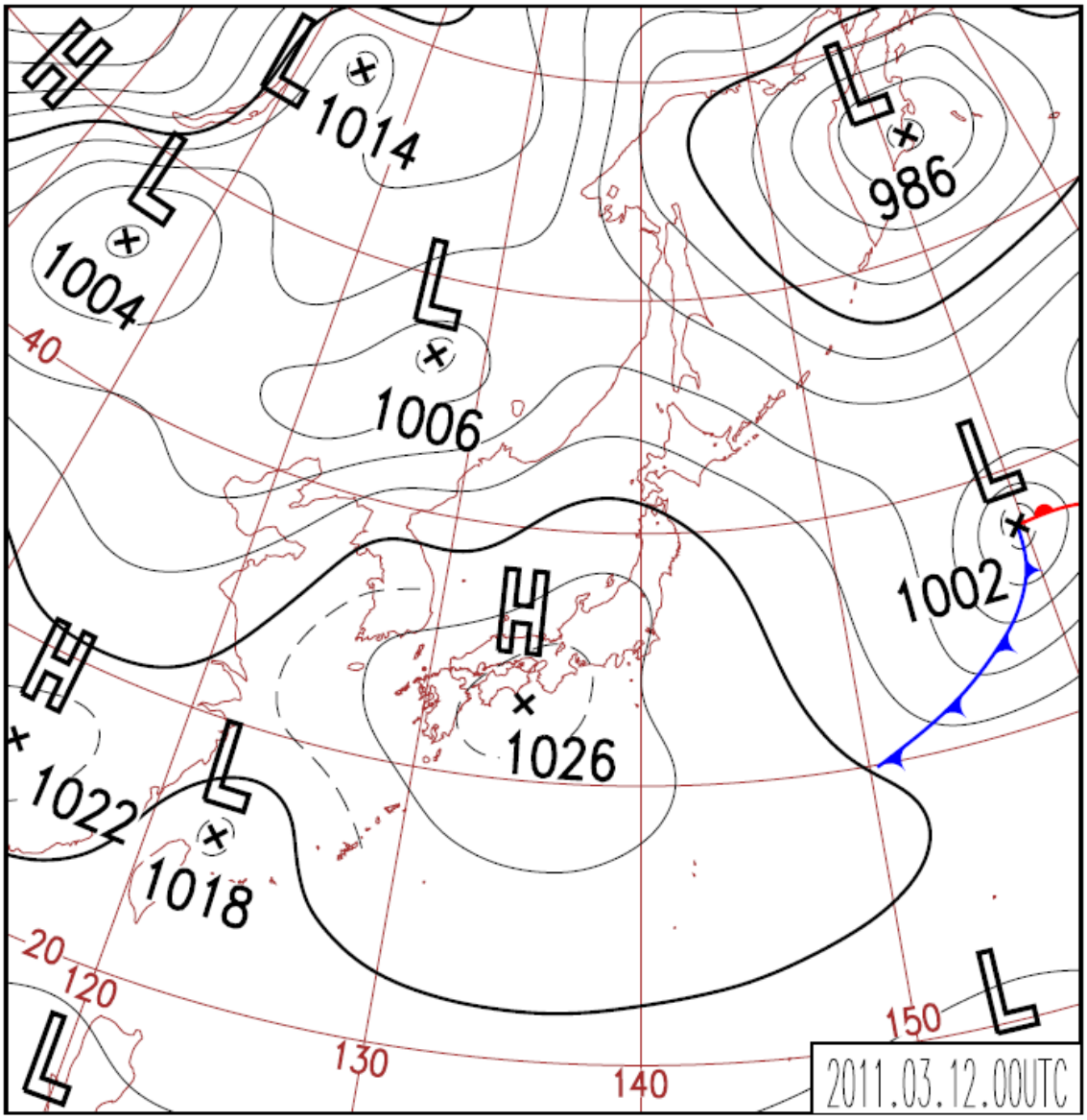

Figure 3.2 JMA surface analysis (hPa) valid 00 UTC 12 March 2011. Contour interval is 4 hPa.

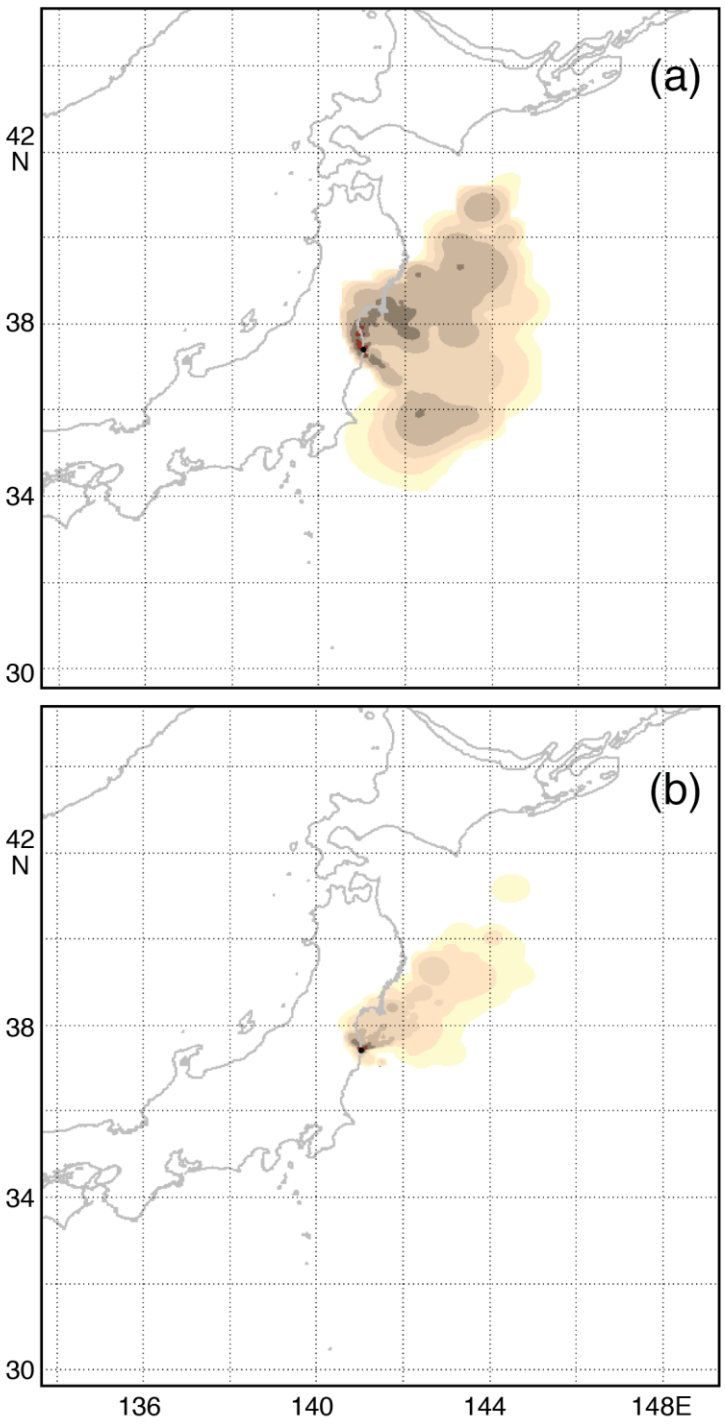

Figure 3.3 As in Figure 3.1, but for 00 UTC 13 March 2011.

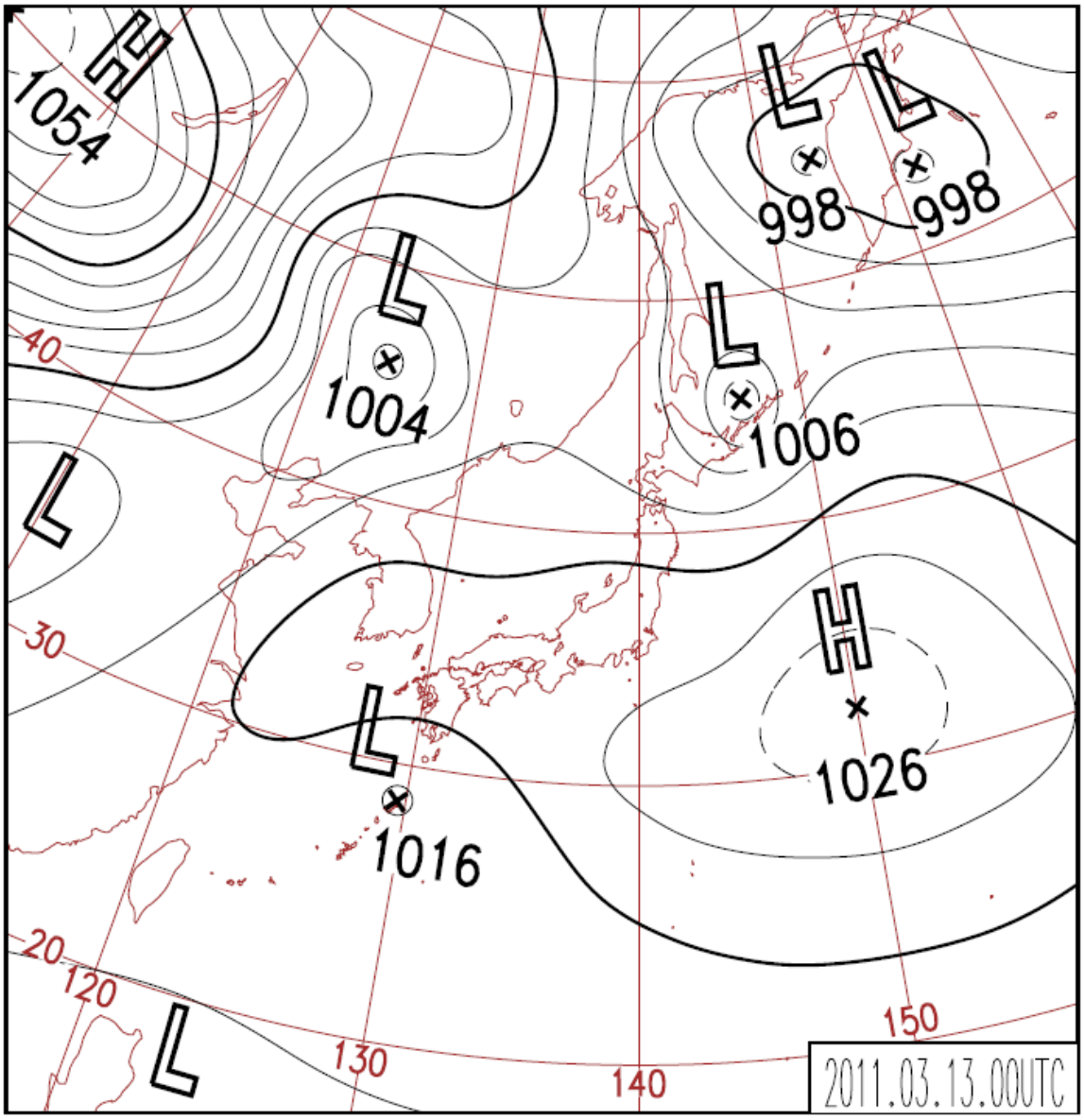

Figure 3.4 JMA surface analysis (hPa) valid 00 UTC 13 March 2011.

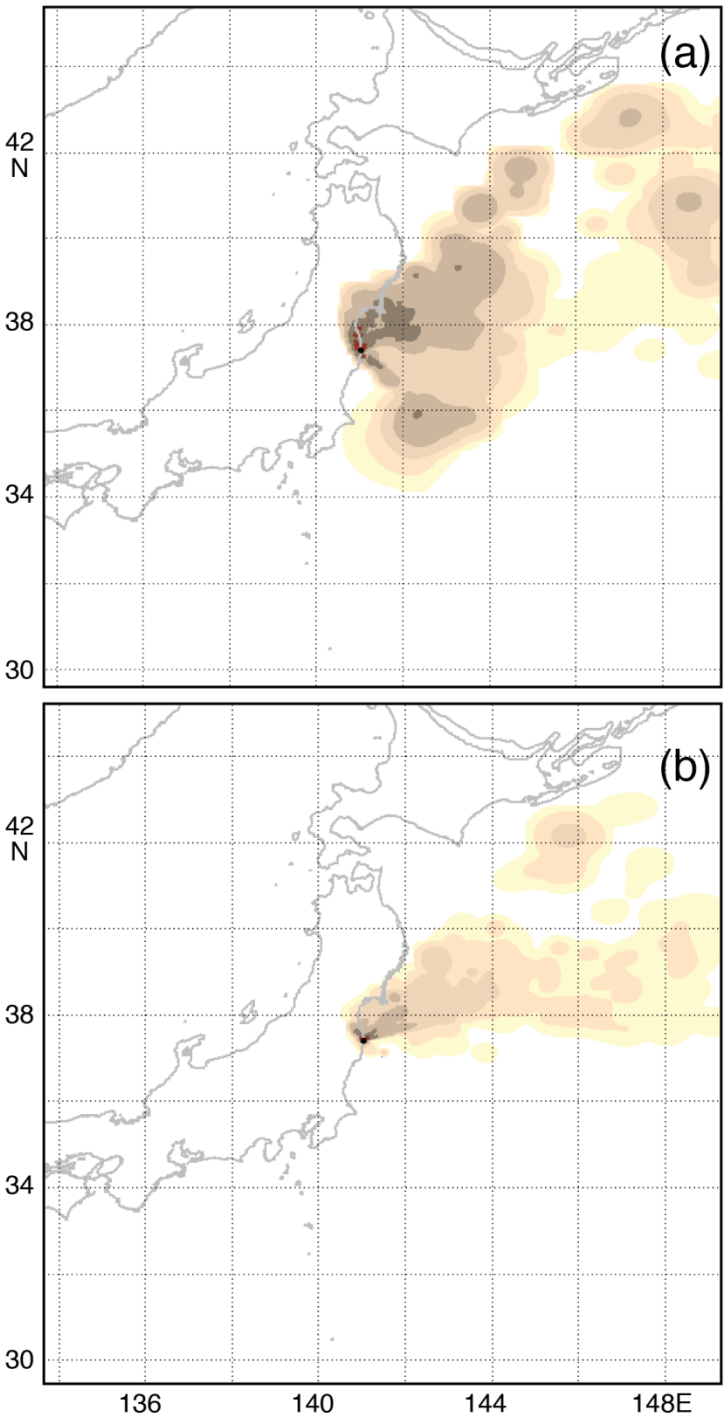

Figure 3.5 As in Figure 3.1, but for 00 UTC 14 March 2011.

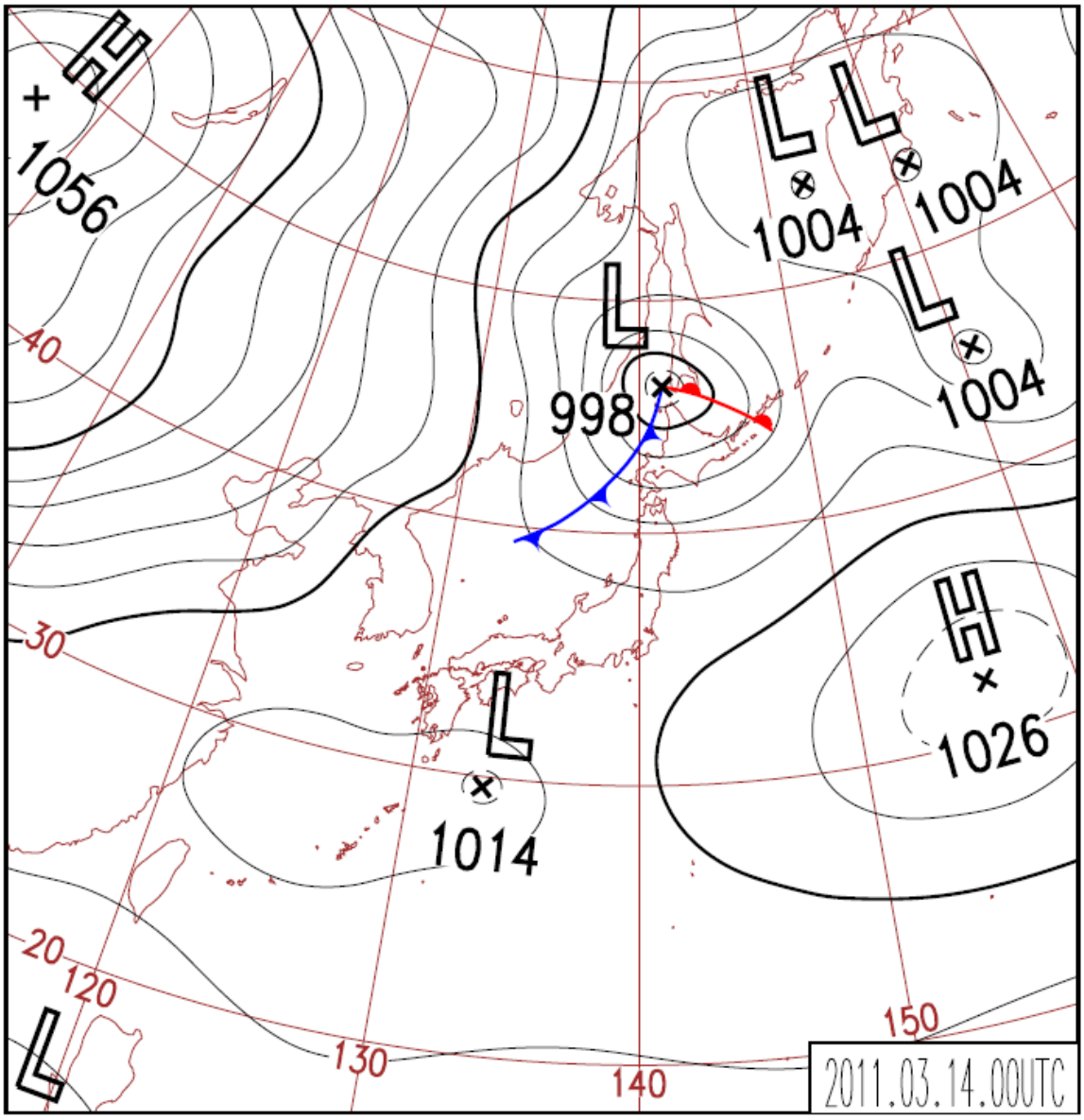

Figure 3.6 JMA surface analysis (hPa) valid 00 UTC 14 March 2011. Contour interval is 4 hPa.

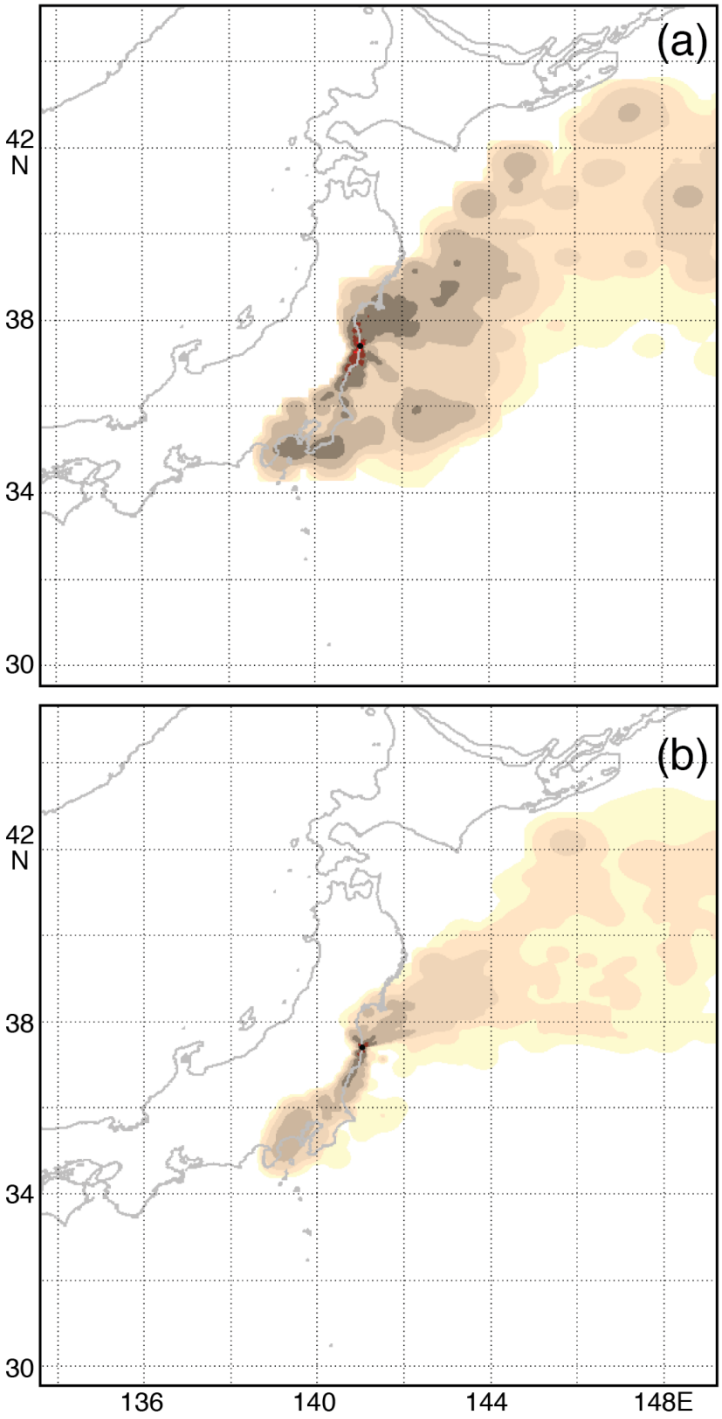

Figure 3.7 As in Figure 3.1, but for 00 UTC 15 March 2011.

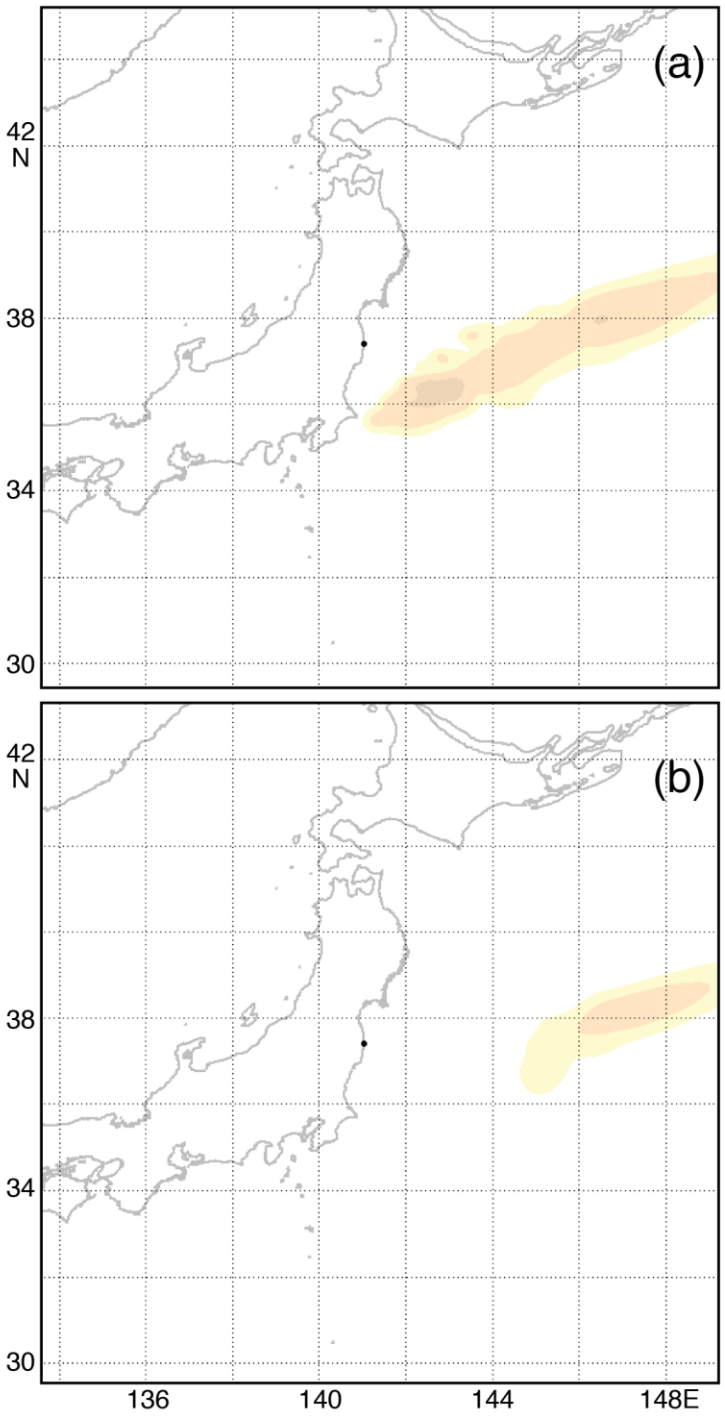

Figure 3.8 Cumulative surface deposition at 00 UTC 15 March 2011 due to wet deposition for (a) Stohl source term and (b) Terada source term. Contour intervals are 10^1, 10^2, 10^3, 10^4, 10^5, 10^6, 10^7 Bqm^{-2}. Black circle indicates the location of the Fukushima Daiichi nuclear power station.

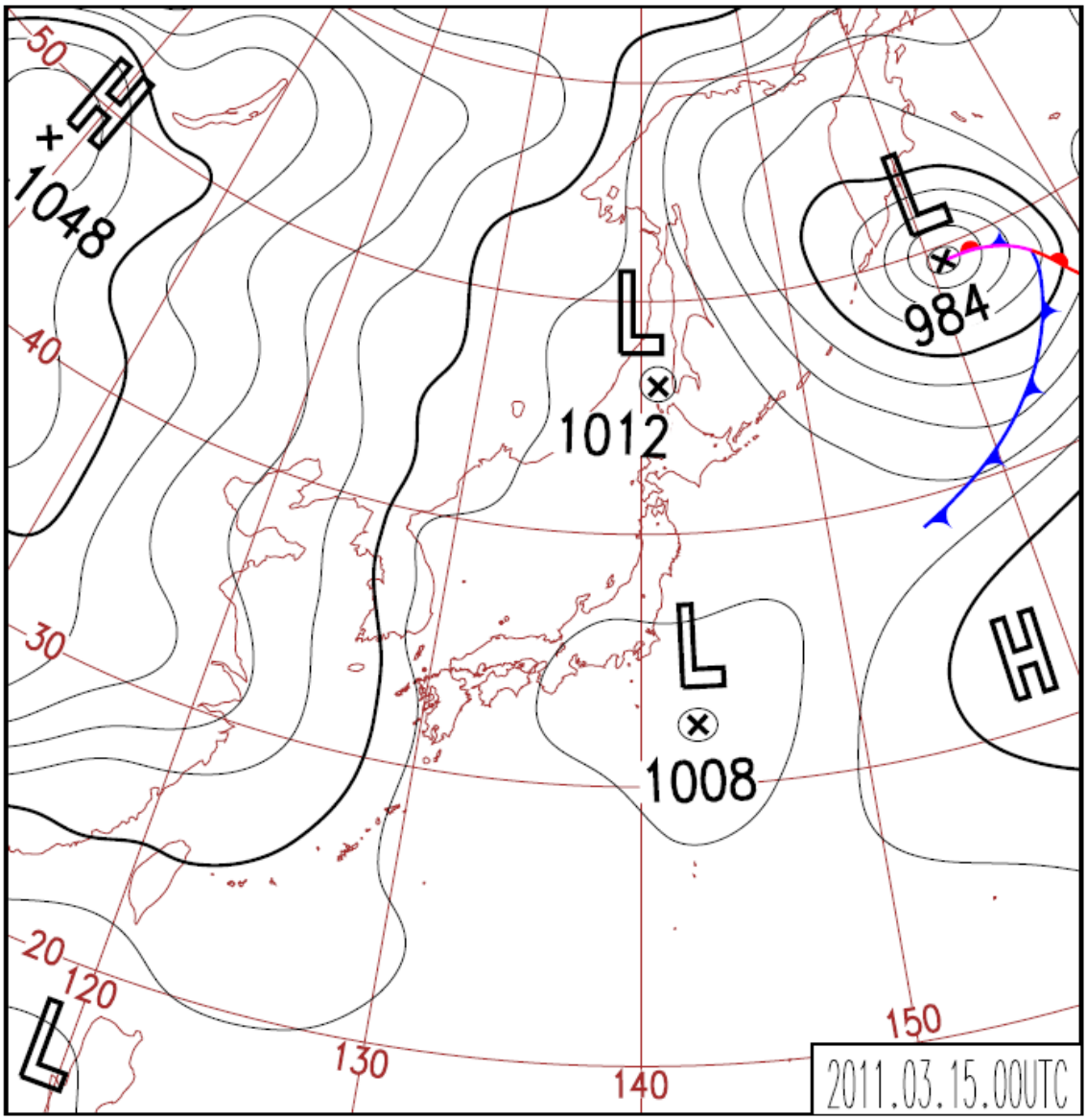

Figure 3.9 JMA surface analysis (hPa) valid 00 UTC 15 March 2011. Contour interval is 4 hPa.

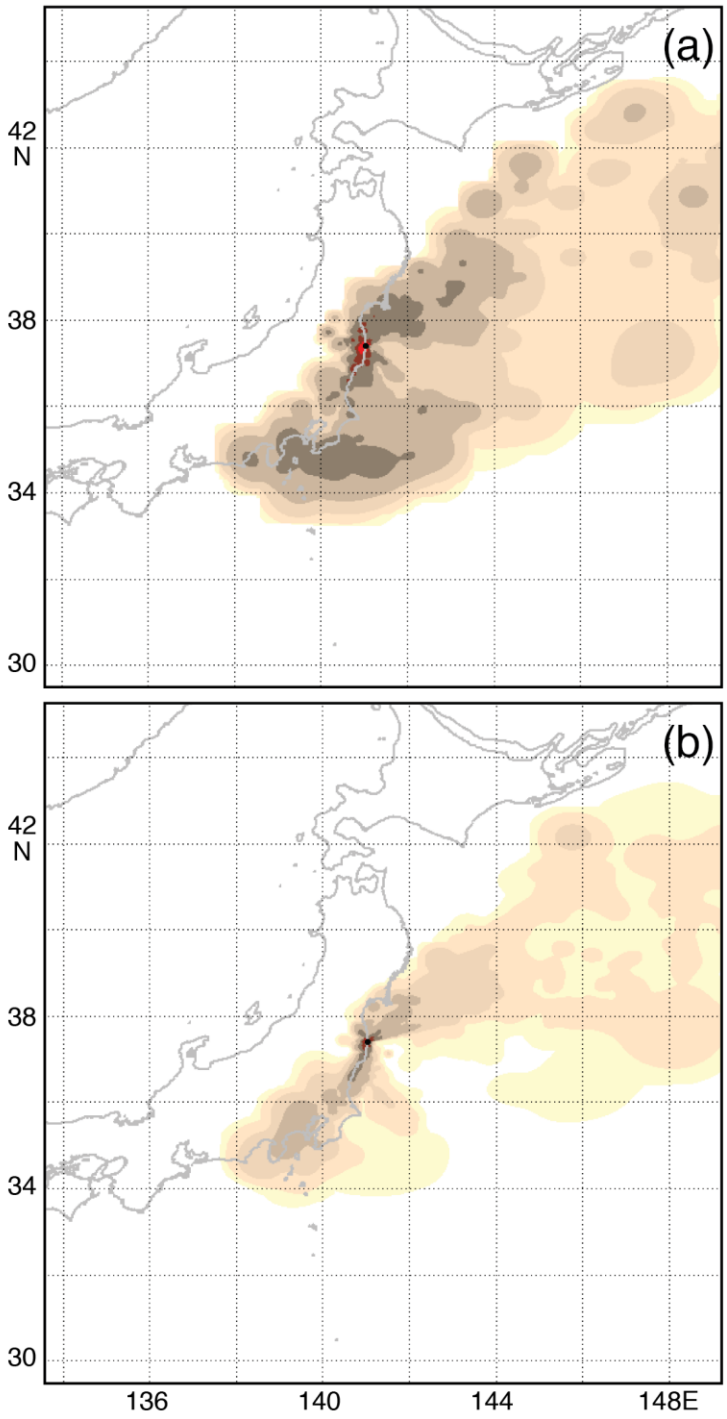

Figure 3.10 As in Figure 3.1, but for 00 UTC 16 March 2011.

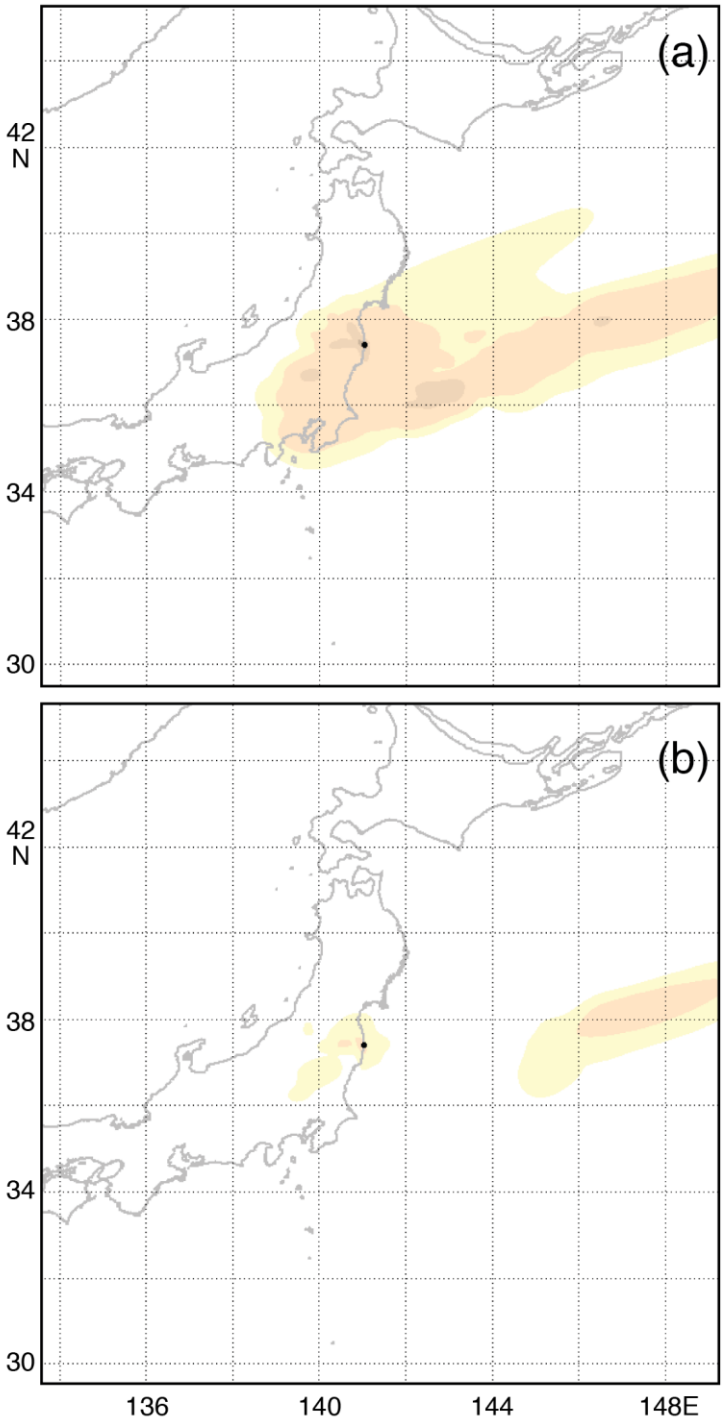

Figure 3.11 As in Figure 3.8, but for 00 UTC 16 March 2011.

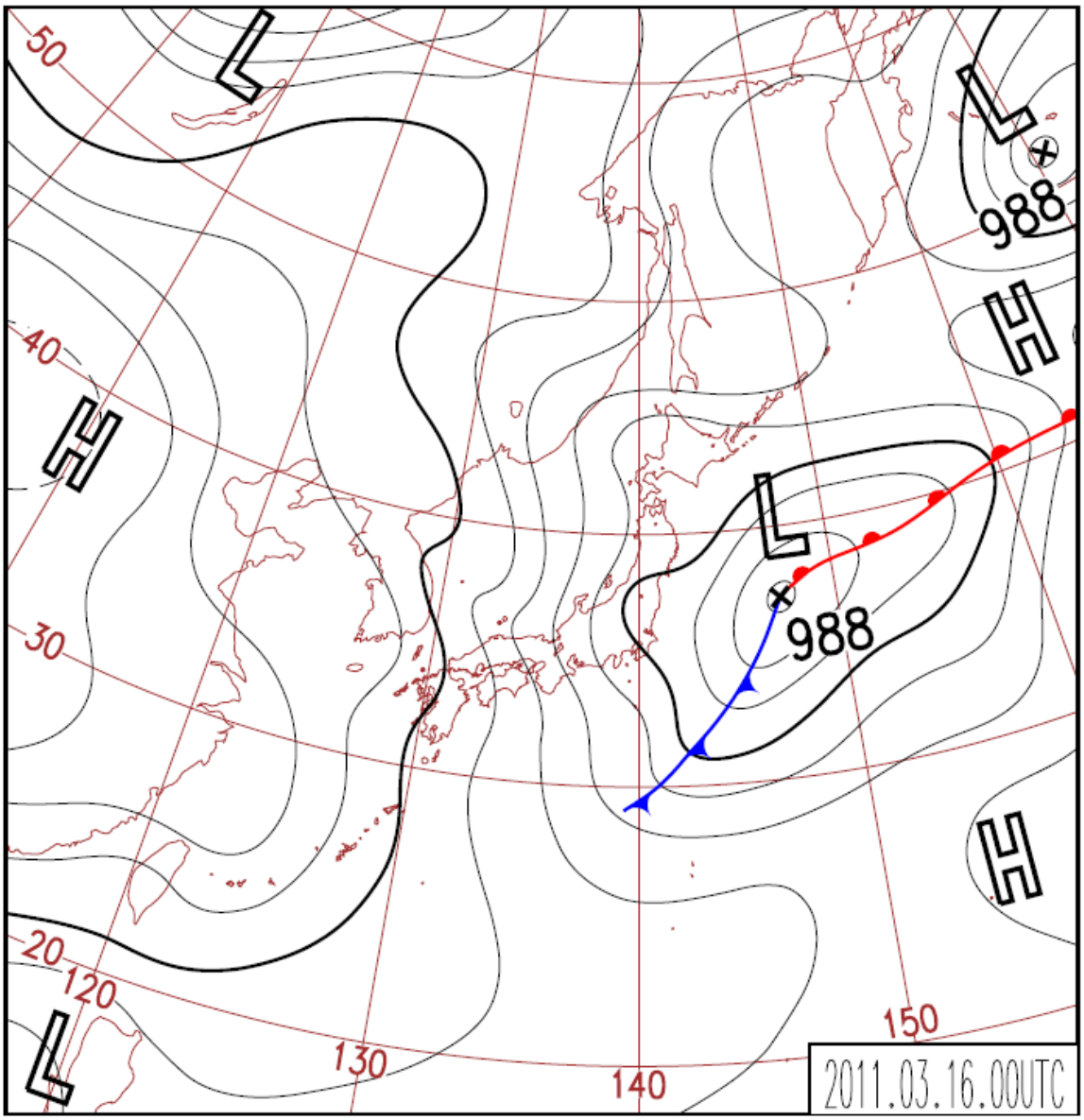

Figure 3.12 JMA surface analysis (hPa) valid 00 UTC 16 March 2011. Contour interval is 4 hPa.

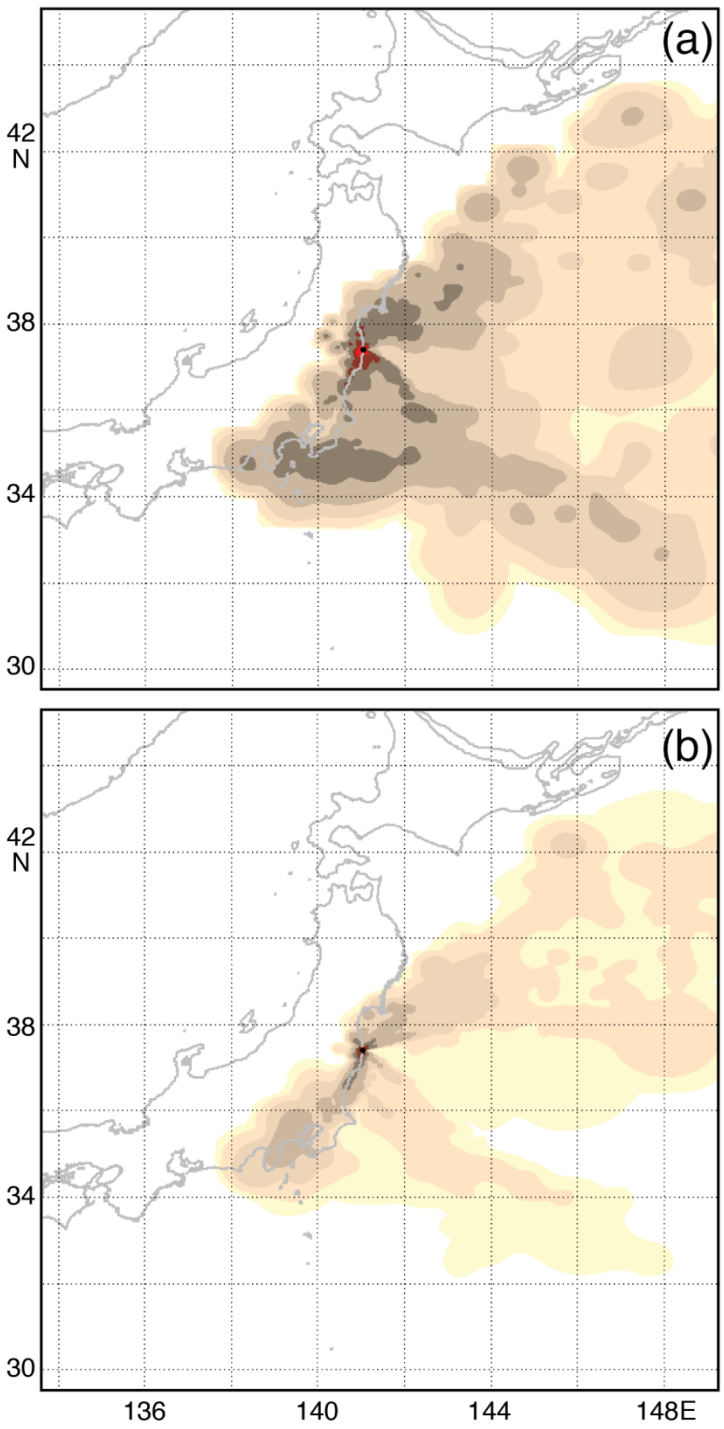

Figure 3.13 As in Figure 3.1, but for 00 UTC 17 March 2011.

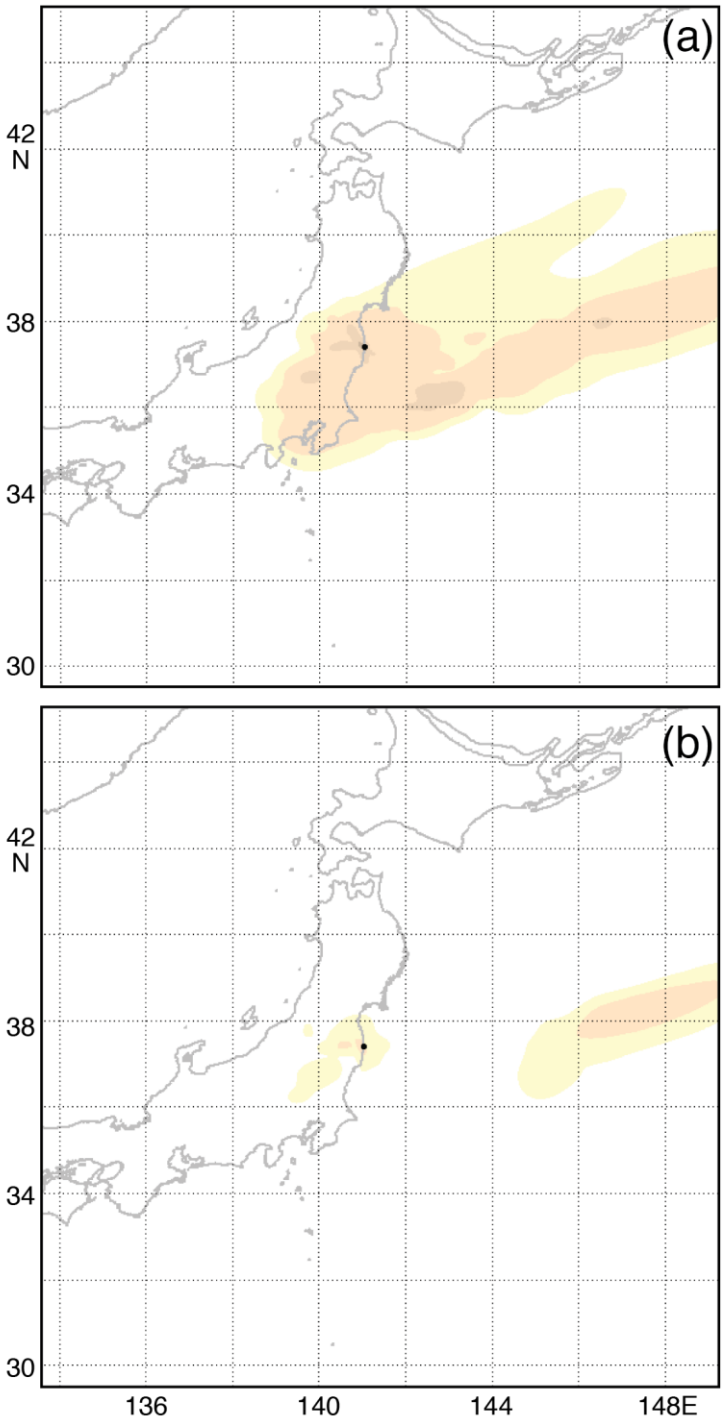

Figure 3.14 As in Figure 3.8, but for 00 UTC 17 March 2011.

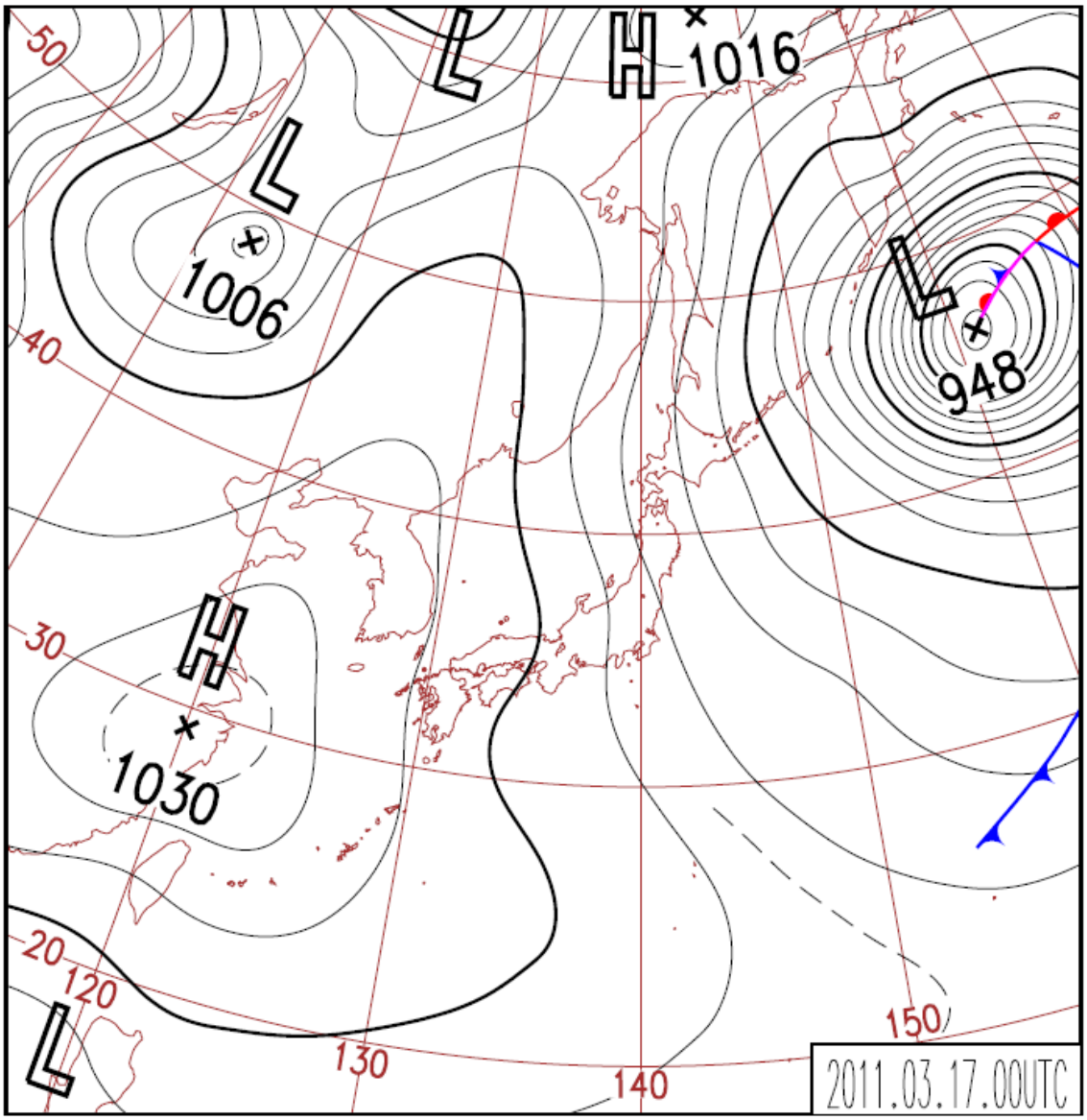

Figure 3.15 JMA surface analysis (hPa) valid 00 UTC 17 March 2011. Contour interval is 4 hPa.

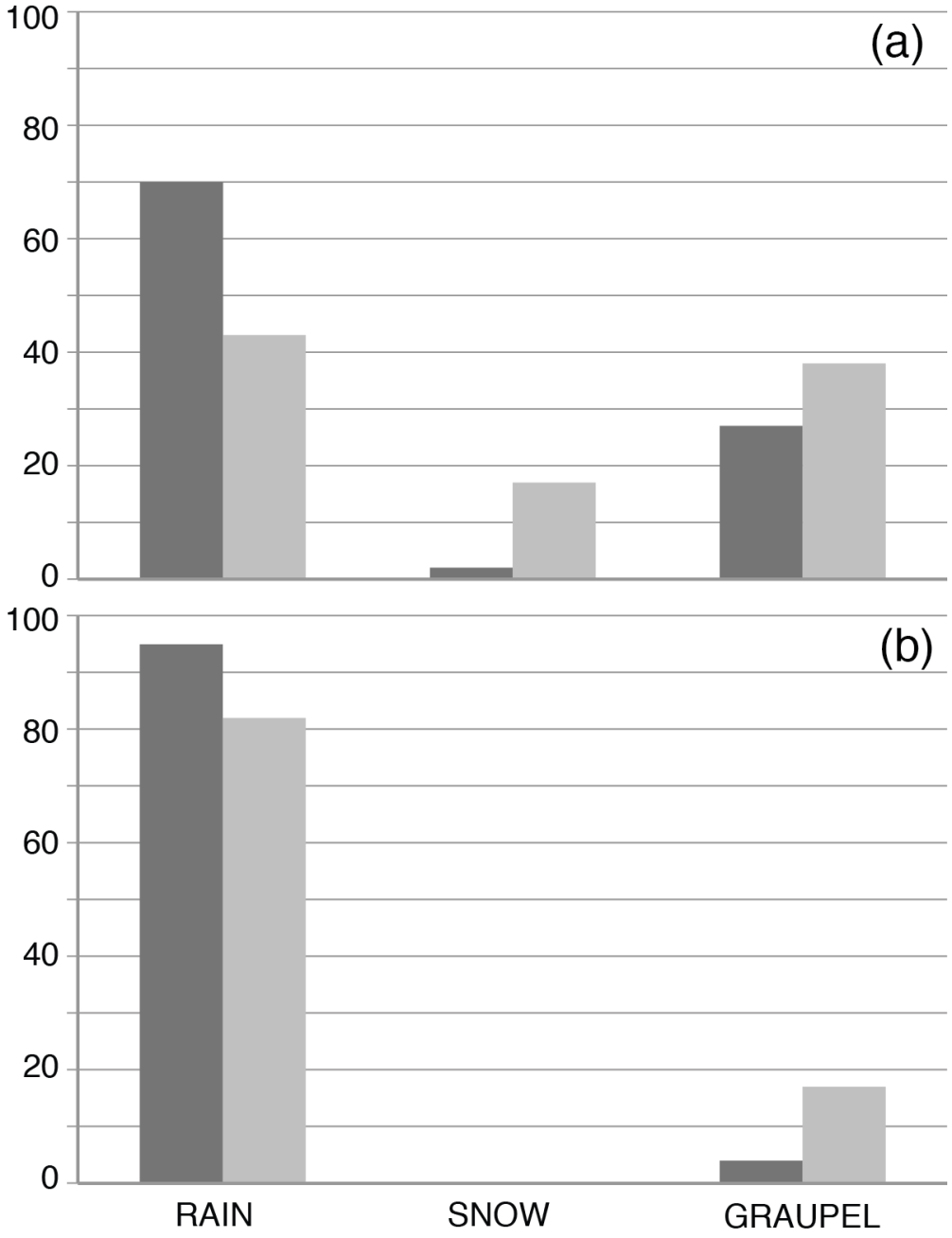

Figure 3.16 Percentage contributions of cumulative surface wet deposition at 00 UTC 17 March 2011 due to scavenging of ^{137}Cs by rain, snow, and graupel for the baseline simulation (MMD=0.5, σ_g= 1.5). Stohl source term (a) and Terada source term (b). Dark grey bars show total radioactivity (Bq). Light grey bars show total area (m^2).

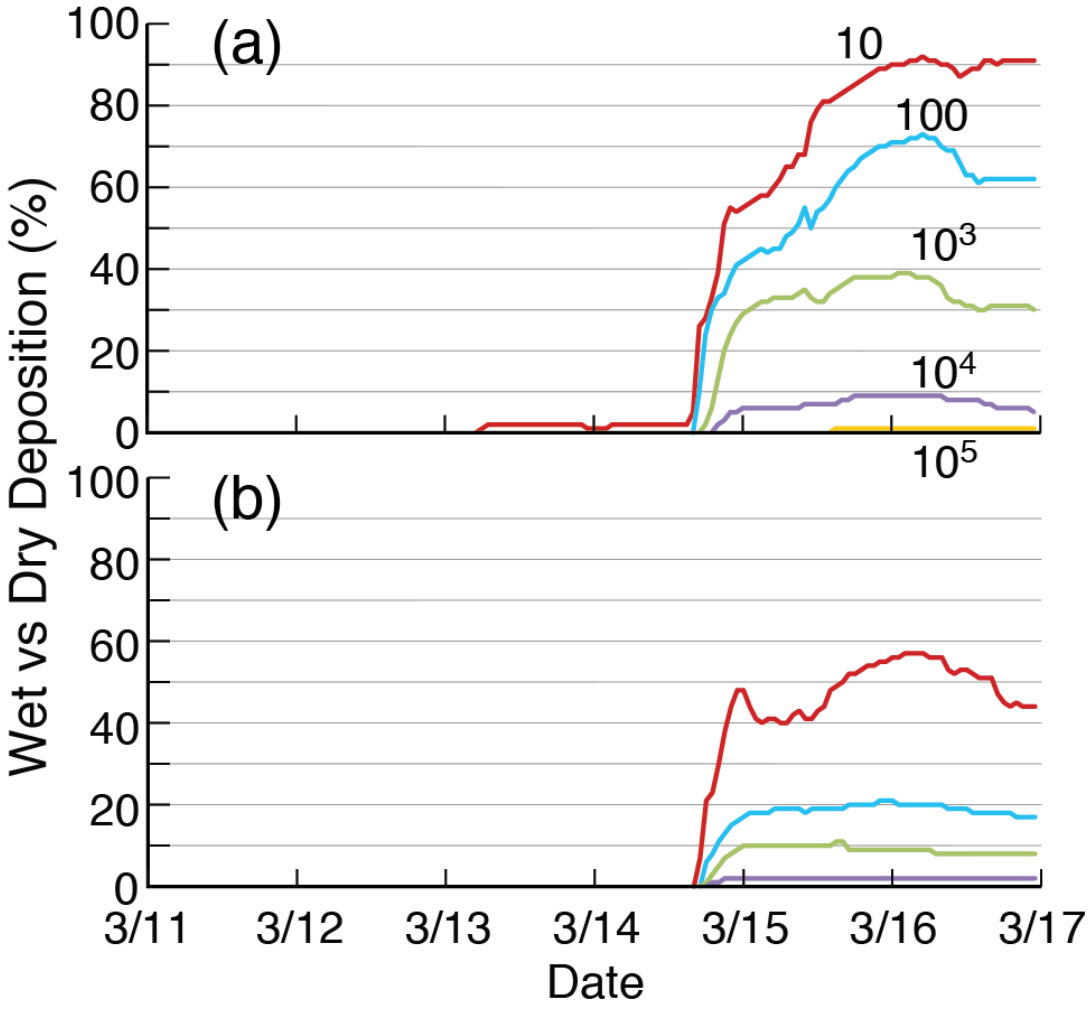

Figure 3.17 Percentage of wet vs. dry deposition with time for (a) Stohl source term and (b) Terada source term. Colored lines represent maximum cumulative surface deposition thresholds for ^{137}Cs (Bqm^{-2}): 10^1 (red), 10^2 (blue), 10^3 (green), 10^4 (purple), and 10^5 (yellow).

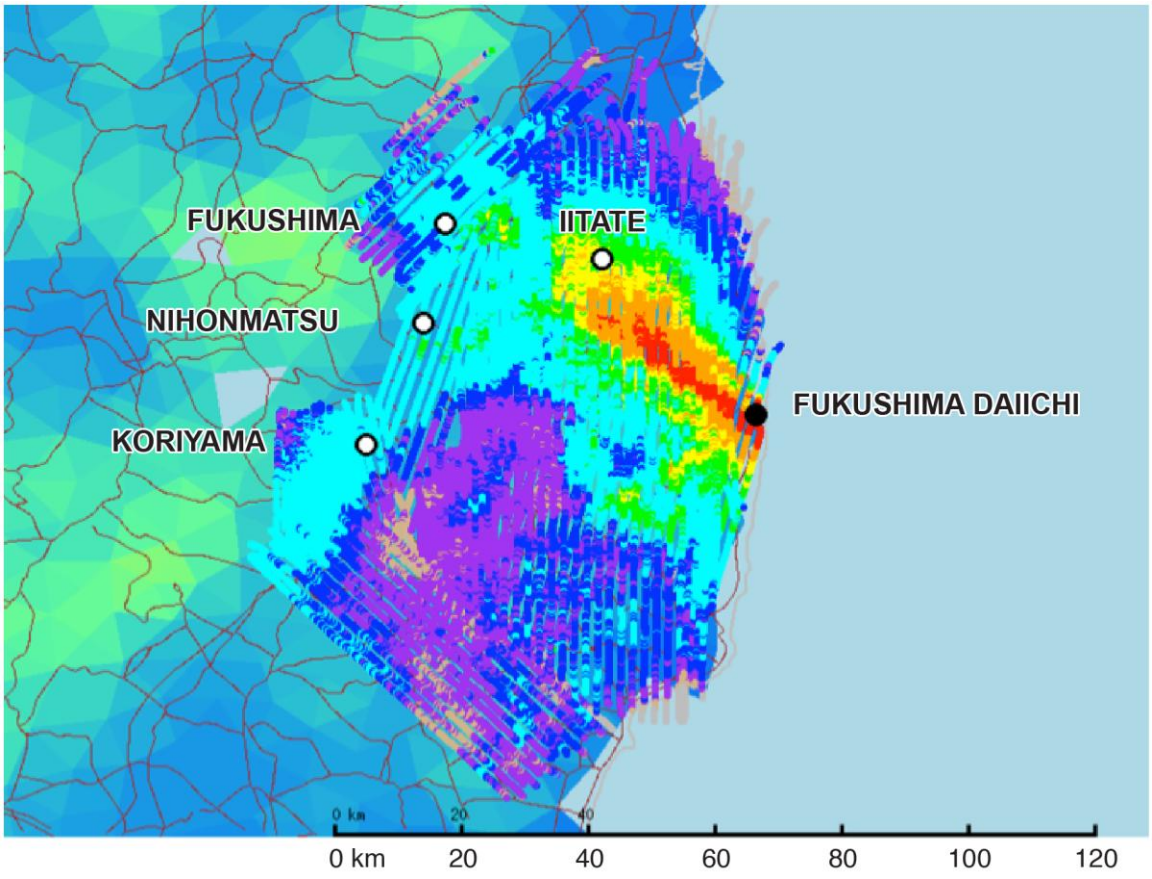

Figure 3.18 Observed surface deposition (colored circles) of ^{137}Cs (Bqm^{-2}) due to wet and dry deposition collected by DOE NNSA from fixed-wing aircraft during the period 2 April–9 May 2011. Color scale (Bqm^{-2}): <10,000 (gray), 10,000–30,000 (tan), 30,000–60,000 (purple), 60,000–100,000 (blue), 100,000–300,000 (cyan), 300,000–600,000 (green), 600,000–1,000,000 (yellow), 1,000,000–3,000,000 (orange), and >3,000,000 (red). Background field is OMEGA terrain (m) above MSL. Brown lines overlaid on terrain show major surface roads. Black circle indicates location of the Fukushima nuclear power station. Black and white circles indicate the locations of Iitate, Fukushima, Nihonmatsu, and Koriyama. Horizontal scale (km) is shown at bottom.

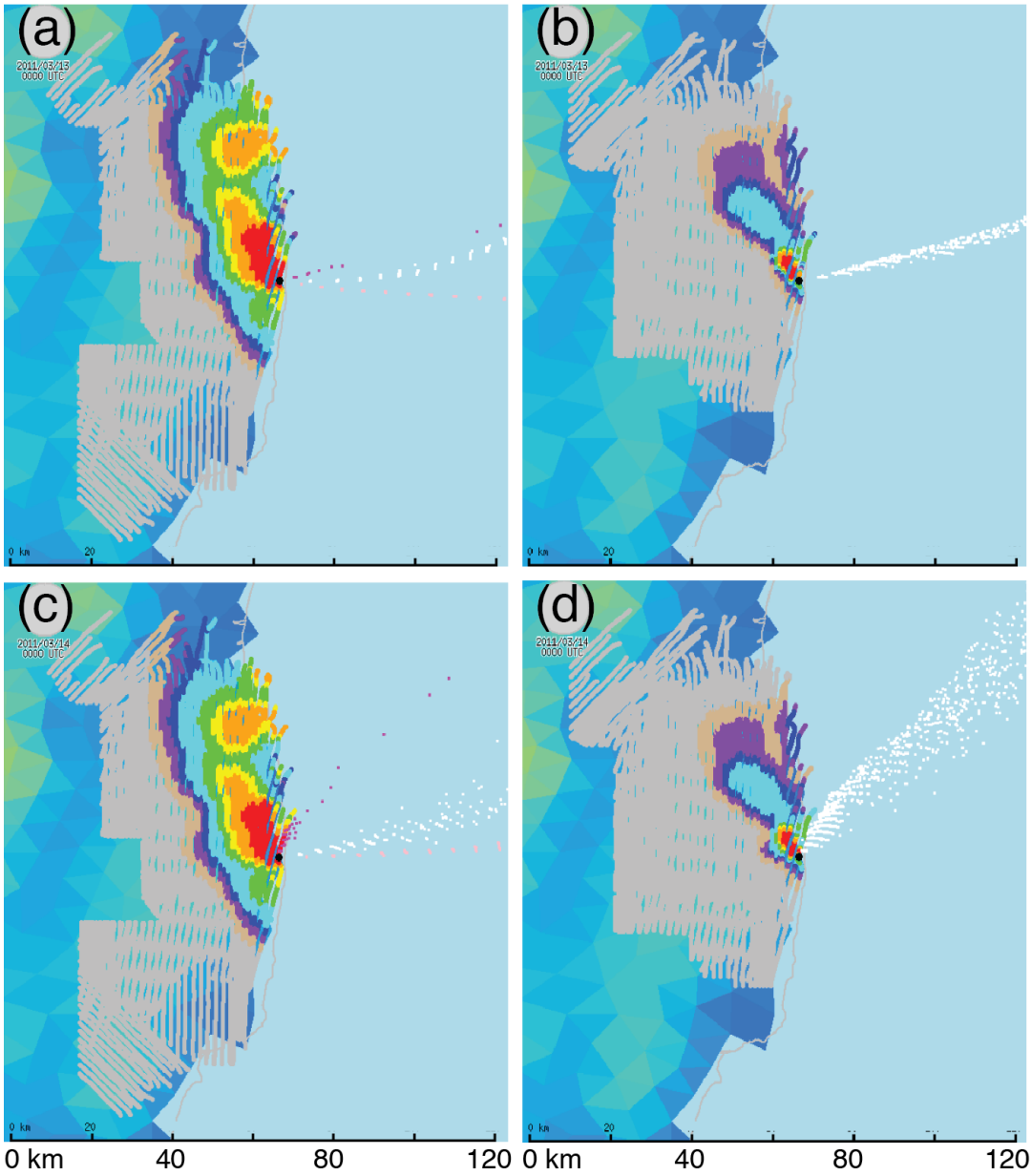

Figure 3.19 OMEGA puff centroids and cumulative total surface deposition patterns (Bqm^{-2}) for the Stohl and Terada source terms at 00 UTC 13 March 2011 (a, b, respectively) and 00 UTC 14 March 2011 (c, d, respectively). Color scale for surface deposition as in Figure 3.18. Background field is OMEGA terrain height (m) above MSL. Horizontal scale (km) is shown at bottom. Centroid colors correspond to emission height (m AGL): ≤ 50 (magenta), 100–300 (white), and 1000 (pink).

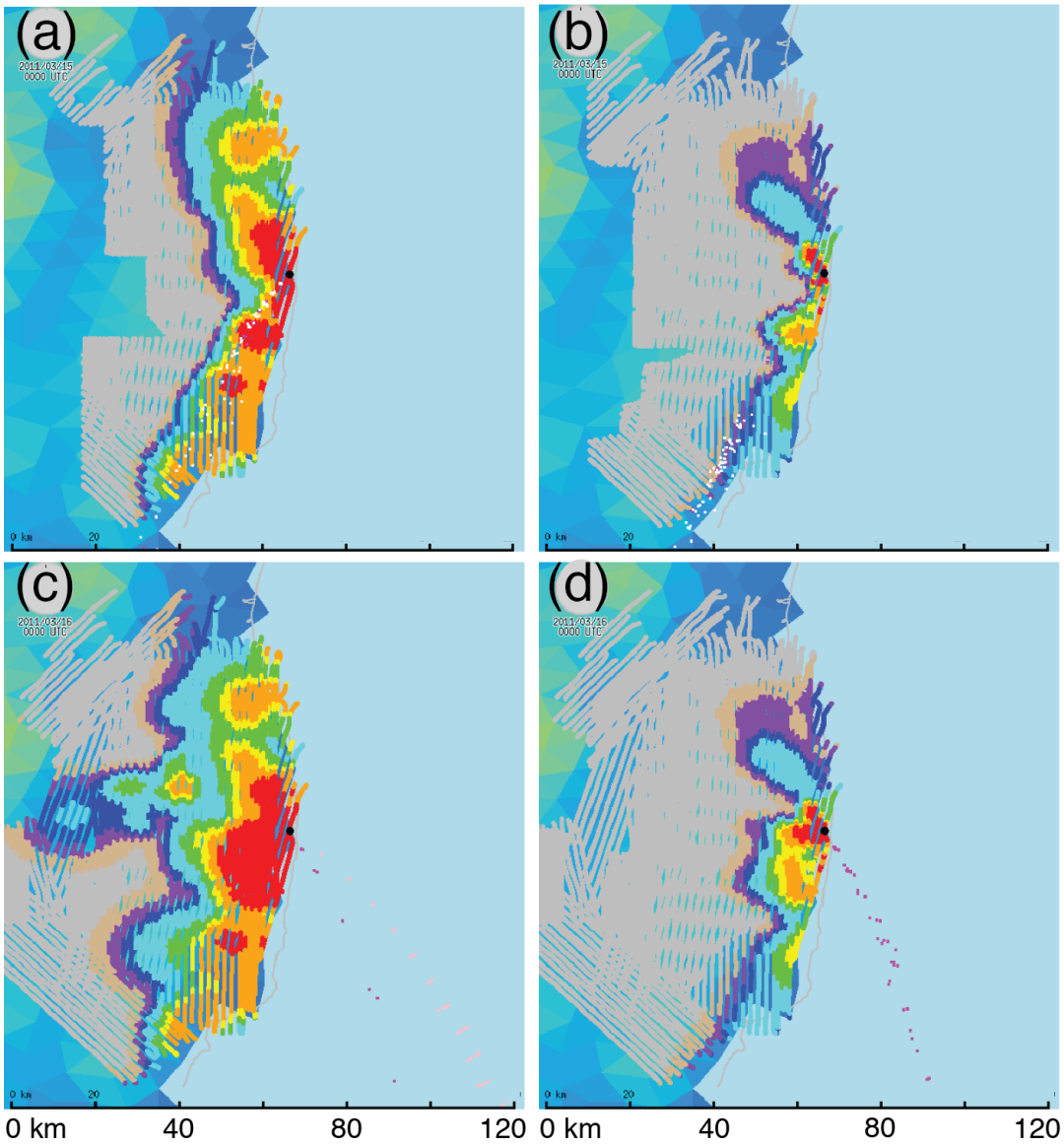

Figure 3.20 OMEGA puff centroids and cumulative total surface deposition patterns (Bqm^{-2}) for the Stohl and Terada source terms at 00 UTC 15 March 2011 (a, b, respectively) and 00 UTC 16 March 2011 (c, d, respectively). Color scale for surface deposition as in Figure 3.18. Background field is OMEGA terrain height (m) above MSL. Horizontal scale (km) is shown at bottom. Centroid colors correspond to emission height (m AGL): ≤ 50 (magenta), 100–300 (white), and 1000 (pink).

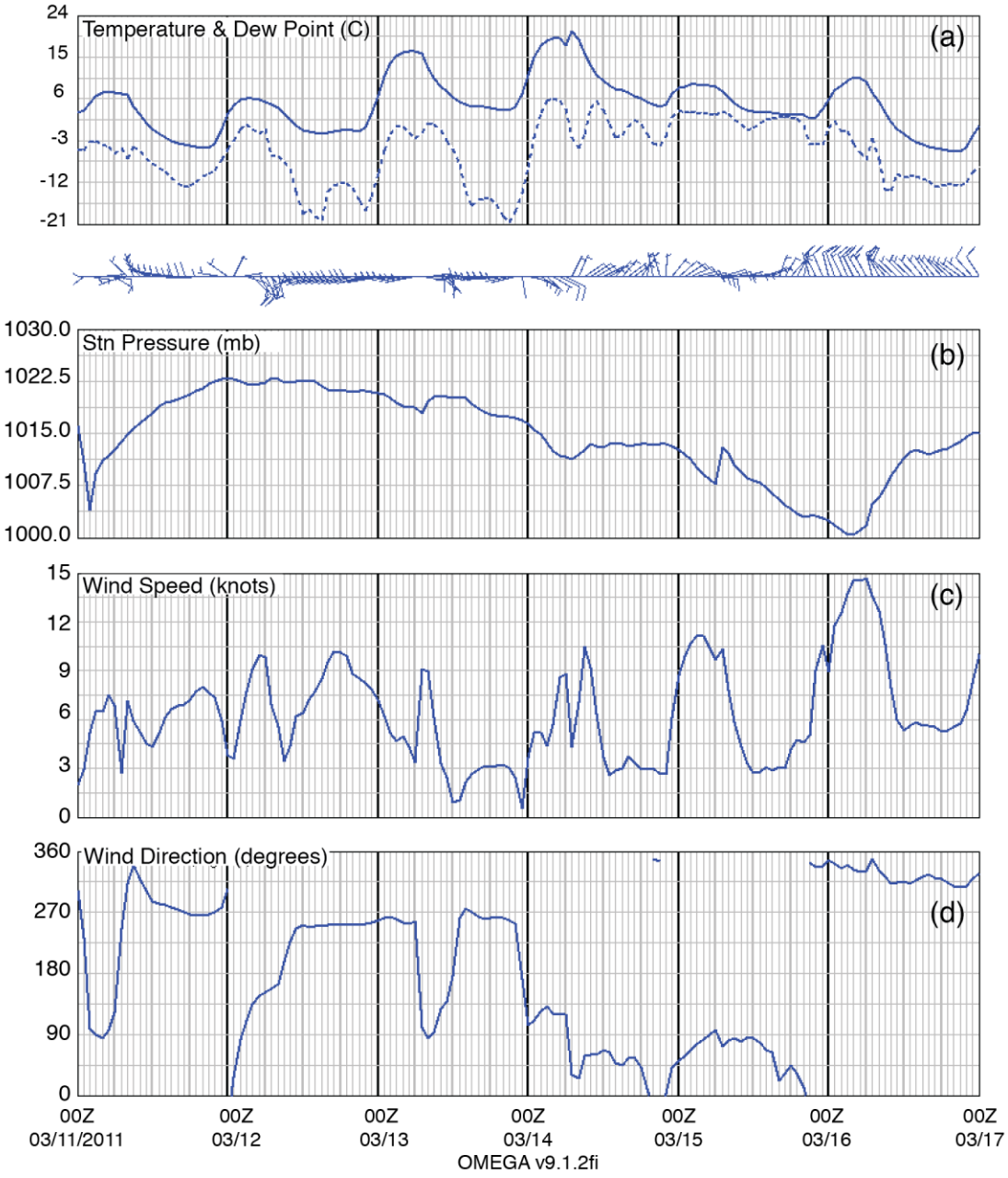

Figure 3.21 OMEGA surface meteogram (blue) at the Fukushima Daiichi nuclear power station for the period 00 UTC 11 March to 00 UTC 17 March 2011. Shown are (a) temperature and dewpoint temperature (°C), (b) station pressure (hPa), (c) wind speed (knots), and (d) wind direction (degrees).

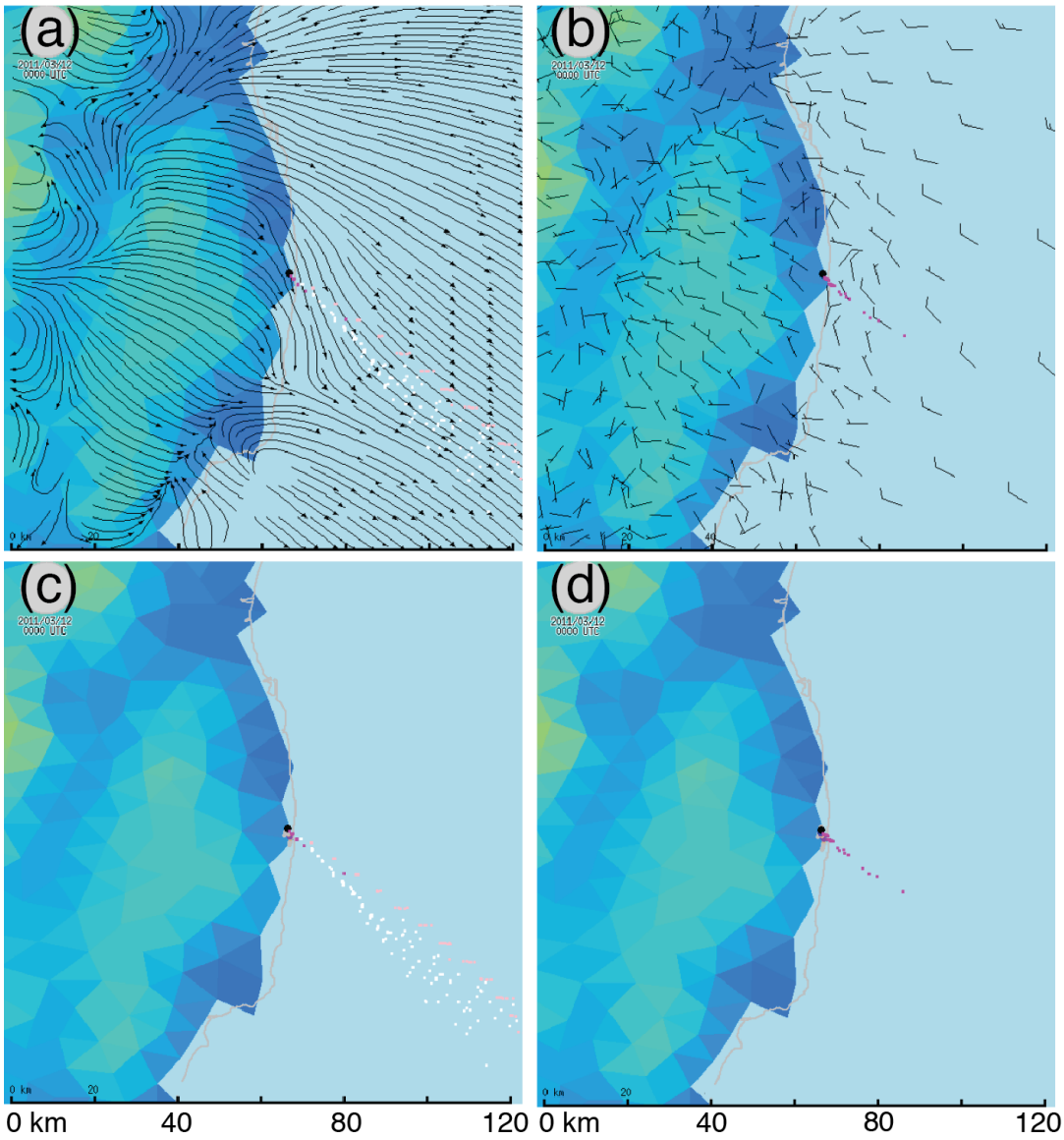

Figure 3.22 OMEGA puff centroids, surface winds (knots) and cumulative total surface deposition patterns (Bqm^{-2}) for the Stohl (a, c) and Terada (b, d) source terms at 00 UTC 12 March 2011. Color scale for surface deposition as in Figure 3.18. Background field is OMEGA terrain height (m) above MSL. Horizontal scale (km) is shown at bottom. Centroid colors correspond to emission height (m AGL): ≤ 50 (magenta), 100–300 (white), and 1000 (pink).

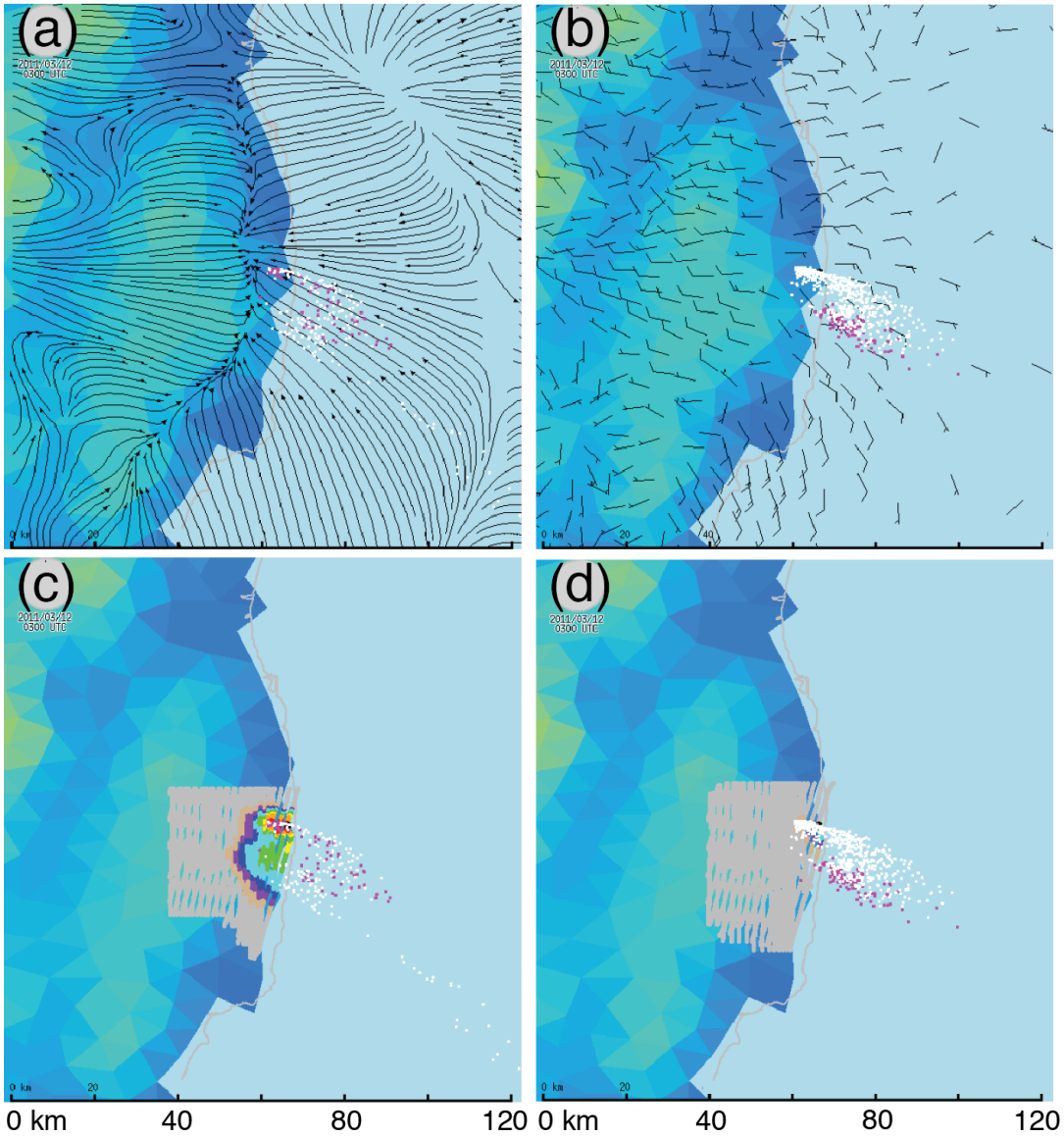

Figure 3.23 As in Figure 3.22, but for 03 UTC 12 March 2011.

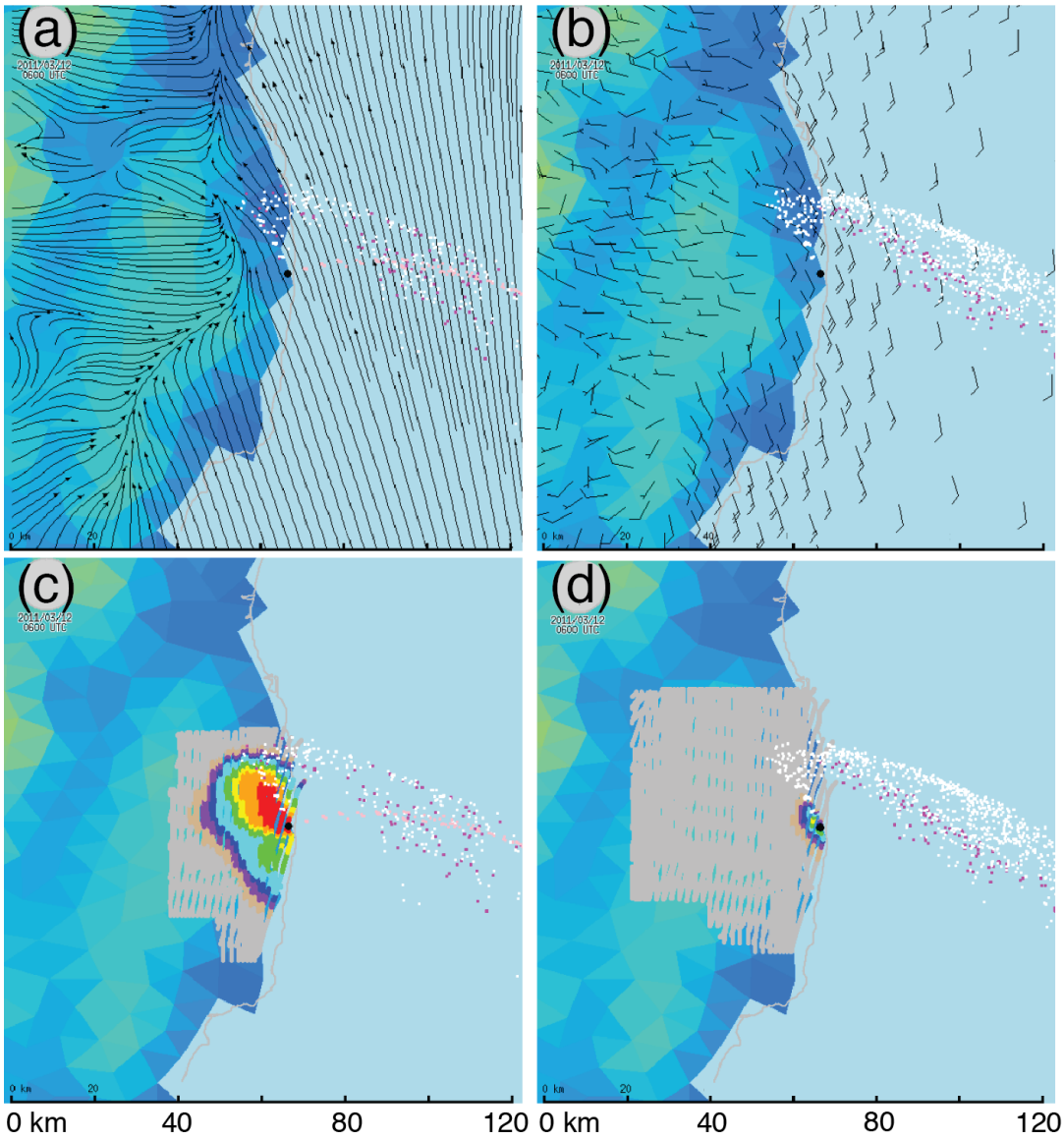

Figure 3.24 As in Figure 3.22, but for 06 UTC 12 March 2011.

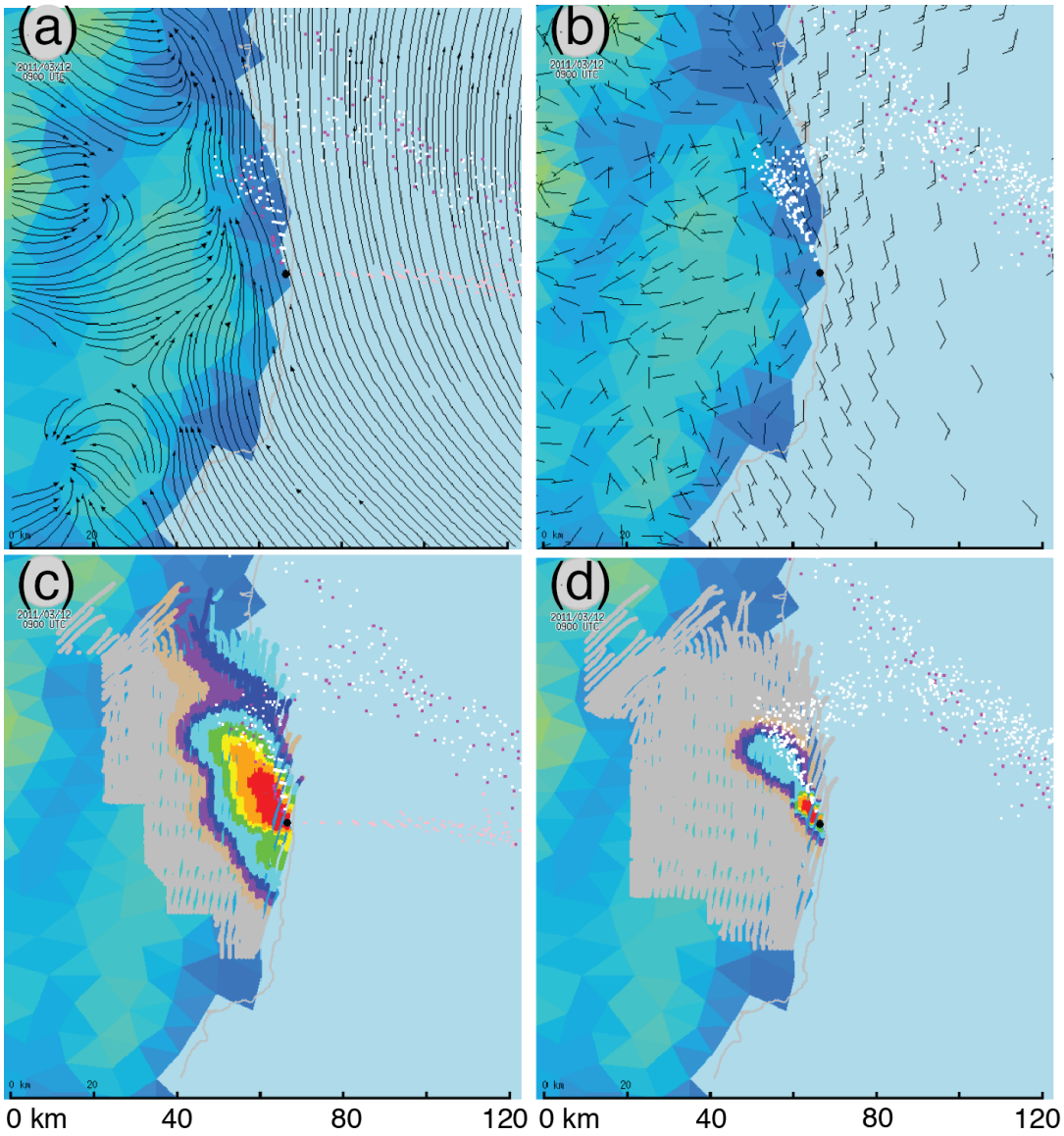

Figure 3.25 As in Figure 3.22, but for 09 UTC 12 March 2011.

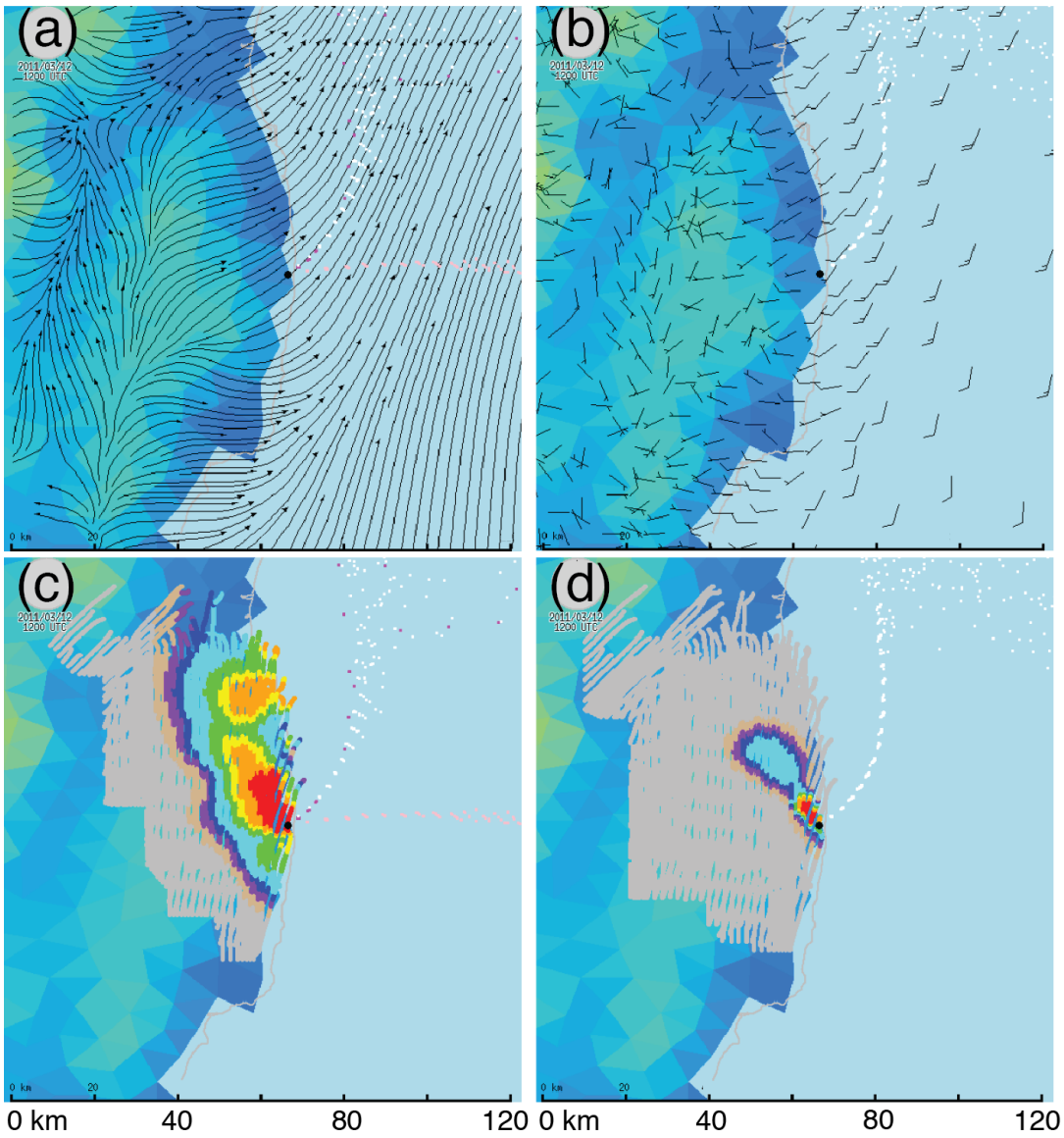

Figure 3.26 As in Figure 3.22, but for 12 UTC 12 March 2011.

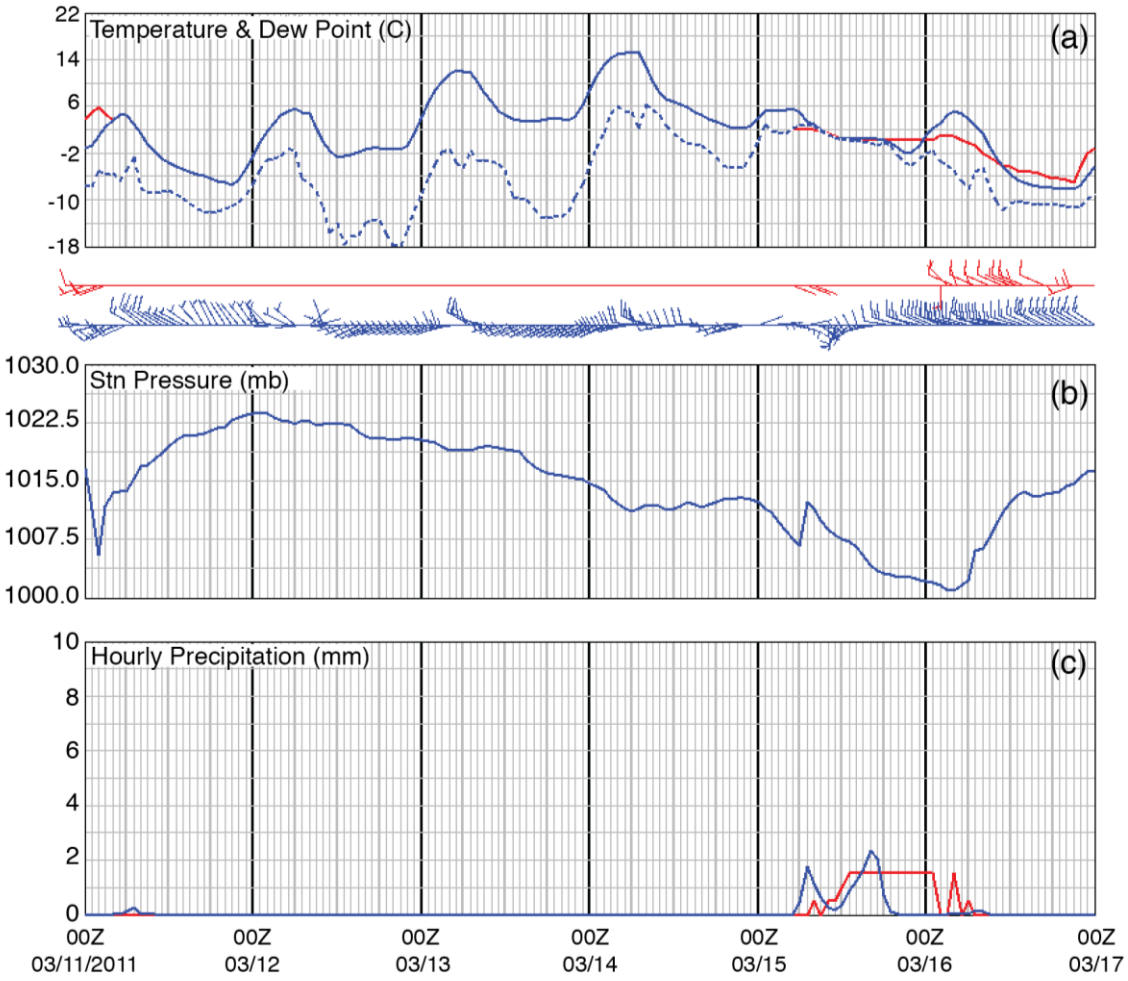

Figure 3.27 Surface meteogram for Iitate for the period 00 UTC 11 March to 00 UTC 17 March 2011. Observations (red) and OMEGA simulation (blue). Shown are (a) temperature and dewpoint temperature (°C), (b) station pressure (hPa), and (c) hourly precipitation (mm).

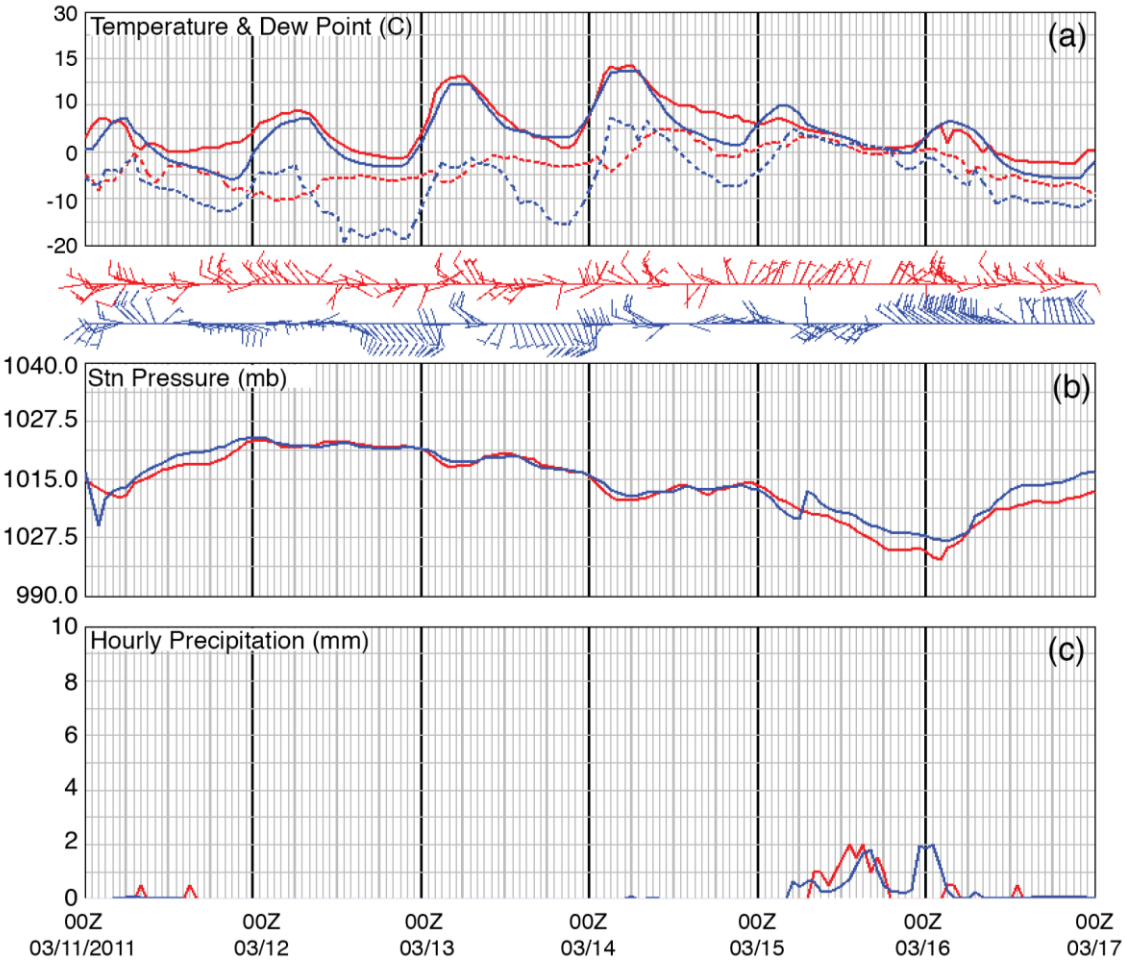

Figure 3.28 As in Figure 3.26, but for Fukushima.

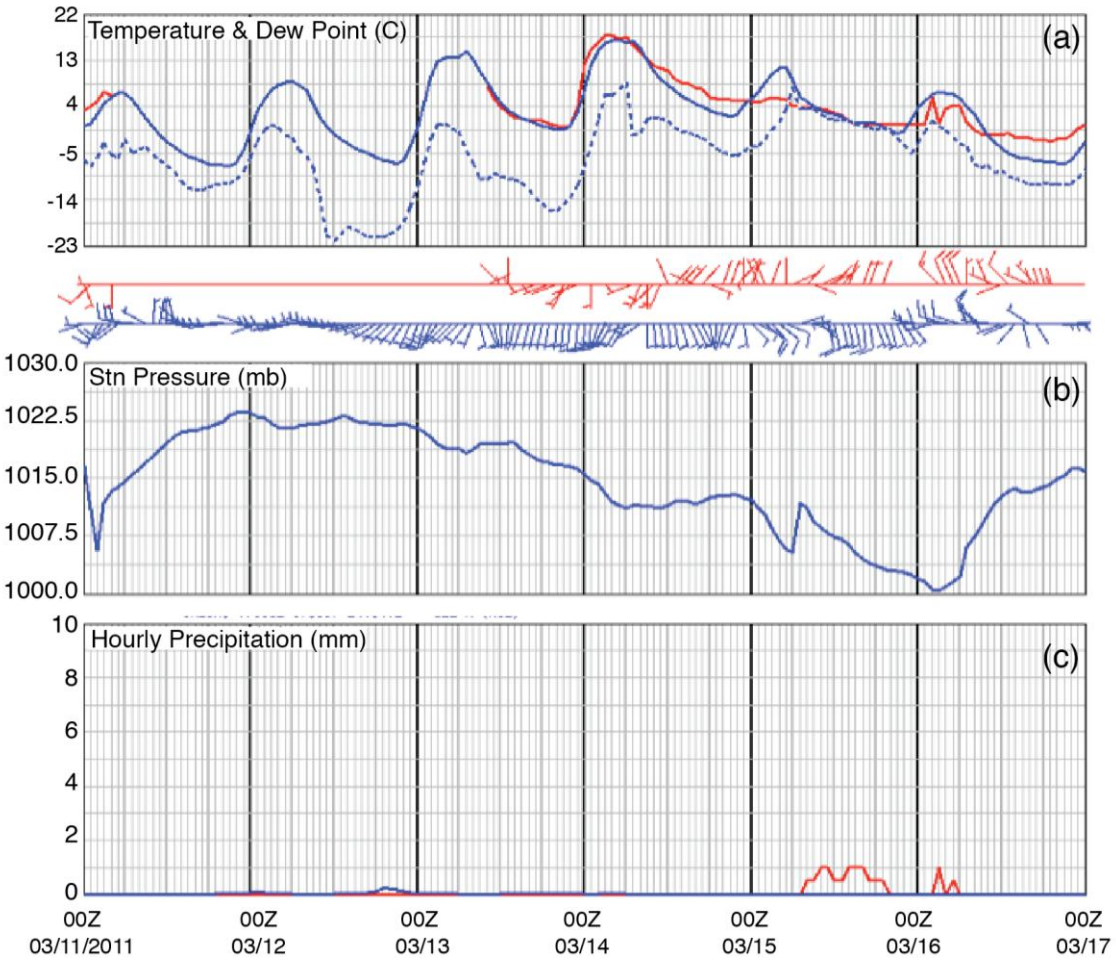

Figure 3.29 As in Figure 3.26, but for Nihonmatsu.

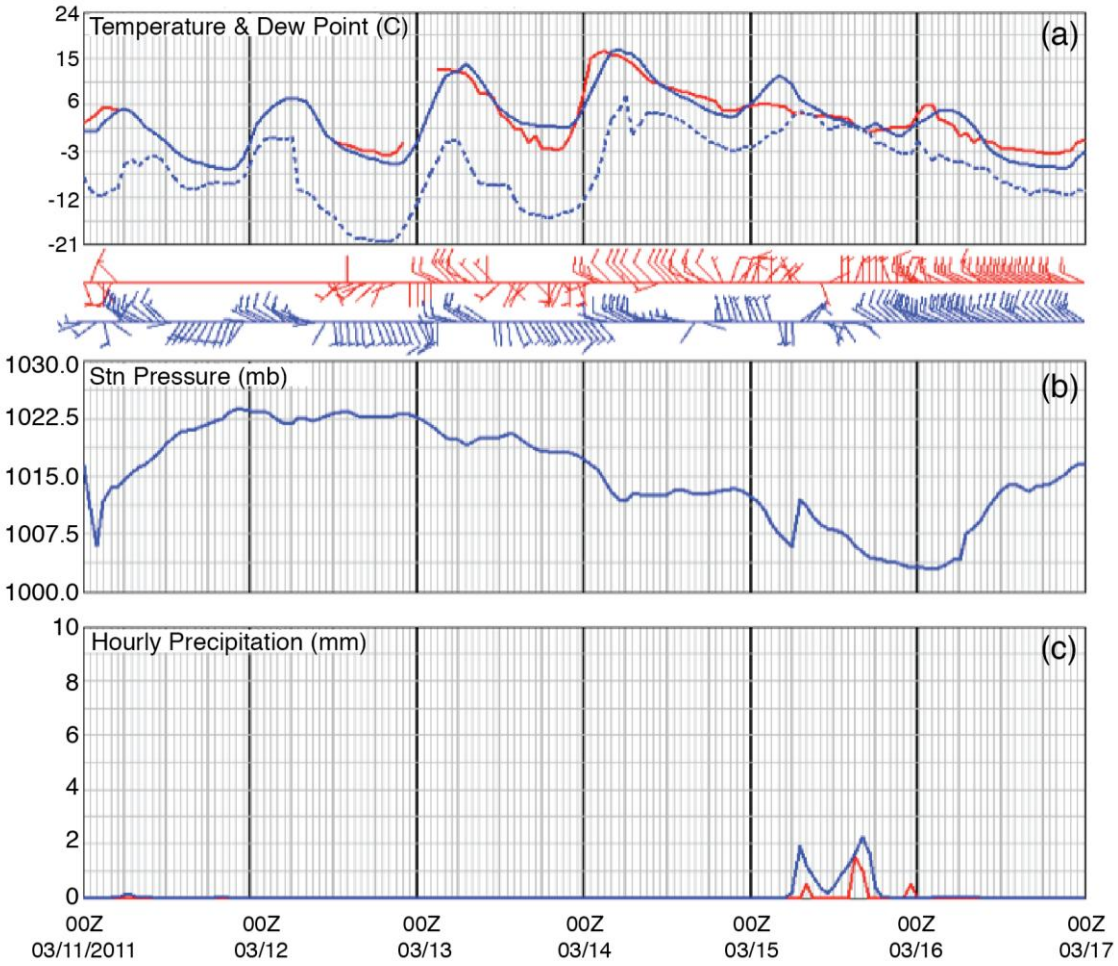

Figure 3.30 As in Figure 3.26, but for Koriyama.

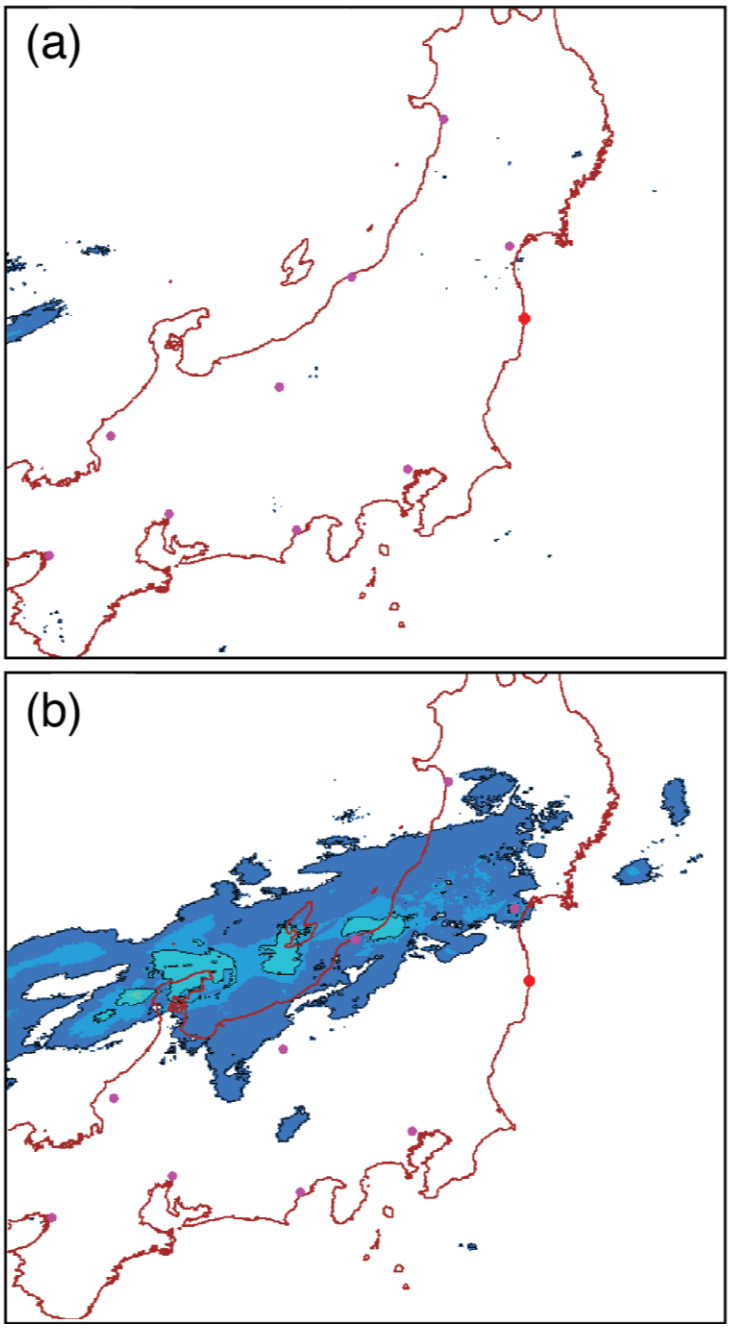

Figure 3.31 JMA radar composite surface rainfall distribution at (a) 00 UTC 15 March 2011 and (b) 06 UTC 15 March 2011. Contour intervals (mm) are: 1–3, 3–5, 5–10, 10–15, 15–20, 20–25, 25–50, 50–75, and 75–100. Red circle is the location of the Fukushima Daiichi nuclear power station. Magenta circles show locations of radar sites that comprise the composite.

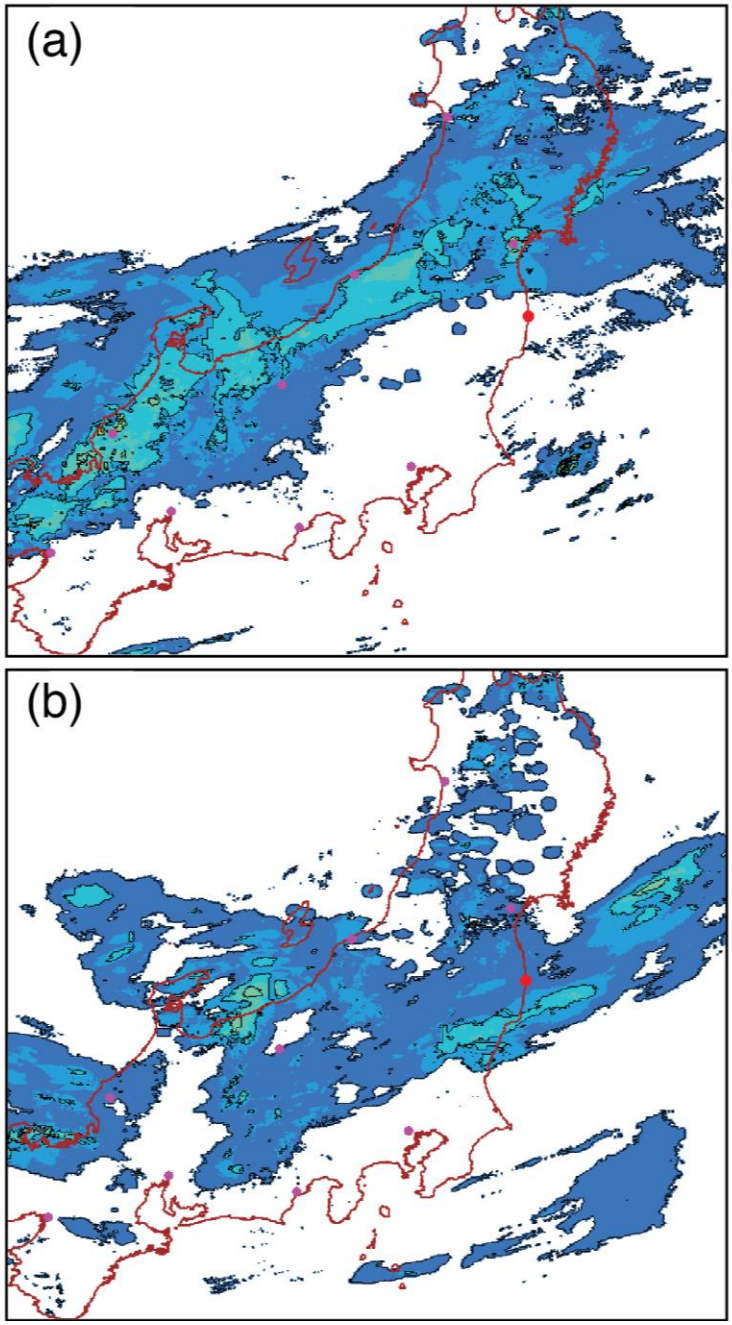

Figure 3.32 JMA radar composite surface rainfall distribution at (a) 12 UTC 15 March 2011 and (b) 18 UTC 15 March 2011. Contour intervals (mm) are: 1–3, 3–5, 5–10, 10–15, 15–20, 20–25, 25–50, 50–75, and 75–100. Red circle is the location of the Fukushima Daiichi nuclear power station. Magenta circles show locations of radar sites that comprise the composite.

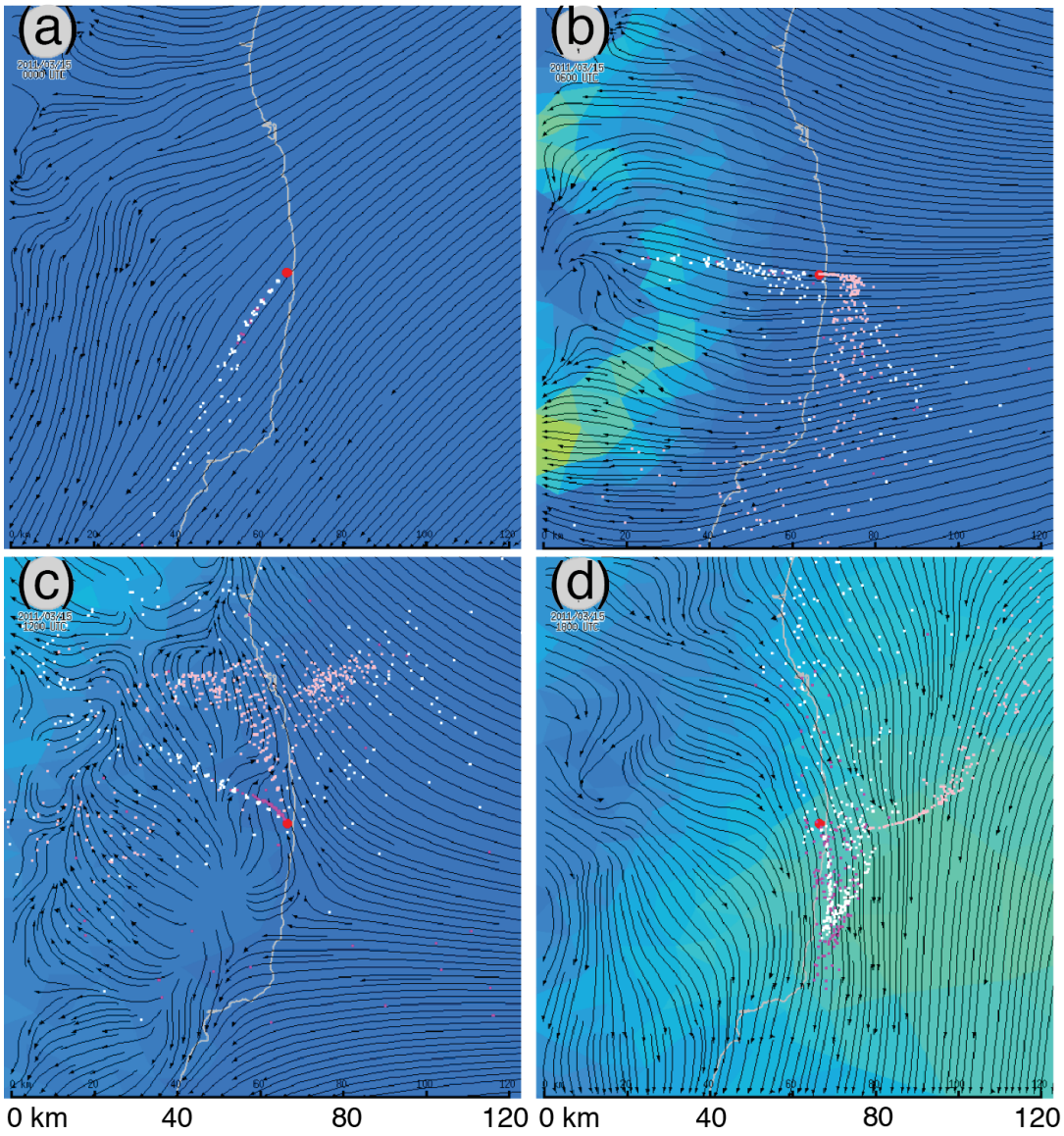

Figure 3.33 OMEGA puff centroids and surface winds (knots) for 15 March 2011 at (a) 00 UTC, (b) 06 UTC, (c) 12 UTC, and (d) 18 UTC for the Stohl source term. Background field is OMEGA surface precipitation (mm). Horizontal scale (km) is shown at bottom. Centroid colors correspond to emission height (m AGL): ≤ 50 (magenta), 100–300 (white), and 1000 (pink).

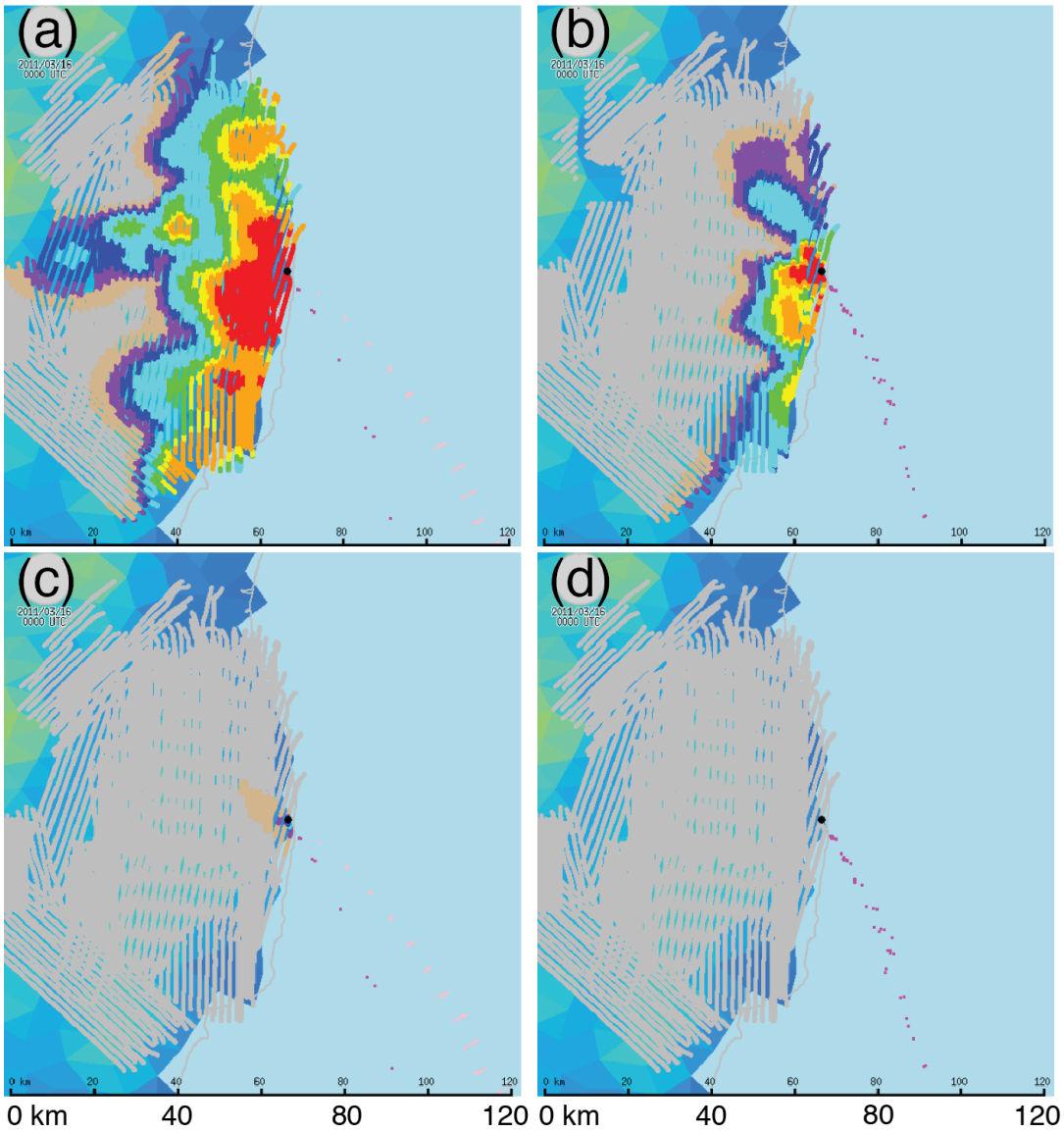

Figure 3.34 OMEGA puff centroids and cumulative total surface deposition patterns (Bqm^{-2}) for the Stohl and Terada source terms at 00 UTC 16 March 2011 (a, b, respectively) and 00 UTC 16 March 2011 (c, d, respectively). Dry deposition is shown in (a) and (b). Wet deposition is shown in (c) and (d). Color scale for surface deposition as in Figure 3.18. Background field is OMEGA terrain height (m) above MSL. Horizontal scale (km) is shown at bottom. Centroid colors correspond to emission height (m AGL): $\leq$ 50 (magenta), 100–300 (white), and 1000 (pink).

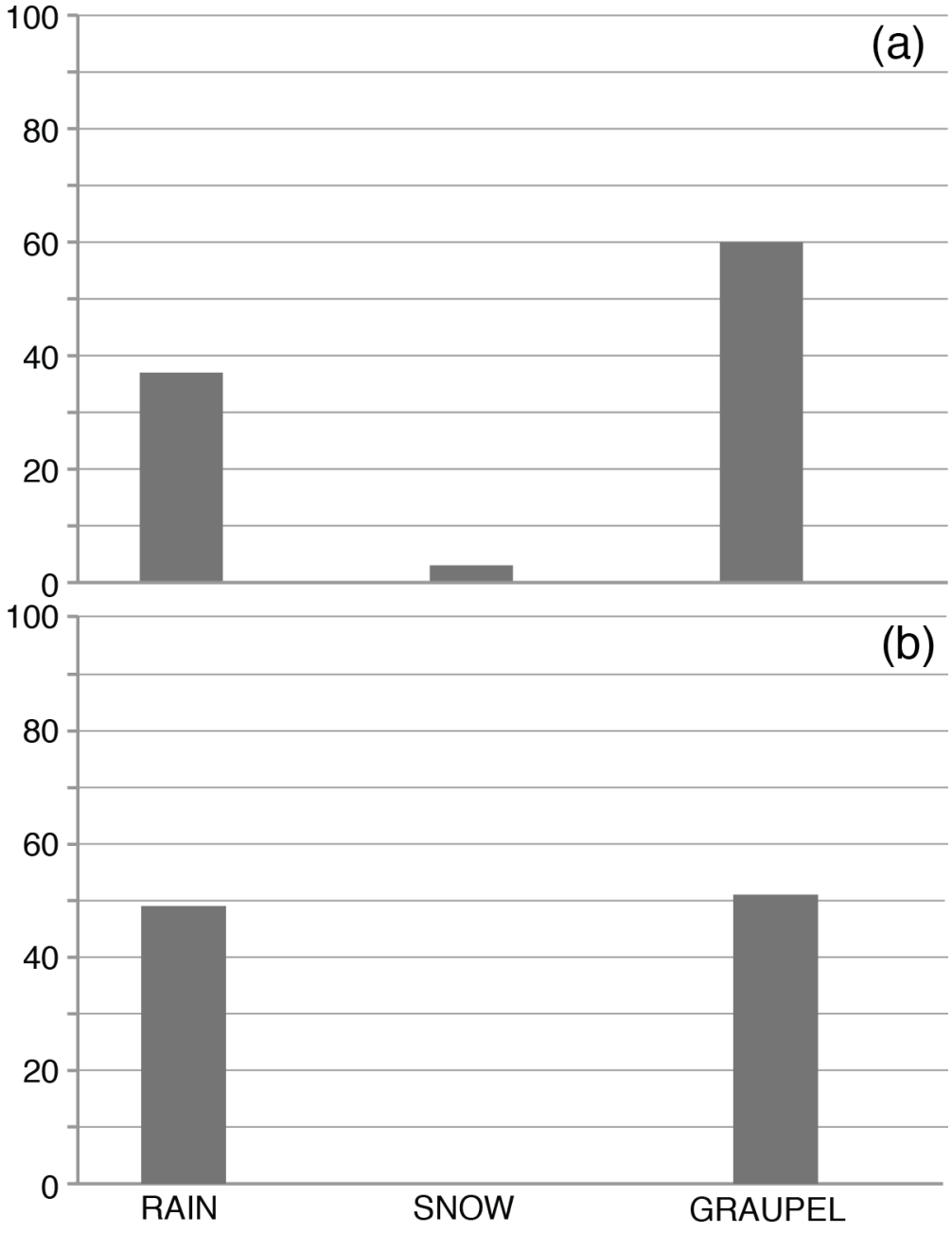

Figure 3.35 Percentage contributions of cumulative surface wet deposition (Bqm^{-2}) at 00 UTC 16 March 2011 on the NNSA aircraft grid due to scavenging of ^{137}Cs by rain, snow, and graupel for the baseline simulation (MMD=0.5, σ_g= 1.5). Stohl source term (a) and Terada source term (b).

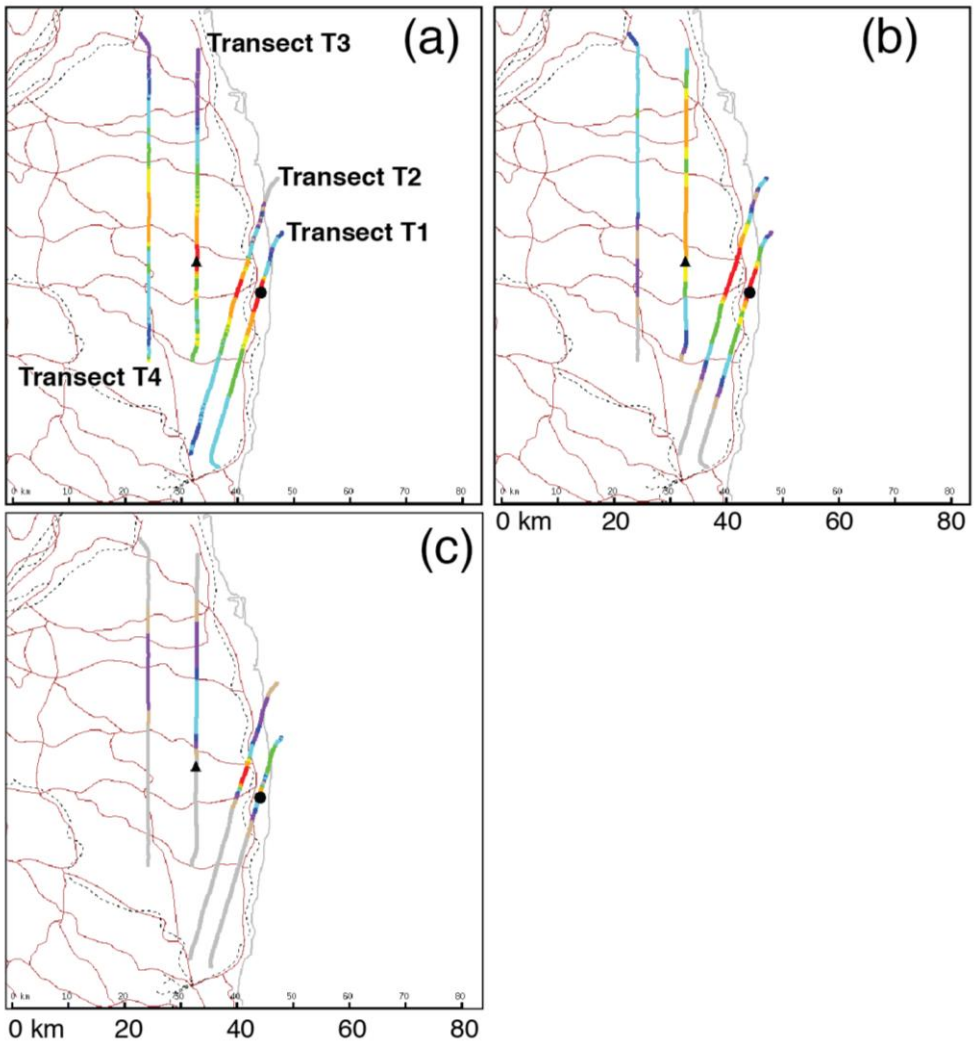

Figure 3.36 Observed and simulated surface deposition of ^{137}Cs (Bqm^{-2}) along four NNSA aircraft transects. Transects due to wet and dry deposition collected by DOE NNSA from fixed-wing aircraft during the period 2 April–9 May 2011 (a). Location of observed maximum deposition value (12617000 Bqm^{-2} at 37.485°N, 140.893°E) indicated on transect T3 by a black triangle. OMEGA cumulative surface dry deposition for the period 00 UTC 11–13 March for Stohl source term (b) and Terada source term (c). Color scale for surface deposition as in Figure 3.18. Brown lines show major surface roads. Dashed black lines show railways. Black circle indicates location of the Fukushima nuclear power station. Horizontal scale (km) is shown at bottom.

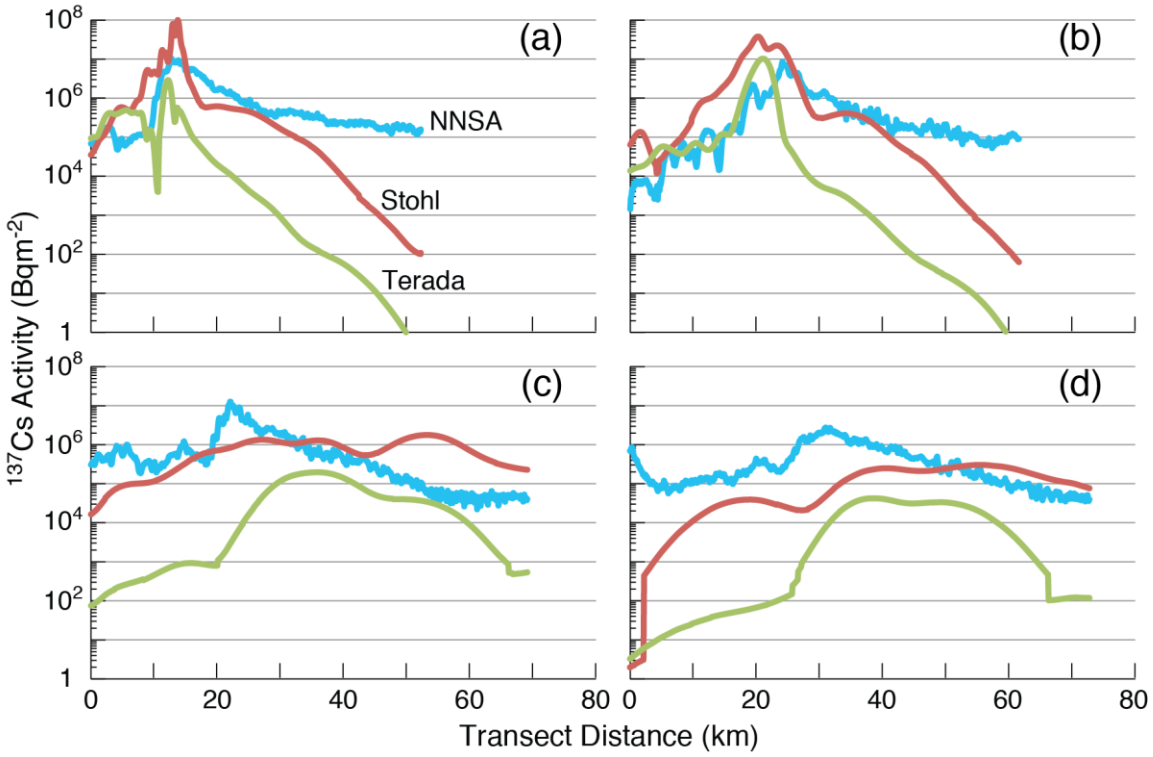

Figure 3.37 Observed and simulated radioactivity (Bqm^{-2}) due to ^{137}Cs surface deposition for the period 00 UTC 11–13 March along aircraft transects shown in Figure 3.36. Plots show (a) Transect T1, (b) Transect T2, (c) Transect T3, and (d) Transect T4. Blue line indicates NNSA observed values. Red and green lines indicate OMEGA simulated values for Stohl and Terada source terms, respectively. Transect distance (km) relates the distance from the starting point of each transect.

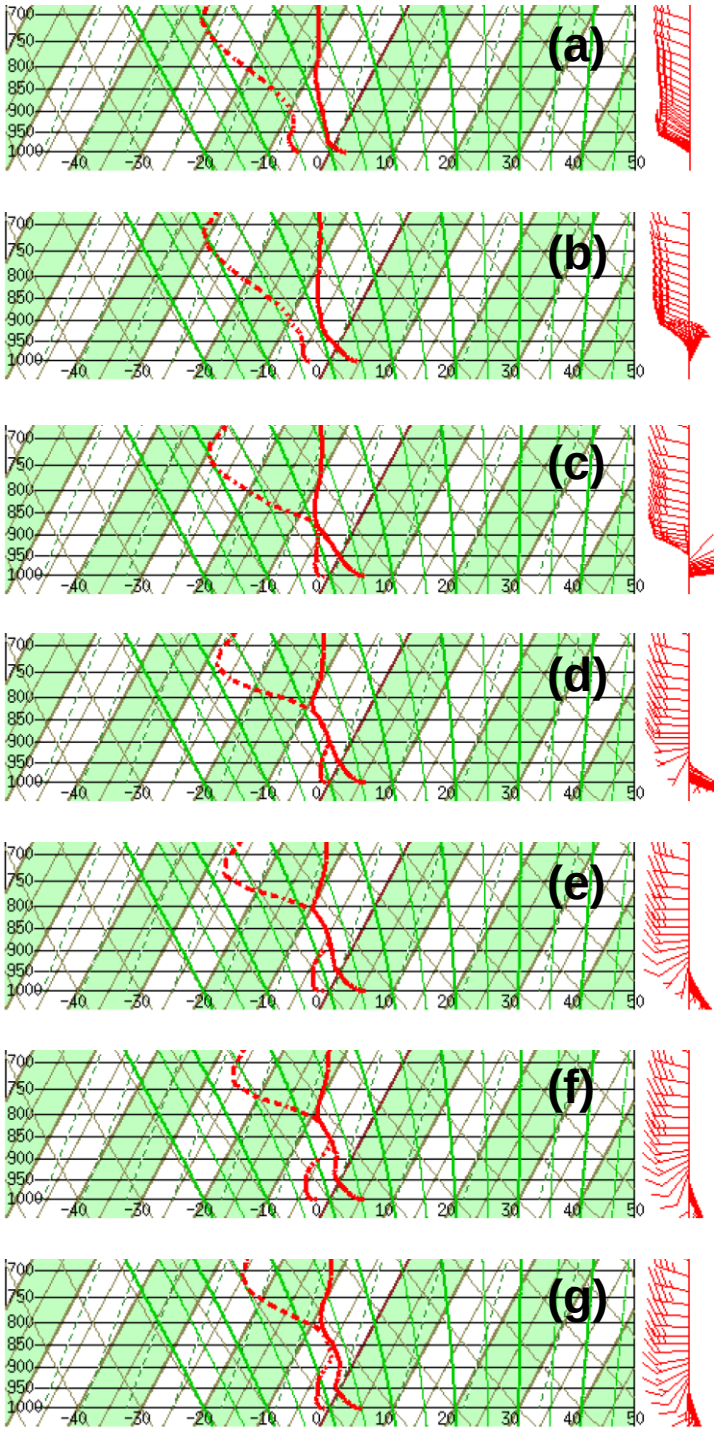

Figure 3.38 Hourly (SkewT-logP diagrams of temperature, dewpoint temperature (°C), and winds (knots) in the lowest 3 km over the accident site on 12 March. Shown are (a) 00, (b) 01, (c) 02, (d) 03, (e) 04, (f) 05, and (g) 06 UTC.

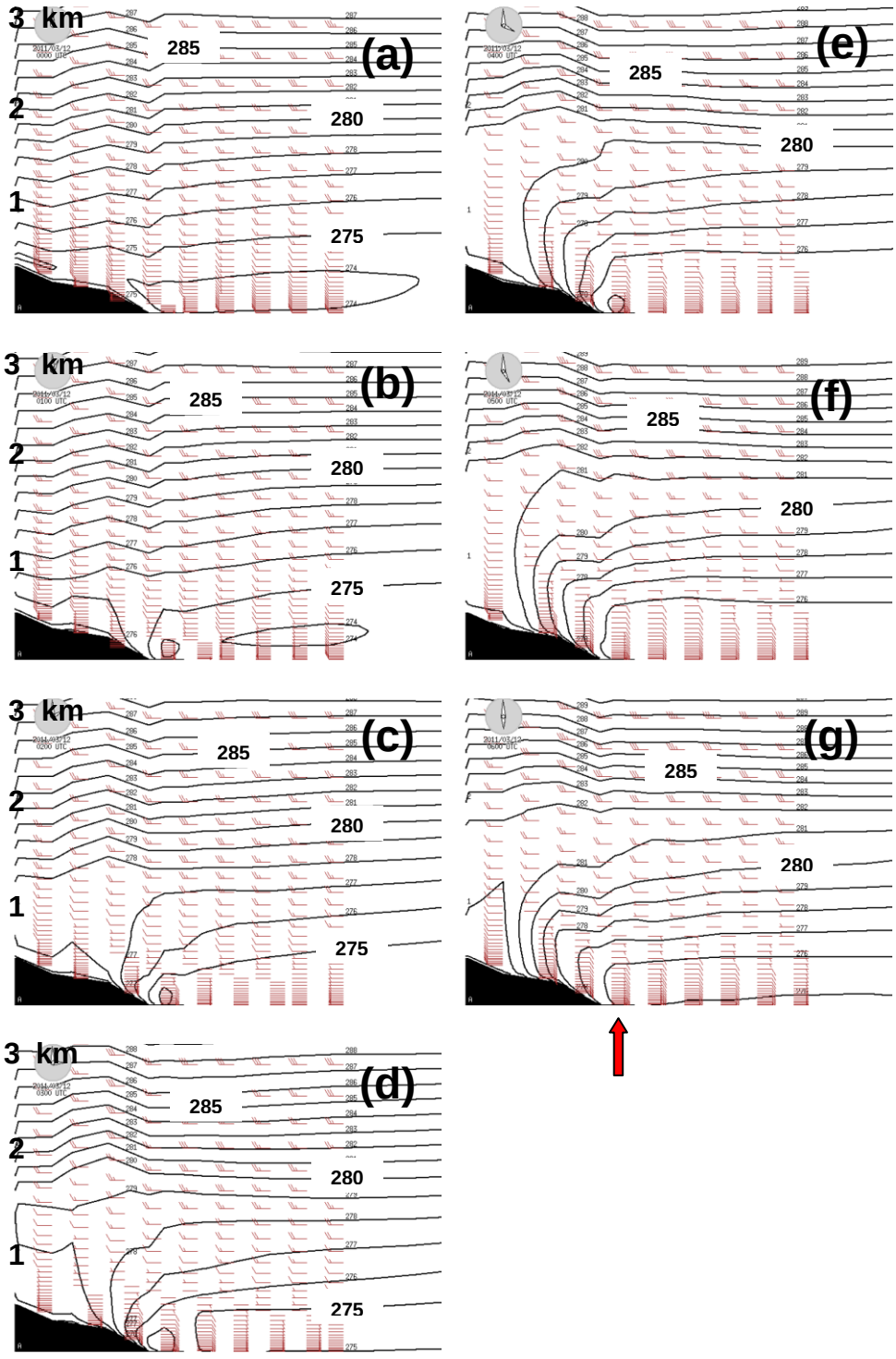

Figure 3.39 Hourly east-west cross section of potential temperature (K) and winds (knots) in the lowest 3 km through the accident site (red arrow) on 12 March. Cross section times as in Figure 3.38. Horizontal scale is approximately 70 km.

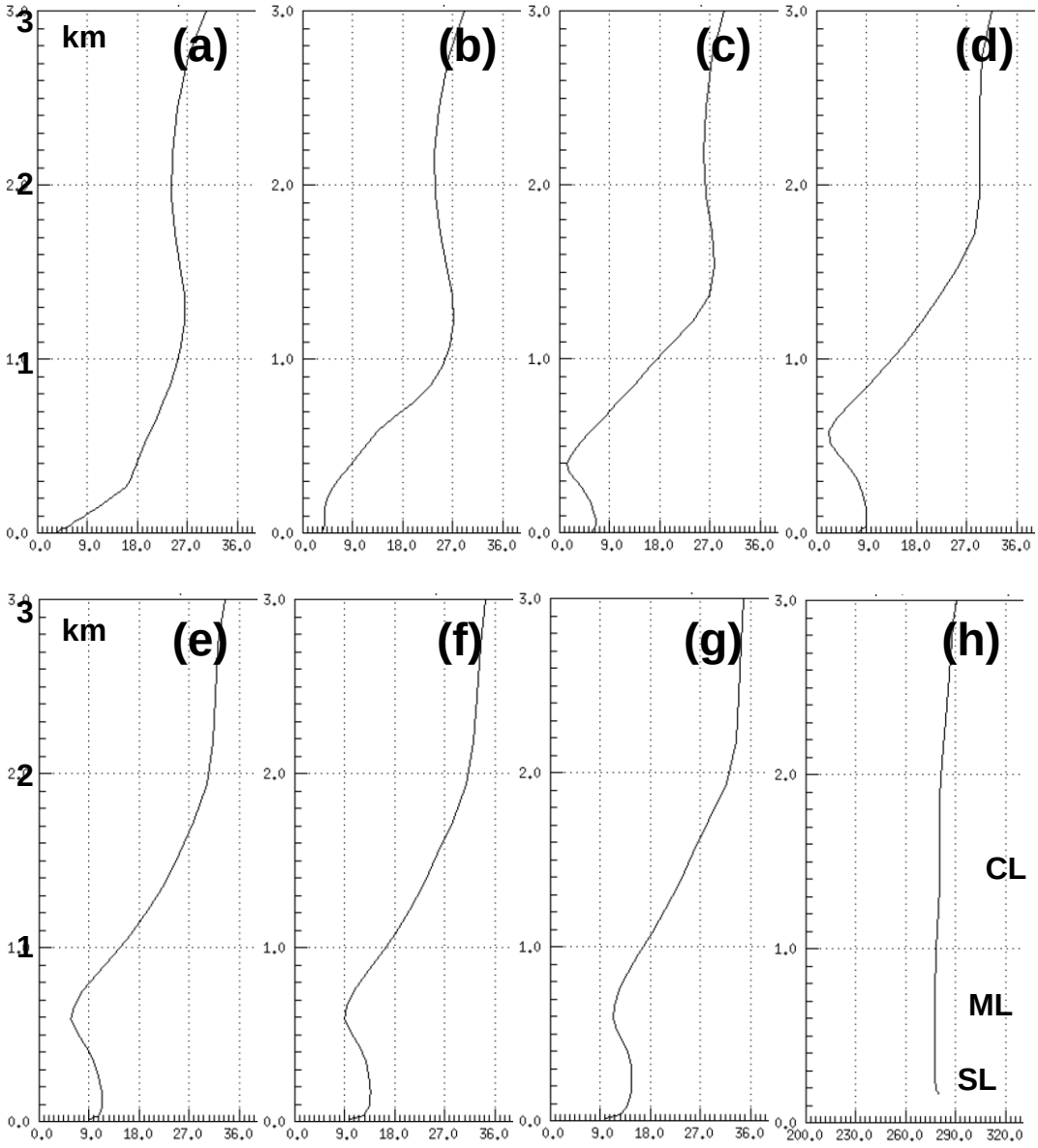

Figure 3.40 Hourly profiles of wind speed (knots) and virtual potential temperature (K) in the lowest 3 km over the accident site on 12 March. Wind profile times as in Figure 3.38. Virtual potential temperature profile at 04 UTC 12 March. Surface layer, mixed layer, and cloud layer are indicated by SL, ML, and CL, respectively.

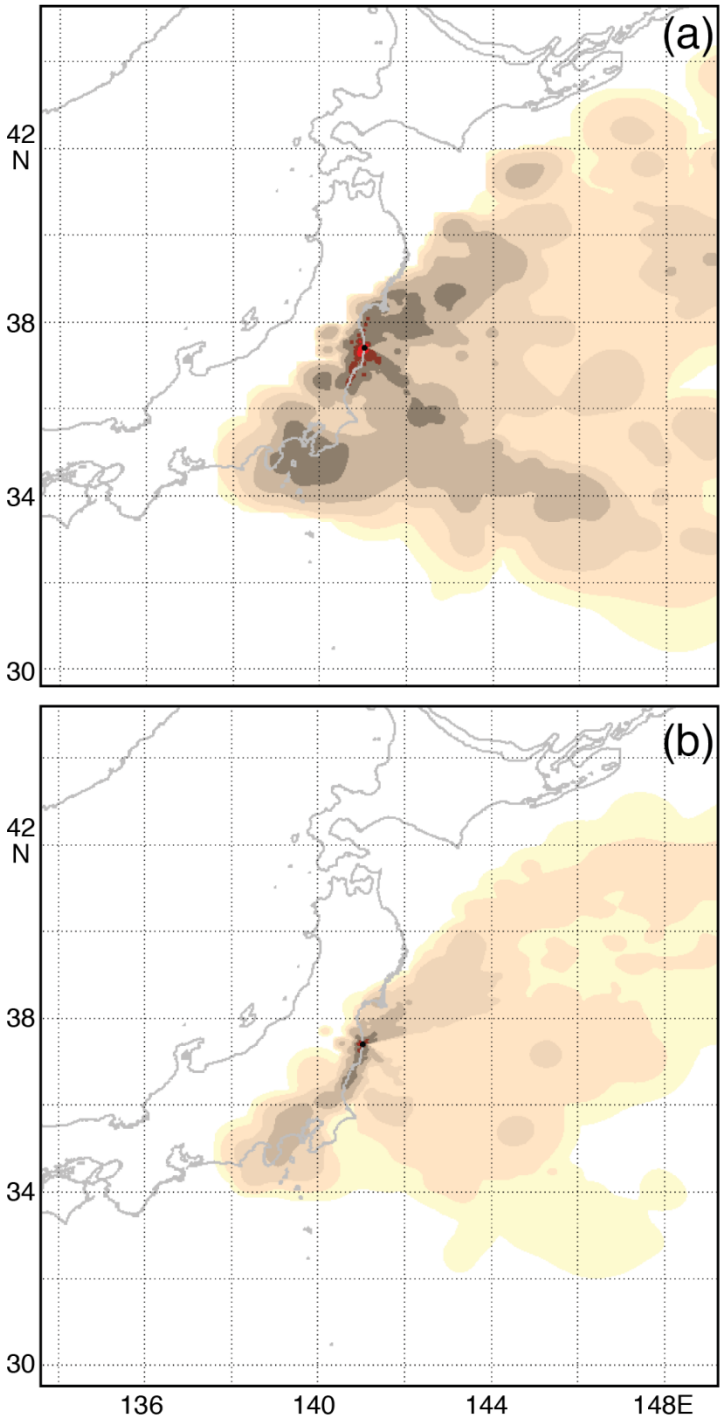

Figure 3.41 Cumulative surface deposition at 00 UTC 17 March 2011 due to dry deposition for (a) Stohl source term and (b) Terada source term for the cloud microphysics sensitivity. Contours intervals are 10^1, 10^2, 10^3, 10^4, 10^5, 10^6, 10^7 Bqm^{-2}. Black circle indicates the location of the Fukushima Daiichi nuclear power station.

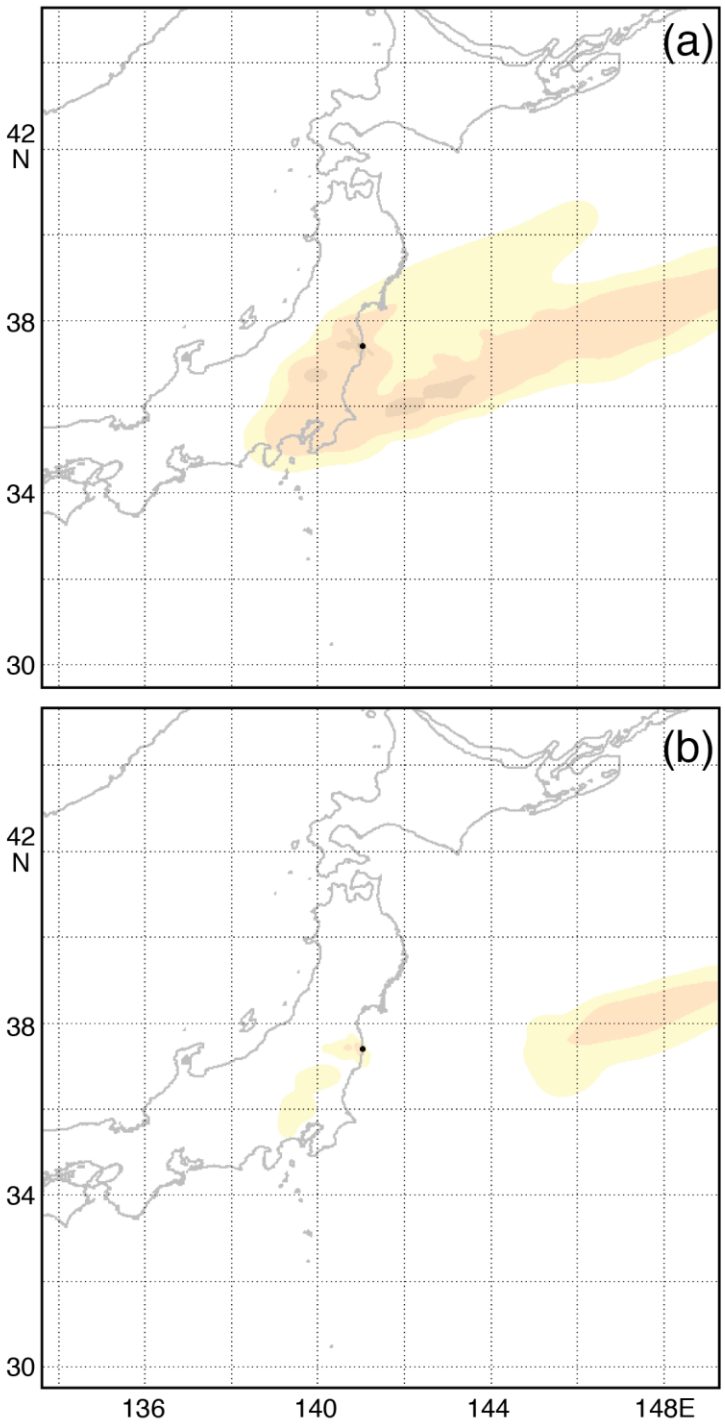

Figure 3.42 Cumulative surface deposition at 00 UTC 17 March 2011 due to wet deposition for (a) Stohl source term and (b) Terada source term for the cloud microphysics sensitivity. Contours intervals are 10^1, 10^2, 10^3, 10^4, 10^5, 10^6, 10^7 Bqm^{-2}. Black circle indicates the location of the Fukushima Daiichi nuclear power station.

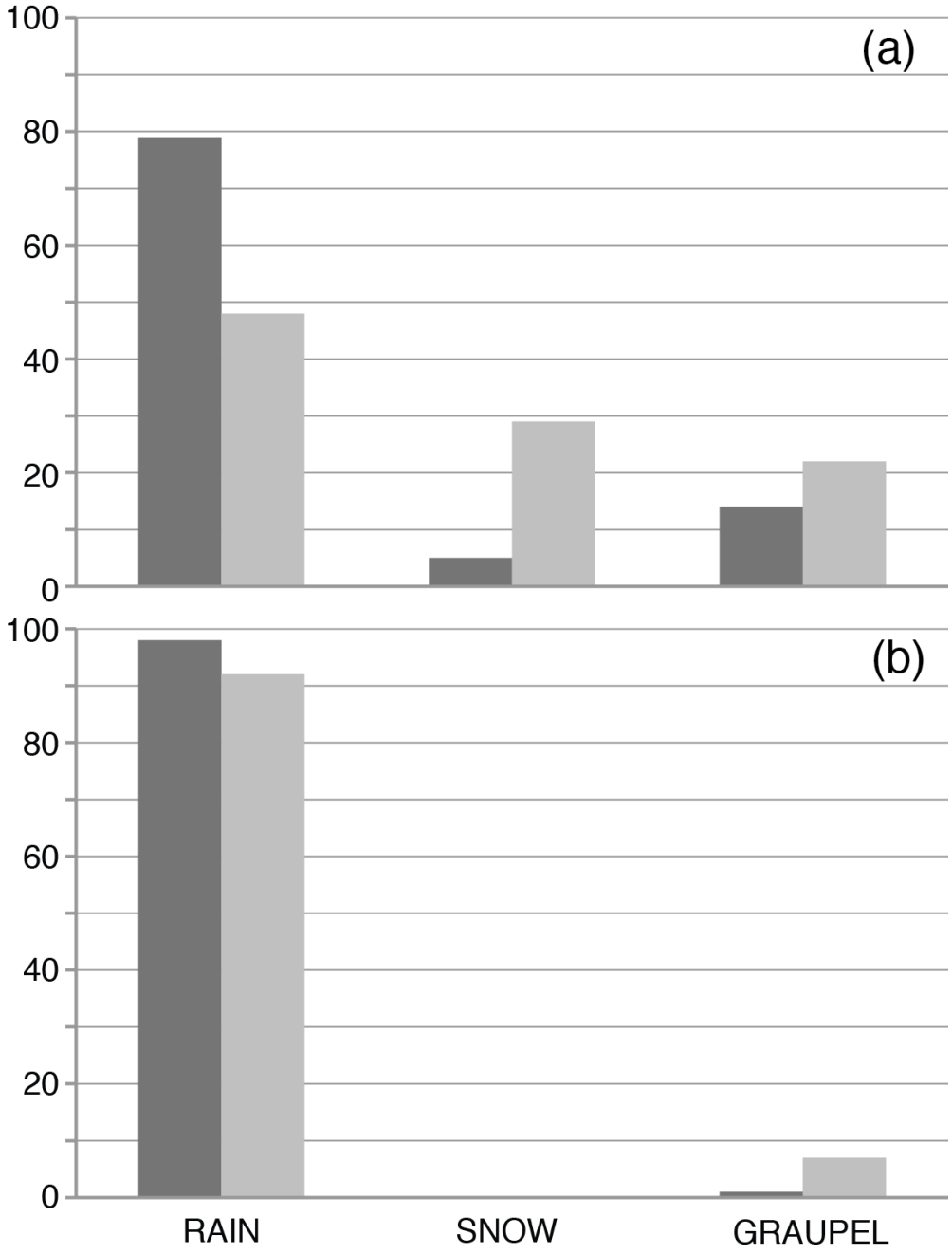

Figure 3.43 Percentage contributions of cumulative surface wet deposition at 00 UTC 17 March 2011 due to scavenging of ^{137}Cs by rain, snow, and graupel for the cloud microphysics sensitivity simulation (MMD = 0.5, σ_g = 1.5). Stohl source term (top) and Terada source term (bottom). Dark gray bar shows total radioactivity (Bq). Light gray bar shows total area (m^2).

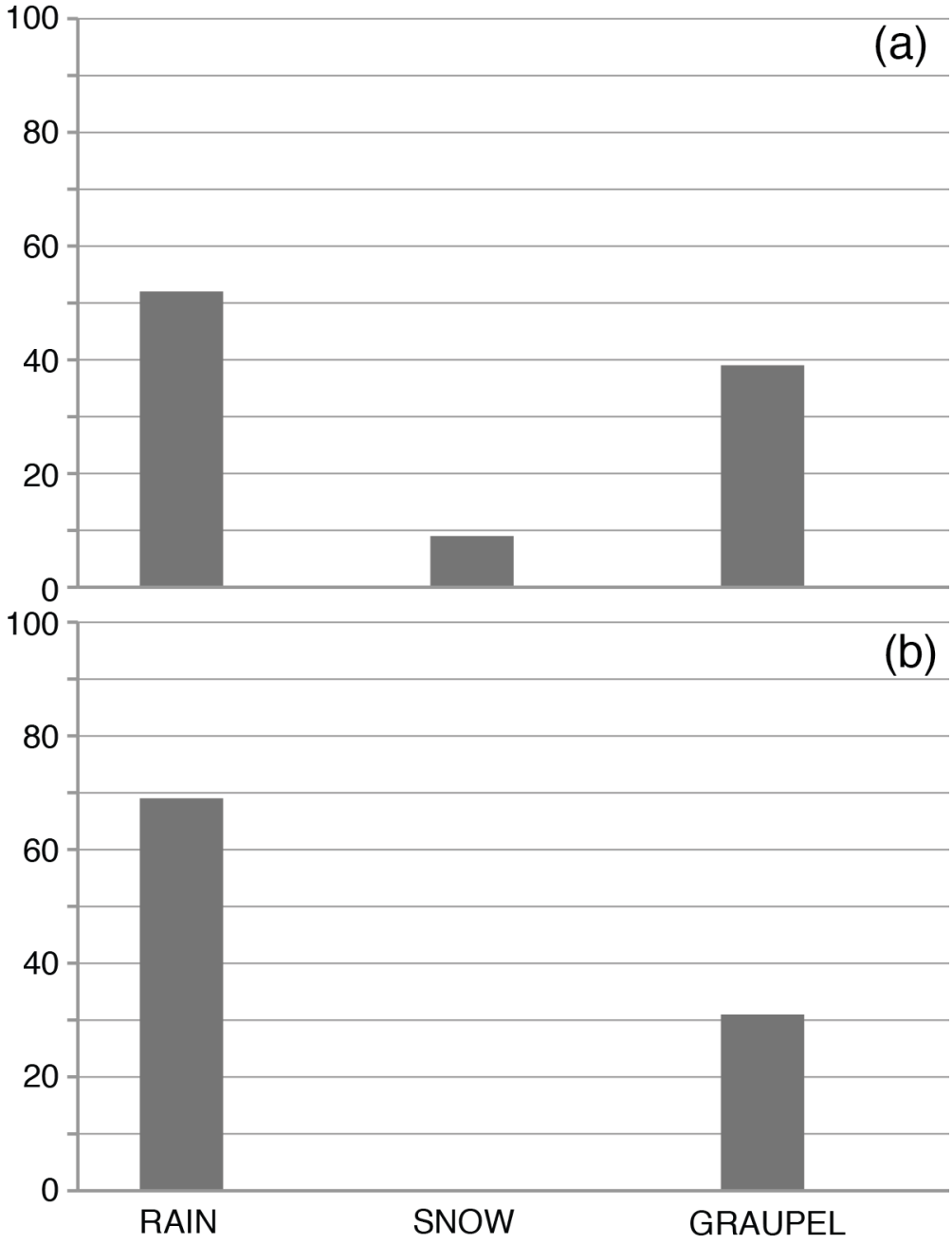

Figure 3.44 Percentage contributions of cumulative surface wet deposition (Bqm^{-2}) at 00 UTC 16 March 2011 on the NNSA aircraft grid due to scavenging of ^{137}Cs by rain, snow, and graupel for the cloud microphysics sensitivity simulation (MMD=0.5, σ_g= 1.5). Stohl source term (a) and Terada source term (b).

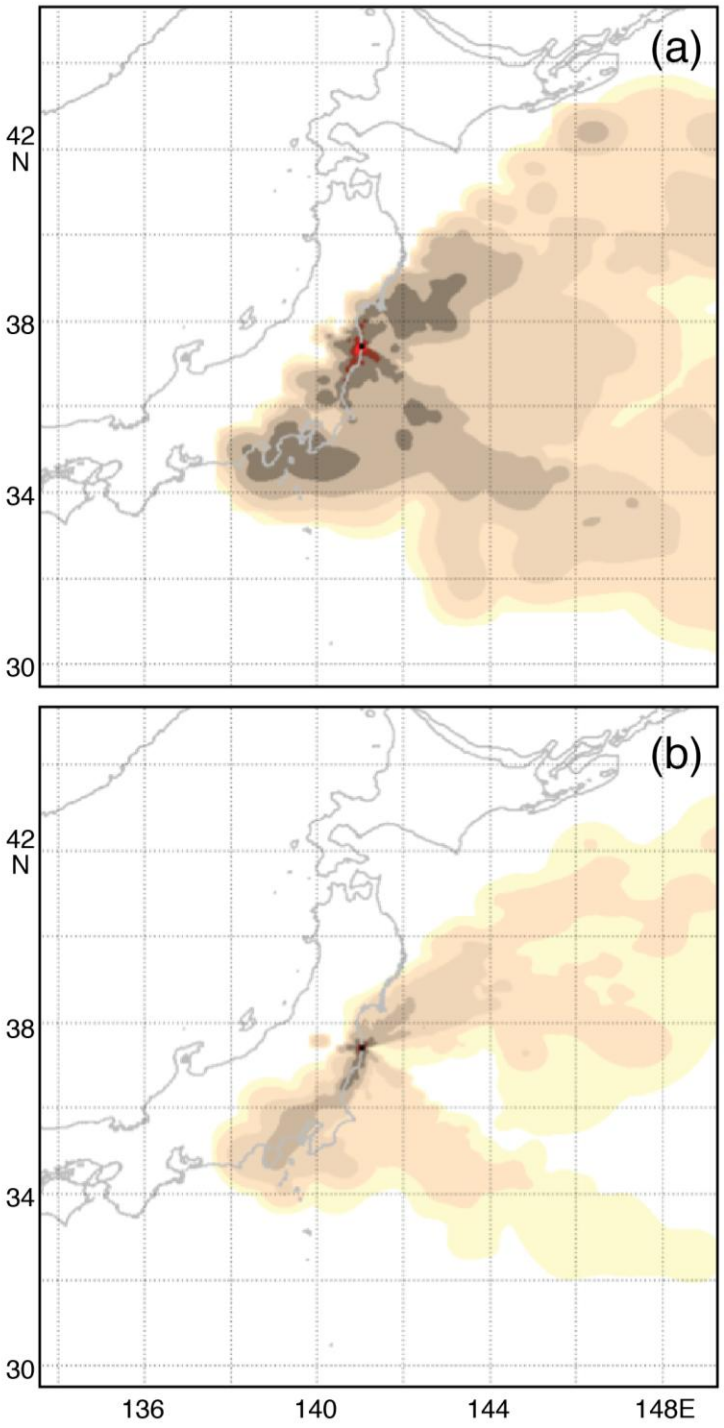

Figure 3.45 Cumulative surface deposition at 00 UTC 17 March 2011 due to dry deposition for (a) Stohl source term and (b) Terada source term for the explosion PSDE1 sensitivity. Contours intervals are 10^1, 10^2, 10^3, 10^4, 10^5, 10^6, 10^7 Bqm^{-2}. Black circle indicates the location of the Fukushima Daiichi nuclear power station.

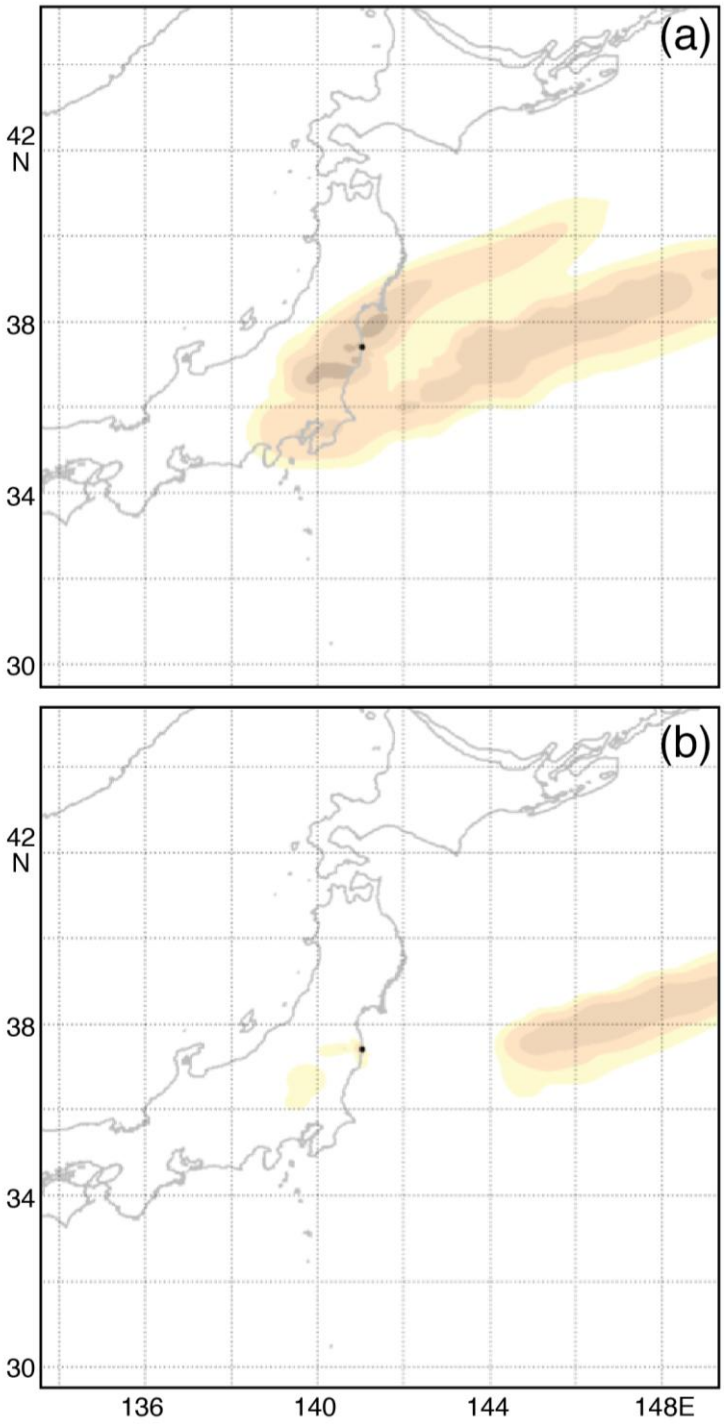

Figure 3.46 Cumulative surface deposition at 00 UTC 17 March 2011 due to wet deposition for (a) Stohl source term and (b) Terada source term (b) for the explosion PSDE1 sensitivity. Contours intervals are 10^1, 10^2, 10^3, 10^4, 10^5, 10^6, 10^7 Bqm^{-2}. Black circle indicates the location of the Fukushima Daiichi nuclear power station.

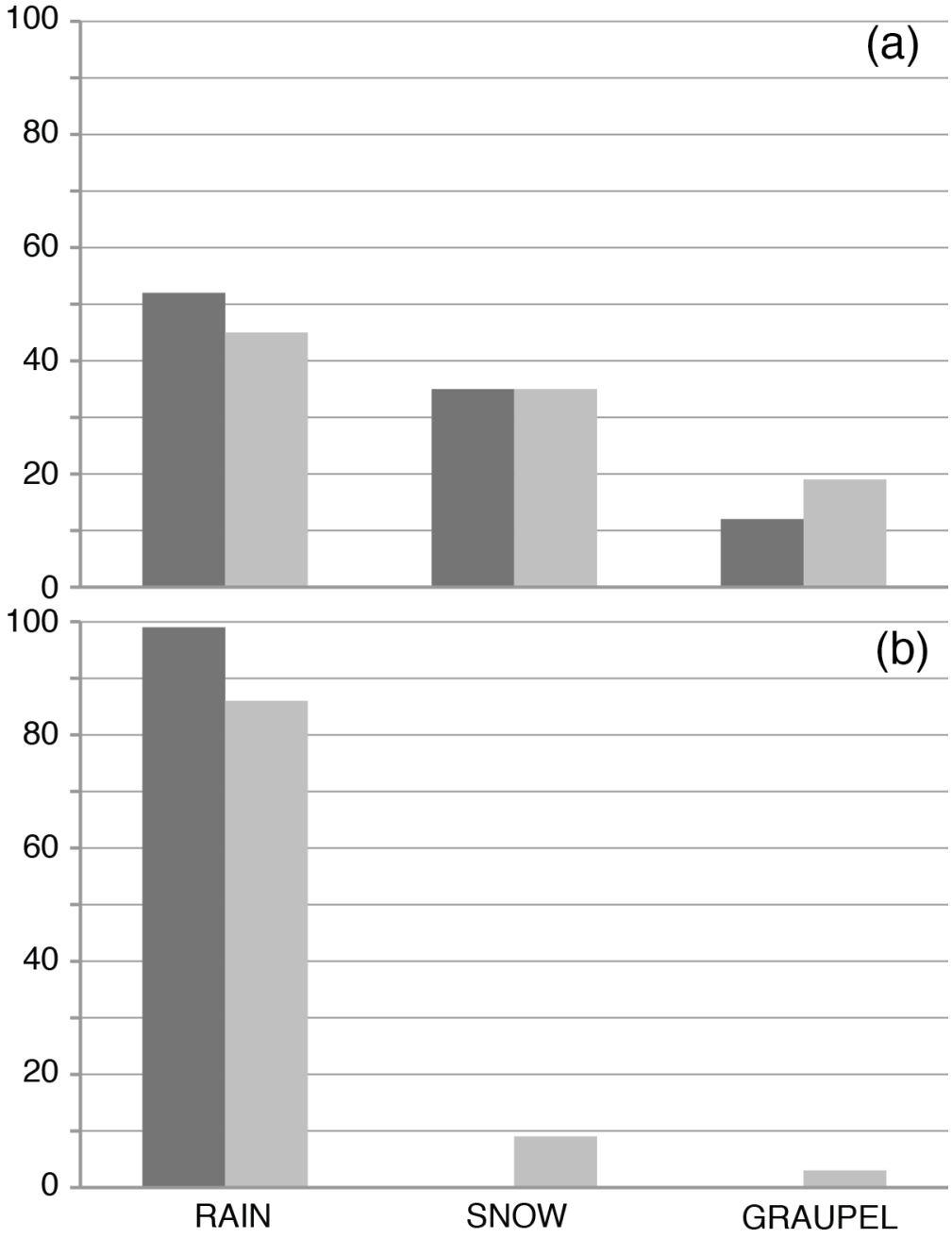

Figure 3.47 Percentage contributions of cumulative surface wet deposition at 00 UTC 17 March 2011 due to scavenging of ^{137}Cs by rain, snow, and graupel for the first explosion PSD sensitivity simulation (MMD=1.0, σ_g= 3.0). Stohl source term (a) and Terada source term (b). Dark grey bars show total radioactivity (Bq). Light grey bars show total area (m^2).

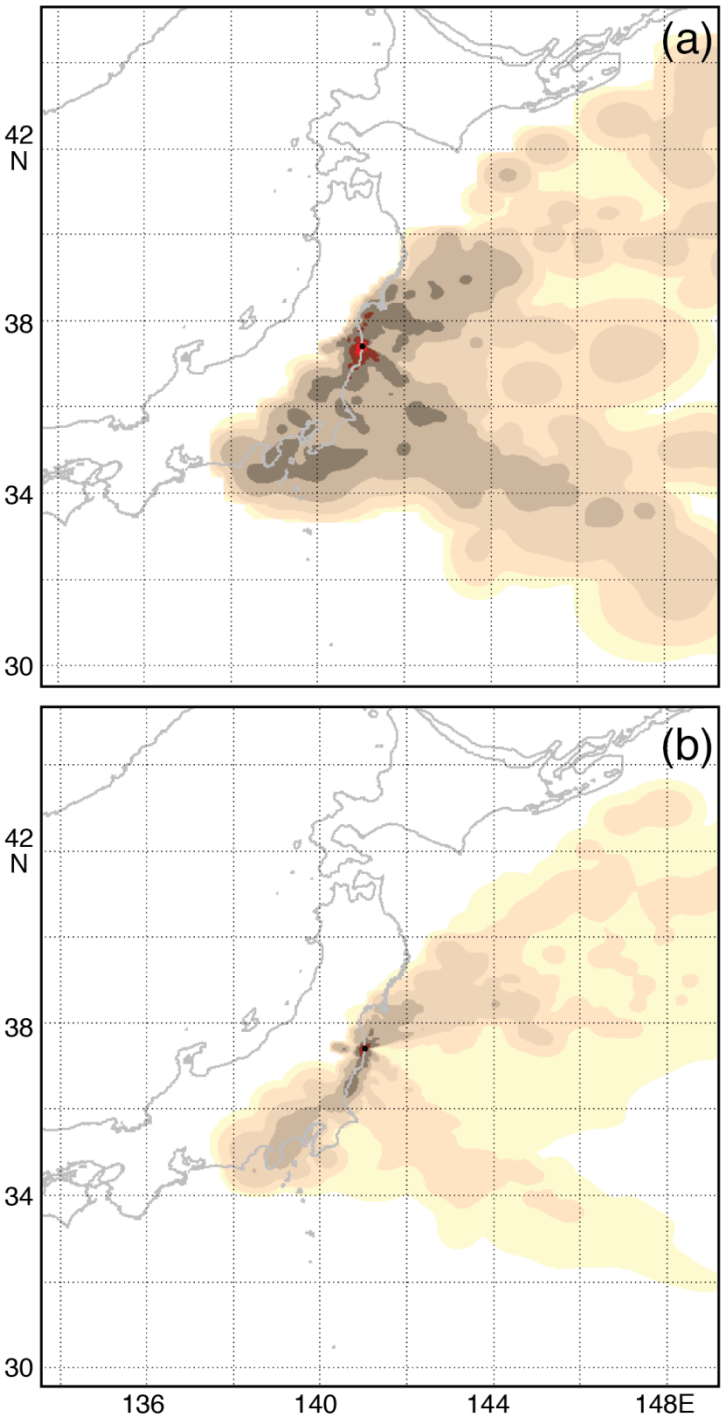

Figure 3.48 Cumulative surface deposition at 00 UTC 17 March 2011 due to dry deposition for (a) Stohl source term and (b) Terada source term for the explosion PSDE2 sensitivity. Contours intervals are 10^1, 10^2, 10^3, 10^4, 10^5, 10^6, 10^7 Bqm^{-2}. Black circle indicates the location of the Fukushima Daiichi nuclear power station.

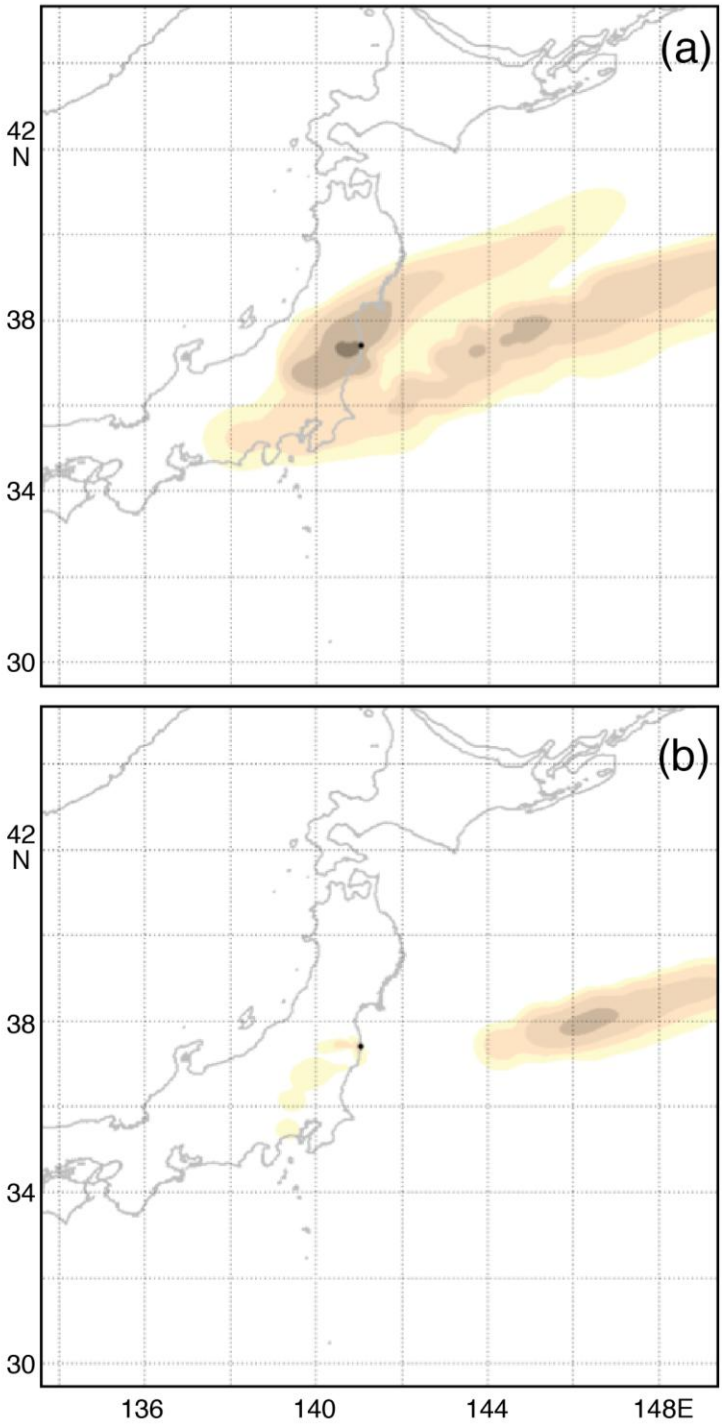

Figure 3.49 Cumulative surface deposition at 00 UTC 17 March 2011 due to wet deposition for (a) Stohl source term and (b) Terada source term for the explosion PSDE2 sensitivity. Contours intervals are 10^1, 10^2, 10^3, 10^4, 10^5, 10^6, 10^7 Bqm^{-2}. Black circle indicates the location of the Fukushima Daiichi nuclear power station.

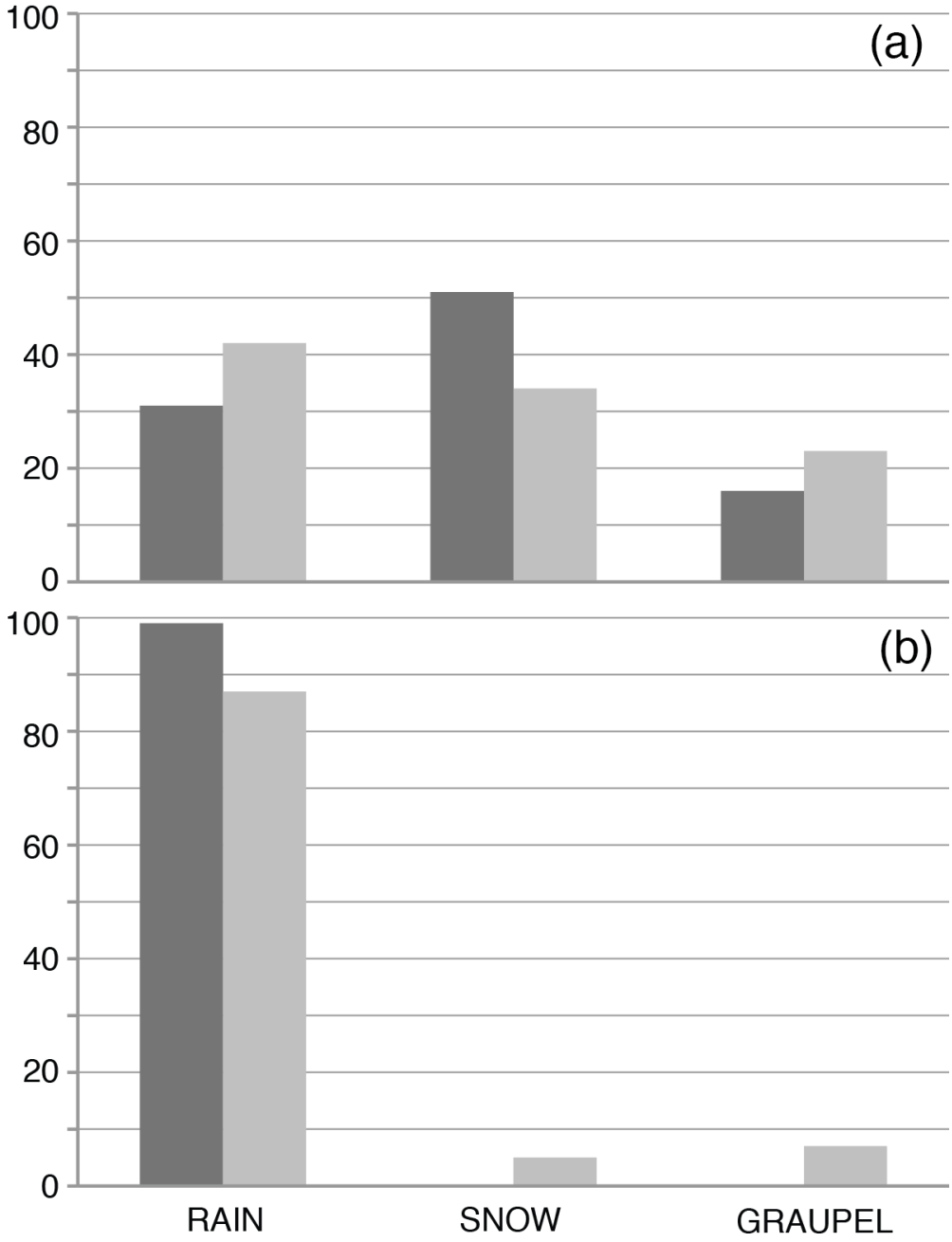

Figure 3.50 Percentage contributions of cumulative surface wet deposition at 00 UTC 17 March 2011 due to scavenging of ^{137}Cs by rain, snow, and graupel for the second explosion PSD sensitivity simulation (MMD=10.0, σ_g= 3.0). Stohl source term (a) and Terada source term (b). Dark grey bars show total radioactivity (Bq). Light grey bars show total area (m^2).

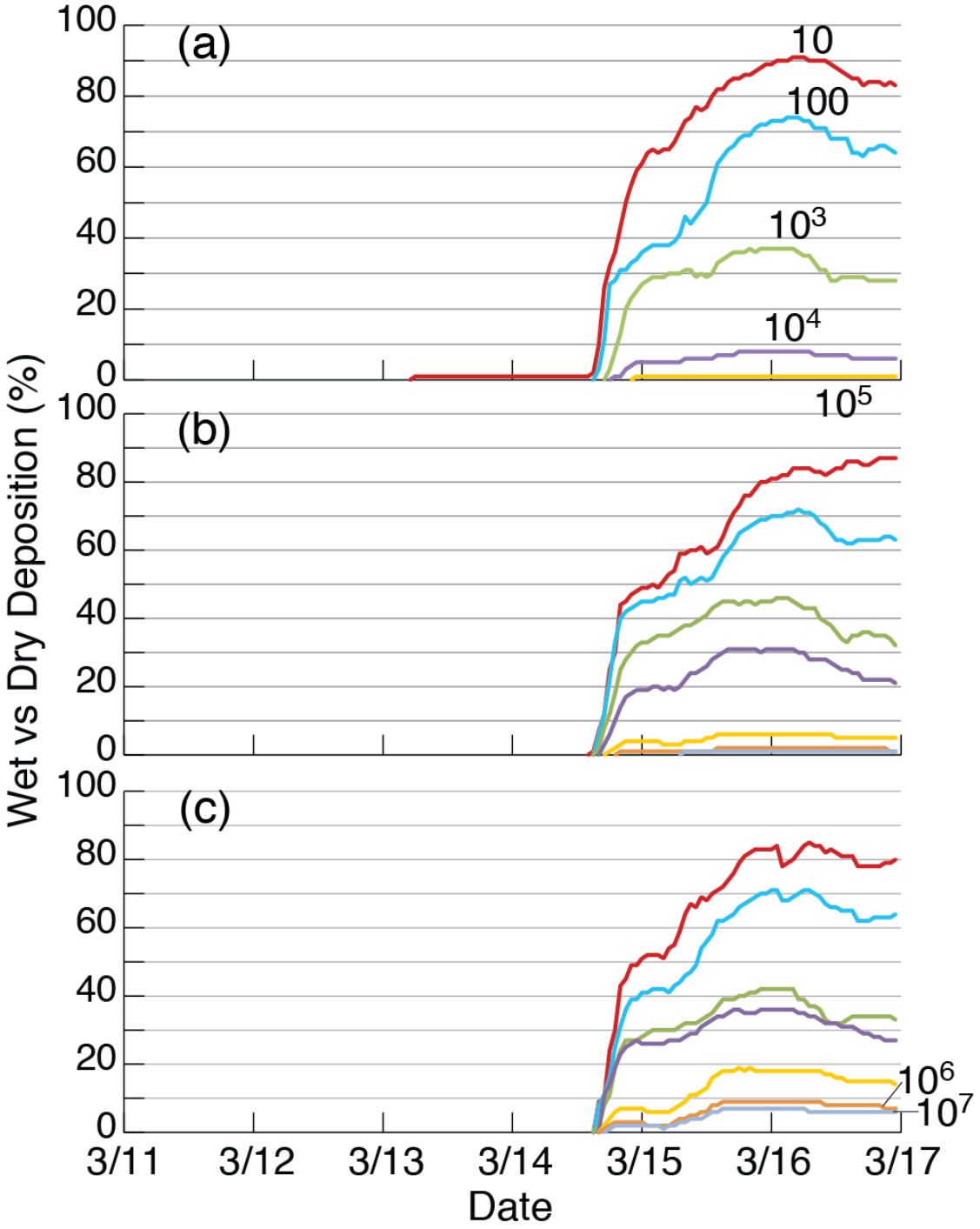

Figure 3.51 Percentage of wet vs. dry deposition with time for the Stohl source term for (a) no explosion, (b) PSDE1, and (c) PSDE2. Colored lines represent cumulative surface deposition thresholds for ^{137}Cs (Bqm^{-2}): 10^1 (red), 10^2 (blue), 10^3 (green), 10^4 (purple), 10^5 (yellow), 10^6 (orange), and 10^7 (gray).

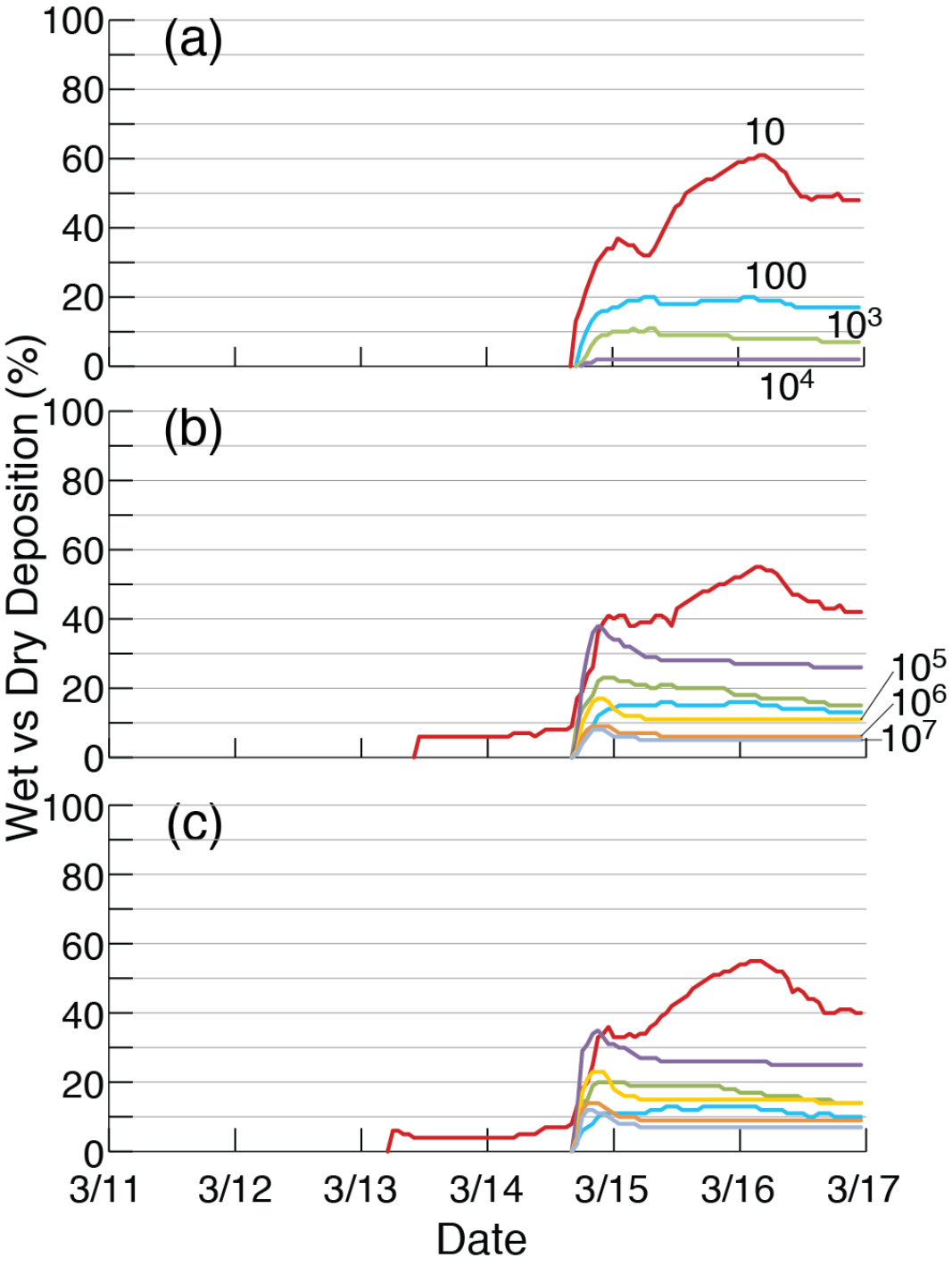

Figure 3.52 Percentage of wet vs. dry deposition with time for the Terada source term for (a) no explosion, (b) PSDE1, and (c) PSDE2. Colored lines represent cumulative surface deposition thresholds for ^{137}Cs (Bqm^{-2}): 10^1 (red), 10^2 (blue), 10^3 (green), 10^4 (purple), 10^5 (yellow), 10^6 (orange), and 10^7 (gray).

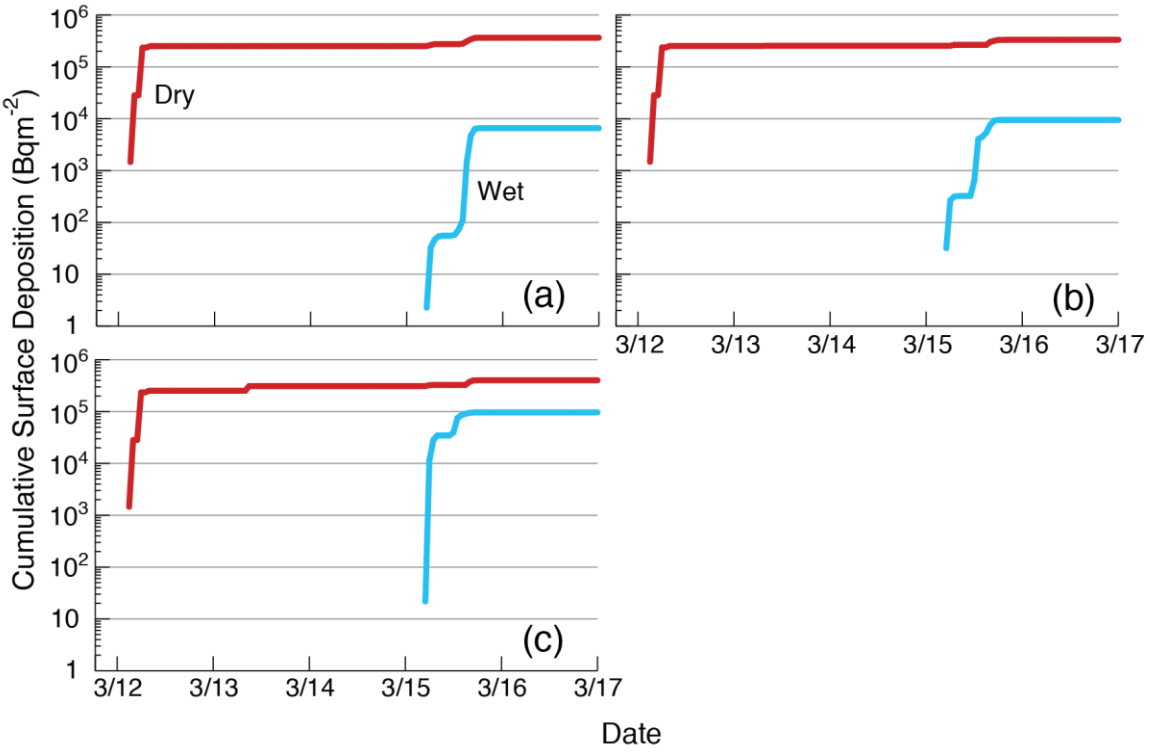

Figure 3.53 Cumulative wet and dry deposition (Bqm^{-}2) vs. time at the location of the NNSA observed surface deposition maximum (depicted by black triangle) on Transect T3 shown in figure 3.36c. Results are shown for the Stohl source term explosion PSD sensitivity study: (a) no explosion (MMD=0.5, σ_g= 1.5), (b) explosion PSDE1 (MMD=1.0, σ_g= 3.0), and (c) explosion PSDE2 (MMD=10.0, σ_g= 3.0). Red line indicates dry deposition. Blue line indicates wet deposition.

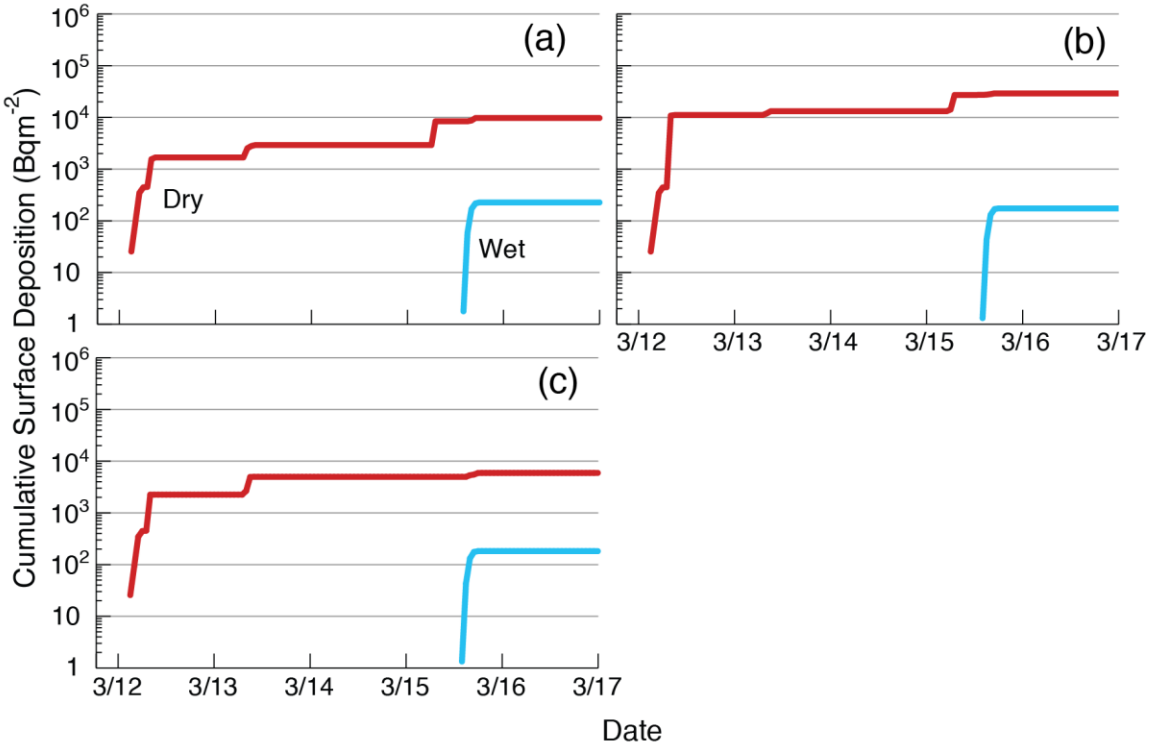

Figure 3.54 Cumulative wet and dry deposition (Bqm-2) vs. time at the location of the NNSA observed surface deposition maximum on Transect T3 shown in figure 3.36c. Results are shown for the Terada source term explosion PSD sensitivity study: (a) no explosion (MMD=0.5, σ_g= 1.5), (b) explosion PSDE1 (MMD=1.0, σ_g= 3.0), and (c) explosion PSDE2 (MMD=10.0, σ_g= 3.0). Red line indicates dry deposition. Blue line indicates wet deposition.

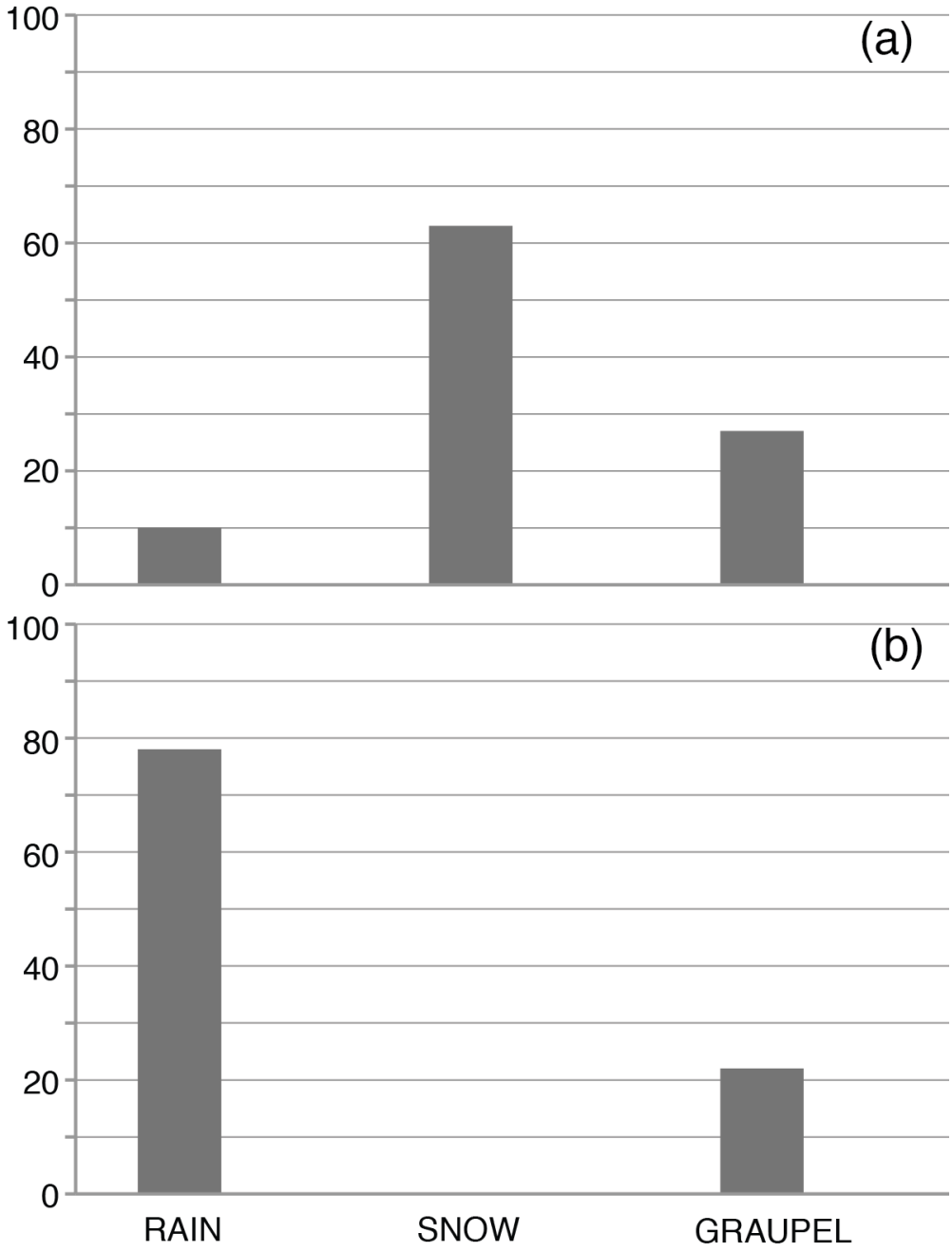

Figure 3.55 Percentage contributions of cumulative surface wet deposition (Bqm^{-2}) at 00 UTC 16 March 2011 on the NNSA aircraft grid due to scavenging of ^{137}Cs by rain, snow, and graupel for the first explosion PSD sensitivity simulation (MMD=1.0, σ_g= 3.0). Stohl source term (a) and Terada source term (b).

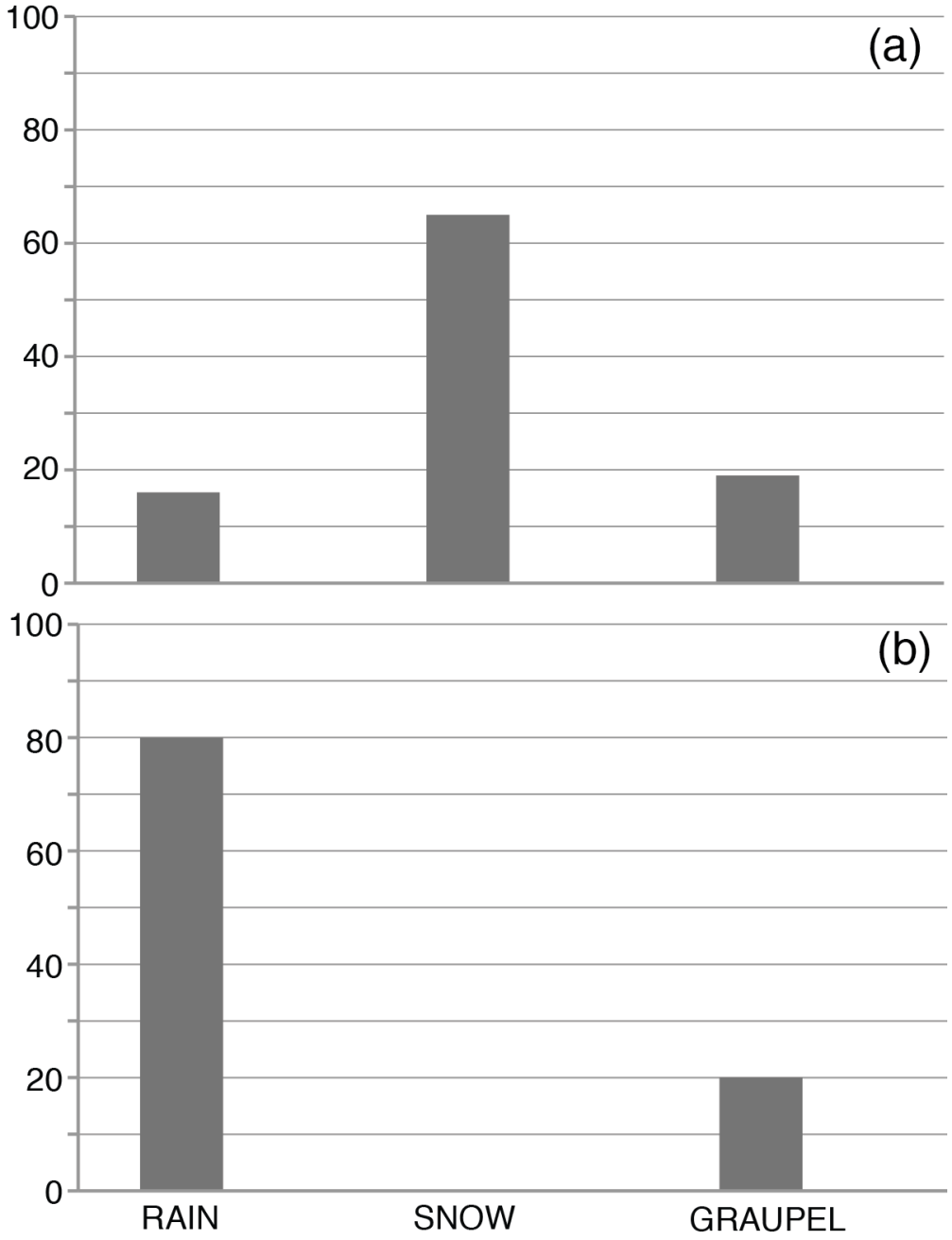

Figure 3.56 Percentage contributions of cumulative surface wet deposition (Bqm^{-2}) at 00 UTC 16 March, 2011 on the NNSA aircraft grid due to scavenging of ^{137}Cs by rain, snow, and graupel for the second explosion PSD sensitivity simulation (MMD=10.0, σ_g= 3.0). Stohl source term (a) and Terada source term (b).

CHAPTER 4. SUMMARY AND CONCLUSIONS

4.1 Discussion

Atmospheric releases of radioactive material represent a life-threatening hazard to local populations and the environment that must be predicted as accurately as possible. The release of radioactivity from the severe accident at the Fukushima Daiichi nuclear power station that resulted in widespread surface contamination provided the motivation for this research, with the goal of constructing an accurate model to predict and understand the dispersal hazards.

The primary objective of this research was to construct a coupled weather and dispersion modeling system and validation schema that can reproduce the observed pattern of surface contamination from the accident. A comparison of the observed deposition pattern of ^{137}Cs with the predicted cumulative surface wet and dry deposition patterns predicted shows that the model did a good job in simulating the deposition pattern during the dry phase of the accident (11 March–14 March) when dry deposition was the dominant removal process. In fact, the ability to model the dry deposition of the plume and the evolution of the surface wind field is key in predicting the surface deposition pattern that extends northwestward from the accident site.

It is suggested that the agreement with observations is because of the weather model's ability to simulate the extent and timing of onshore flow associated with a sea breeze circulation that developed around the time of the first reactor explosion since the observed pattern was predicted reasonably well with both source terms. An examination of the boundary layer structure during the period of onshore flow suggests that model

resolution of the underlying terrain may be a factor in the northward shift of the modeled surface deposition patterns compared with observations.

The magnitude of the modeled deposition pattern was also examined by comparing the observed and predicted surface deposition along four transects from the aircraft observations. The results showed that the OMEGA predictions were within an order of magnitude or better on portions of the transects that traversed the accident site, an additional distance downwind, and the observed maximum.

During the wet phase of the accident (15 March–16 March), the surface deposition pattern was not as well predicted. It is suggested that this discrepancy is because of differences between the model predicted and observed precipitation distributions. The model-simulated precipitation developed and moved through the area centered on and surrounding the accident site from 6 to 12 hours earlier than that shown by the observed precipitation distribution. This discrepancy resulted in widespread and diffuse surface deposition of radioactive material because the inland dispersing radioactive plumes interacted with the model precipitation fields over a broad area for a relatively longer period of time.

A second objective of this research was to compare the Terada and Stohl source terms results to determine if the simulated wet and dry deposition fields are sensitive to differences in the source specification. The results of the study show that the simulated surface deposition fields are sensitive to differences in the source terms.

On the synoptic scale, an analysis showed aerosol-bound ^{137}Cs from the Stohl source term, with emission heights at 50, 300, and 1000 meters AGL, was scavenged by rain (70%) and graupel (30%) compared with the Terada source term with emission

heights at 20 and 120 meters AGL in which material was scavenged preferentially by rain (95%). Conversely, on a local scale grid surrounding the accident that was fixed by the locations of aircraft observations, the aerosols from the Terada source term were scavenged by rain and graupel in roughly equal proportions.

Time series of the percentages of wet versus dry deposition predicted by the model showed a large spatial variability when segregated by threshold maximum surface deposition. At lower thresholds, wet deposition may account for up to 90% of the total deposited material. In contrast, dry deposition dominates wet deposition by up to two orders of magnitude when evaluated at higher thresholds due to relatively large amounts of dry deposited material near the accident site.

The Stohl source term released roughly a factor of seven more radioactive material than the Terada source term over the emission period of this study, and this is a controlling factor in this case on the extent of the surface deposition pattern. However, the distribution of the surface deposition is also sensitive to the PSD of the effluent, thus the ratio of scavenged material due to rain, snow, and graupel may be less skewed in other cases. A fraction of the additional material was postulated by Stohl et al. (2012) to have occurred through emissions from spent fuel pools. This aspect of the accident was not addressed in the formulation of the Terada source term and may be an important omission.

The Terada emission heights are relatively lower than the Stohl emission heights and the Terada explosive periods are significantly shorter than those used in the Stohl source term. These emission factors likely combine to skew the proportion of material that is scavenged by rain when using the Terada source term because aerosols are not

lofted in sufficient quantities to heights at which scavenging by frozen precipitation becomes important.

The third objective of this study comprised two sensitivity studies. The aim of the cloud microphysics study was to determine whether the use of a double-moment scheme was warranted for the wet phase of the accident. In general, results showed little sensitivity to the choice of scheme. However, given the weakly-forced and widespread, but relatively light precipitation that developed during the accident, this result could be due to the simplification of using the mass-mean diameter in the Slinn scavenging model in place of the full hydrometeor PSD predicted by the double-moment scheme. In addition, other precipitation cases involving relatively stronger forcing (e.g., convective storms, orographic lifting, frontal boundaries) may show more sensitivity to the complexity of the microphysics scheme used.

A second study investigated the sensitivity of the precipitation scavenging process to different choices of aerosol PSD, specifically to broadening the PSD during explosive periods. Results showed that precipitation scavenging using the Stohl source term was very sensitive to the explosion PSD compared with the Terada source term, which showed little sensitivity.

Results also showed that the percentage of wet versus dry deposition over time depends on the PSD used and on the threshold value of the cumulative surface deposition used to evaluate the percentage. For the PSDE1 and PSDE2 explosion cases, the percentage of wet deposition in the smaller threshold categories remains relatively unchanged for the Stohl and Terada source terms in contrast to the larger threshold categories that show small increases in the percentage of wet deposition over time.

This study is the first to compare the Terada and Stohl source terms using a common atmospheric modeling framework (i.e., use of identical weather simulations to drive the dispersion of different emissions estimates). Therefore, it is important to assess which source term produced the most realistic result.

The results of the present study point to the need for accurate emission heights in cases where precipitation scavenging is the dominant removal process because this parameter serves to differentiate the surface wet deposition patterns when rain, snow, and graupel are present. In this respect, the Stohl source term provides a more realistic result for this modeling study because the emission heights span the depth of the modeled boundary layer during the accident and thus the spectrum of mixed-phase precipitation observed during the accident. In contrast, the Terada source term releases material at relatively lower altitudes with the exception of explosive periods when emission heights are increased briefly, but only to the lower half of the modeled boundary layer height. Thus, the primary result of using a source term with relatively lower emission heights for the meteorological scenario accompanying the accident is that the surface wet deposition pattern is determined predominantly by rain instead of mixed-phase precipitation.

During the dry phase of the accident the Stohl source term yielded a better agreement with observations in terms of the surface dry deposition pattern. Given the demonstrated ability of the weather model to accurately predict the inland dispersion of the effluents, the relative amount of material released between the two source terms may be the deciding factor compared to the difference in emission heights for this phase of the accident. Also, on the basis of matching the observed surface pattern, as well as the better match to observations in the magnitude of deposited material along the analyzed aircraft

transects, the Stohl source term provided a more realistic result for this modeling study. However, an important consideration in making this distinction is the fact that the true amount of material released is currently unknown.

This study demonstrated the dominant role of dry deposition in predicting the observed surface pattern from the accident, but also highlighted the large spatial variability in the surface deposition due to precipitation scavenging. With respect to the phase of the accident during which dry deposition was the dominant removal process, the study showed both source terms to be useful in combination with an accurate weather and dispersion simulation. However, the Stohl source term produced more realistic results compared with observations. Modeling results for the wet phase of the accident underscore the need for better estimates of the time-varying emission heights for use in the dispersion model and point to the need for improvement in simulating the timing and distribution of the precipitation field in the weather model.

These aspects of the study have implications for modeling future incidents because the prediction of dispersal hazards from radioactive releases must include the capability to model wet and dry processes accurately given the random nature of accidents. This work presents a validated methodology to predict the dispersal of radioactive material that will be useful in providing critical guidance to government agencies dealing with emergency response and mitigation.

4.2 Future work

This study developed new analytical tools for the atmospheric dispersion of radioactive material that can be applied to future accidents. However, there are several

aspects of the study and models that can be improved in future works and provide new avenues for future research.

Decreasing the grid spacing in the weather model would improve the accuracy of the simulation results because it would help to further resolve the complex terrain in the vicinity of the Fukushima nuclear power plant and the evolving precipitation field. In addition, the simulation schema that was developed for this study would benefit from data assimilation that uses the OMEGA output as a first guess for each incremental leg of the atmospheric simulation to reduce spin-up in the model simulation.

With respect to the atmospheric dispersion model, there are aspects of the scavenging parameterization that could be improved. For example, in the current scheme when a particulate puff encounters precipitation that removes puff mass, the scavenged puff mass is deposited instantaneously on the surface. A more accurate parameterization would allow the scavenged puff mass to settle to the surface at a rate determined by the sedimentation of the precipitation field. Moreover, fully resolving the hydrometeor PSD instead of using the mass-mean diameter as a characteristic scavenging diameter may also improve the distribution of the surface wet deposition field. Other aerosol PSDs should be tested as the source term becomes more refined. Lastly, in-cloud scavenging by nucleation processes may help to predict the observed surface deposition patterns in areas of complex terrain and valleys where the occurrence of fog was more likely a factor in the scavenging process than rain, snow, or graupel.

The accuracy of the puff dispersion could be improved by the addition of a puff splitting and merging scheme, which would better resolve the atmospheric properties at the location of the puff centroid that characterize the influence of unresolved turbulence.

Finally, the addition of a first-principles capability for resolving momentum and buoyancy-dominated plume rise would improve the results by allowing the release height to vary according to the local meteorology rather than remain fixed over time. This is an important consideration since the use of a fixed release height is not physically coupled with the local meteorology, particularly the depth of the mixed layer.

The radioactive material released during the Fukushima accident was dispersed circumglobally over the Northern Hemisphere by the end of March 2011 through the action of the synoptic-scale flow. For example, radiation reached the Hawaiian Islands in trade wind flow after having been observed on the Pacific coast of the U.S. mainland. Because the OMEGA model can be configured as a global simulation, it would be of interest to continue the dispersion of the radioactive material over the Northern Hemisphere to gauge the utility of the model for the simulation of similar dispersal hazards such as volcanic eruption clouds and dust storms.

A high-resolution model validation study of the rapidly intensifying coast low pressure system that influenced the dispersal of the plume should be performed to further investigate the influence of the mixed-phase precipitation fields on the surface wet and dry deposition patterns observed during the accident. One focus of such a study should be the evolution of the melting layer and its effect on precipitation scavenging. Another focus should be the track, intensity, and timing of the development of the low pressure center near the coast.

Finally, the modeling system developed for this research will be applied to the validation datasets constructed for the Windscale and Chernobyl events to refine the methodology for use in future accident scenarios.

REFERENCES

Ahmad, N. N., D. P. Bacon, M. S. Hall, and R. A. Sarma, 2006: Application of the multidimensional positive advection transport algorithm (MPDATA) to environmental modeling on adaptive unstructured grids. *Int. J. Numer. Meth. Fluids,* **50,** 1247–1268.

Anthes, R. A., 1977: A cumulus parameterization scheme utilizing a one-dimensional cloud model. *Mon. Wea. Rev.,* **105,** 270–286.

ApSimon, H. M., A. J. H. Goddard, and J. Wrigley, 1985: Long-range atmospheric dispersion of radioisotopes-I: The MESOS model. *Atmos. Environ.,* **19,** 99–111.

ApSimon, H. M., and J. J. N. Wilson, 1987: Modeling atmospheric dispersion of the Chernobyl release across Europe. *Bound-Layer Meteor.*, **41,** 123–133.

Arnold, L., 1992: *Windscale 1957*. St. Martin's Press, 235 pp.

Arya, S. P., 1999: *Air Pollution Meteorology and Dispersion.* Oxford University Press, 310 pp.

Agency for Toxic Substances and Disease Registry, 1999: Toxicological profile for ionizing radiation. U.S. Department of Health and Human Services, 395 pp.

Agency for Toxic Substances and Disease Registry, 2004: Toxicological profile for cesium. U.S. Department of Health and Human Services, 244 pp.

Bacon, D. P., N. N. Ahmad, Z. Boybeyi, T. J. Dunn, M. S. Hall, P. C. S. Lee, R. A. Sarma, M. D. Turner, K. T. Waight, S. H. Young, and J. W. Zack, 2000: A dynamically adapting weather and dispersion model: The Operational Multiscale Environment model with Grid Adaptivity (OMEGA). *Mon. Wea. Rev.*, **128,** 2044–2076.

Bacon, D. P., N. N. Ahmad, T. J. Dunn, M. C. Monteith, and A. Sarma, 2008: An operational multiscale system for hazards prediction, mapping, and response. *Nat. Hazards,* **44,** 317–327.

Barad, M. L., 1958: Project Prairie Grass, a field program in diffusion, Vol. I. *Geophys. Res. Papers,* **59,** AFCRC-TR-58-235(I), U.S. Air Force Cambridge Research Center, 280 pp.

Berthet, S., M. Leriche, J.-P. Pinty, J. Cuesta, and G. Pigeon, 2010: Scavenging of aerosol particles by rain in a cloud resolving model. *Atmos. Res.,* **96,** 325–336.

Boybeyi, Z., N. N. Ahmad, D. P. Bacon, T. J. Dunn, M. S. Hall, P. C. S. Lee, and R. A. Sarma, 2001: Evaluation of the Operational Multiscale Environment Model with Grid Adaptivity against the European tracer experiment. *J. Appl. Meteor.,* **40,** 1541–1558.

Chamberlain, A. C., 1959: Deposition of iodine-131 in northern England in October 1957. *Q. J. R. Meteorol. Soc.,* **85,** 350–361.

Chate, D. M., P. S. P. Rao, M. S. Naik, G. A. Momin, P. D. Safai, and K. Ali, 2003: Scavenging of aerosols and their chemical species by rain. *Atmos. Environ.,* **37,** 2477–2484.

Chino, M., H. Nakayama, H. Nagai, H. Terada, G. Katata, and H. Yamazawa, 2011: Preliminary estimation of release amounts of ^{131}I and ^{137}Cs accidentally discharged from the Fukushima Daiichi nuclear power plant into the atmosphere. *J. Nucl. Sci. Technol.,* **48,** 1129–1134.

Clarke, R. H., 1974: An analysis of the 1957 Windscale accident using the WEERIE code. *Ann. Nucl. Sci. Eng.,* **1,** 73–82.

Cox, R. M., J. Sontowski, C. M. Dougherty, and J. C. Boutet, 2003: The use of diagnostic and prognostic wind fields for atmospheric transport calculations: An evaluation of the DIPOLE EAST 169 field experiment. *Meteorol. Appl.*, **10,** 151−164.

Crabtree, J., 1959: The travel and diffusion of the radioactive material emitted during the Windscale accident. *Q. J. R. Meteorol. Soc.,* **85,** 362−370.

De Cort, M., G. Dubois, Sh. D. Fridman, M. G. Germenchuk, Yu. A. Izrael, A. Janssens, A. R. Jones, G. N. Kelly, E. V. Kvasnikova, I. I. Matveenko, I. M. Nazarov, Yu. M. Pokumeiko, V. A. Sitak, E. D. Stukin, L. Ya. Tabachny, Yu. S. Tsaturov, and S. I. Avdyushin, 1998: Atlas of caesium deposition on Europe after the Chernobyl accident. EUR 16733 EN, European Commission, Luxembourg, 63 pp.

Draxler, R. R., and G. D. Hess, 1998: An overview of the HYSPLIT_4 modeling system for trajectories, dispersion, and deposition. *Aust. Meteor. Mag.*, **47,** 295−308.

Eisenbud, M., and T. Gesell, 1997: *Environmental Radioactivity from Natural, Industrial, and Military Sources.* Academic Press, 683 pp.

El-Hussein, A., and A. A. Ahmed, 1994: Activity size distribution of natural radionuclides. *Radiat. Phys. Chem.,* **44,** 99−101.

Englemann, R. J., and W. F. Wolff, 1990: Role of meteorology in emergency response. In: Kramer, M. L., and W. M. Porch (Eds.), *Meteorological Aspects of Emergency Response.* American Meteorological Society, Boston, MA, 5−14.

Evangeliou, N., Y. Balkanski, A. Cozic, and A. P. Moller, 2013: Simulations of the transport and deposition of ^{137}Cs over Europe after the Chernobyl nuclear power plant accident: influence of varying emission-altitude and model horizontal and vertical resolution. *Atmos. Chem. Phys.,* **13,** 7183−7198.

Feng, J., 2007: A three-mode parameterization of below-cloud scavenging of aerosols for use in atmospheric dispersion model. *Atmos. Environ.,* **41,** 6808–6822.

Garcia Nieto, P. J., B. Arganza Garcia, J. M. Fernandez Diaz, and M. A. Rodriguez, 1994: Parametric study of the selective removal of atmospheric aerosol by below-cloud scavenging, *Atmos. Environ.,* **28,** 2335–2342.

Gopalakrishnan, S. G., D. P. Bacon, N. N. Ahmad, Z. Boybeyi, T. J. Dunn, M. S. Hall, Y. Jin, P. C. S. Lee, D. E. Mays, R. V. Madala, R. A. Sarma, M. D. Turner, and T. R. Wait, 2002: An operational multiscale hurricane forecasting system. *Mon. Wea. Rev.,* **130,** 1830–1847.

Greenfield, S. M., 1957: Rain scavenging of radioactive particulate matter from the atmosphere. *J. Meteor.,* **14,** 115–125.

Grell, A. G., R. Knoche, S. E. Peckham, and A. S. McKeen, 2004: Online versus offline air quality modeling on cloud-resolving scales. *Geophys. Res. Lett.,* **31,** L16117.

Gudiksen, P. H., T. F. Harvey, and R. Lange, 1989: Chernobyl source term, atmospheric dispersion, and dose estimation. *Health Phys.,* **57,** 697–706.

Hanna, S. R., 1982: Applications in air pollution modeling. In: Nieuwstadt, F. T. M., and H. van Dop (Eds.), *Atmospheric Turbulence and Air Pollution Modelling.* D. Reidel Publishing Company, Dordrecht, the Netherlands, 275–310.

Heffter, J. L., A. D. Taylor, and G. J. Ferber, 1975: *A regional-continental scale transport, diffusion, and deposition model.* NOAA Technical Memorandum ERL ARL-50, Silver Spring, MD, 28 pp.

Hollingshead. A. T., S. Businger, R. Draxler, J. Porter, and D. Stevens, 2003: Dispersion modeling of the Kilauea plume. *Bound-Layer Meteor.,* **108,** 121–144.

Hsu, S. A., 1988: *Coastal Meteorology.* Academic Press, 260 pp.

Hsu, S. C., C. A. Huh, C. Y. Chan, S. H. Lin, F. J. Lin, and S. C. Liu, 2012: Hemispheric dispersion of radioactive plume laced with fission nuclides from the Fukushima nuclear event. *Geophys. Res. Lett.,* **39,** L00G22, doi:10.1029/2011GL049986.

Johnson, C. A., K. P. Kitchen, and N. Nelson, 2007: A study of the movement of radioactive material released during the Windscale fire in October 1957 using ERA40 data. *Atmos. Environ.,* **41,** 3921–3937.

Junge, C. E., 1963: *Air Chemistry and Radioactivity.* Academic Press, 382 pp.

Kalnay, E., 2003: *Atmospheric Modeling, Data Assimilation and Predictability.* Cambridge University Press, 341 pp.

Kaneyasu, N., H. Ohashi, F. Suzuki, T. Okuda, and F. Ikemori, 2012: Sulfate aerosol as a potential transport medium of radiocesium from the Fukushima nuclear accident. *Environ. Sci. Technol.,* **46,** 5720–5726.

Kaplan, M. L., C. S. Adaniya, P. J. Marzette, K. C. King, S. J. Underwood, and J. M. Lewis, 2009: The role of upstream midtropospheric circulations in the Sierra Nevada enabling leeside (spillover) precipitation. Part II: A secondary atmospheric river accompanying a midlevel jet. *J. Hydrometeor.,* **10,** 1327–1354.

Katata, G., M. Ota, H. Terada, M. Chino, and H. Nagai, 2012a: Atmospheric discharge and dispersion of radionuclides during the Fukushima Dai-ichi nuclear power plant accident. Part I: Source term estimation and local-scale atmospheric dispersion in early phase of the accident. *J. Environ. Radioact.,* **109,** 103–113.

Katata, G., H. Terada, H. Nagai, and M. Chino, 2012b: Numerical reconstruction of high dose rate zones due to the Fukushima Dai-ichi nuclear power plant accident. *J. Environ. Radioact.,* **111,** 2–12.

Kinoshita, N, K. Sueki, K. Sasa, J. Kitagawa, S. Ikarashi, T. Nishimura, Y.-S. Wong, Y. Satou, K. Handa, T. Takahashi, M. Sato, and T. Yamagata, 2011: Assessment of individual radionuclide distributions from the Fukushima nuclear accident covering central-east Japan. *Proc. Natl. Acad. Sci. USA,* **108,** 19526–19529.

Klug, W., G. Graziani, G. Grippa, D. Pierce, and C. Tassone, 1992: *Evaluation of Long Range Atmospheric Transport Models using Environmental Radioactivity Data from the Chernobyl Accident.* Elsevier, 366 pp.

Korsholm, U. S., A. Baklanov, A. Gross, and J. H. Sorensen, 2009: On the importance of the meteorological coupling interval in dispersion modeling during ETEX-1. *Atmos. Environ.,* **43,** 4805–4810.

Kramer, M. L., and W. M. Porch, 1990: Meteorological aspects of emergency response. In: Kramer, M. L., and W. M. Porch, (Eds.), 1990: *Meteorological Aspects of Emergency Response.* American Meteorological Society, Boston, MA, 1–4.

Lang, R., 1978: ADPIC−A three dimensional particle-in-cell model for the dispersal of atmospheric pollutants and its comparison to regional tracer studies. *J. Appl. Meteor.,* **17,** 320−329.

Lewellen, W. S., A. K. Varma, and Y. P. Sheng, 1983: Dry deposition model sensitivity. In: Pruppacher, H. R., R. G. Semonin, and W. G. N. Slinn (Eds.), *Precipitation Scavenging, Dry Deposition, and Resuspension. Vol. 2, Dry Deposition and Resuspension.* Elsevier, 859–870.

Lin, J. C., D. Brunner, and C. Gerbig, 2011: Studying atmospheric transport through Lagrangian models. *EOS,* **92,** 177–178.

Lin, Y.-L., R. D. Farley, and H. D. Orville, 1983: Bulk parameterization of the snow field in a cloud model. *J. Climate Appl. Meteor.,* **22,** 1065–1092.

Loosmore, G. A., and R. T. Cedarwall, 2004: Precipitation scavenging of atmospheric aerosols for emergency response applications: Testing an updated model with new real-time data. *Atmos. Environ.,* **38,** 993–1003.

Milbrandt, J., and R. McTaggart-Cowan, 2008: An efficient semi-double-moment microphysics scheme for operational applications. Presented at the WMO Cloud Modeling Workshop, Cozumel, Mexico, 14–17 July 2008.

Milbrandt, J. K., and M. K. Yau, 2005: A multimoment bulk microphysics parameterization. Part II: A proposed three-moment closure and scheme description. *J. Atmos. Sci.,* **62,** 3051–3064.

Minty, B. R. S., 1997: Fundamentals of airborne gamma-ray spectrometry. *J. Aust. Geol. & Geophys.* **17,** 39–50.

Nuclear Energy Agency, 2002: Chernobyl: Assessment of radiological and health impacts. 2002 update of Chernobyl: Ten years on. Vol. 3, No. 1, Report 230, OECD, 155 pp.

Nuclear Energy Agency, 2009: State-of-the-art report on nuclear aerosols. Nuclear Energy Agency Committee on the Safety of Nuclear Installations, NEA/CSNI/R(2009)5, 388 pp.

Nuclear Regulatory Commission, 2013: Glossary. U.S. Nuclear Regulatory Commission. [Available at http://www.nrc.gov/reading-rm/basic-ref/glossary.html.]

Pasquill, F., 1974: *Atmospheric Diffusion.* John Wiley & Sons, 429 pp.

Pielke, R. A., 2002: *Mesoscale Meteorological Modeling.* Academic Press, 676 pp.

Porter, J. N., and A. D. Clarke, 1997: Aerosol size distribution models based on in situ measurements. *J. Geophys. Res.*, **102,** 6035–6045.

Pruppacher, H. R., and J. D. Klett, 1980: *Microphysics of Clouds and Precipitation.* D. Reidel Publishing Company, 714 pp.

Pudykiewicz, J., 1988: Numerical simulation of the transport of radioactive cloud from the Chernobyl nuclear accident. *Tellus,* **40B,** 241–259.

Rogers, R. R., and M. K. Yau, 1989: *A Short Course in Cloud Physics.* Butterworth Heinemann, 290 pp.

Sarma, A., 2001: *Operational Multiscale Environment model with Grid Adaptivity (OMEGA); A User's Guide.* Science Applications International Corporation, McLean, VA, 74 pp.

Seinfeld, J. H., and S. N. Pandis, 2006: *Atmospheric Chemistry and Physics.* John Wiley & Sons, Inc., 1203 pp.

Skamarock, W. C., J. B. Klemp, J. Dudhia, D. O. Gill, D. M. Barker, M. G. Duda, X-Y. Huang, W. Wang, and J. G. Powers, 2008: A Description of the Advanced Research WRF Version 3. NCAR Technical Note NCAR/TN-475+STR, National Center for Atmospheric Research, Boulder, CO, 113 pp.

Slade, D. H. (Ed.), 1968: Meteorology and atomic energy−1968. USAEC/TID-24190, Oak Ridge, TN, 445 pp.

Slinn, W. G. N., 1984: Precipitation scavenging. In: Randerson, D. (Ed.), *Atmospheric Science and Power Production*, OSTI, DOE/TIC-27601, Oak Ridge, TN, 466–532.

Sportisse, B., 2007: A review of parameterizations for modeling dry deposition and scavenging of radionuclides. *Atmos. Environ.*, **41,** 2683–2698.

Stewart, N. G., and R. N. Crooks, 1958: Long-range travel of the radioactive cloud from the accident at Windscale. *Nature*, **182,** 627–628.

Stohl, A., C. Forster, A. Frank, P. Seibert, and G. Wotawa, 2005: Technical note: The Lagrangian particle dispersion model FLEXPART version 6.2. *Atmos. Chem. Phys.*, **5,** 2461–2474.

Stohl, A., P. Seibert, G. Wotawa, D. Arnold, J. F. Burkhart, C. Tapia, A. Vargas, and T. J. Yasunari, 2012: Xenon-133 and caesium-137 releases into the atmosphere from the Fukushima Dai-ichi nuclear power plant: Determination of the source term, atmospheric dispersion, and deposition. *Atmos. Chem. Phys.*, **12,** 2313–2343. doi:10.5194/acp-12-2313-2012.

Straka, J. M., 2009: *Cloud and Precipitation Microphysics, Principles and Parameterizations.* Cambridge University Press, 392 pp.

Stull, R. B., 1988: *An Introduction to Boundary Layer Meteorology.* Kluwer Academic Publishers, 670 pp.

Sykes, R. I., C. P. Cerasoli, and D. S. Henn, 1999: The representation of dynamic flow effects in a Lagrangian puff dispersion model. *J. Haz. Mat.*, **64,** 223–247.

Sykora, I., and K. Froehlich, 2009: Radionuclides as tracers of atmospheric properties. In: Froehlich, K. (Ed.), *Environmental Radionuclides. Tracers and Timers of*

Terrestrial Processes (Radioactivity in the Environment, Vol. 16). Elsevier, 432 pp.

Terada, H., G. Katata, M. Chino, and H. Nagai, 2012: Atmospheric discharge and dispersion of radionuclides during the Fukushima Dai-ichi nuclear power plant accident. Part I: Verification of the source term and analysis of regional-scale atmospheric dispersion. *J. Environ. Radioact.,* **112,** 141–154.

Twomey, S., 1977: *Atmospheric Aerosols.* Elsevier Publishing Company, 302 pp.

Uliasz, M., 1990: Development of the mesoscale dispersion modeling system using personal computers. Part I: Models and computer implementation. *Meteor. Z.,* **40,** 110–120.

United Nations Scientific Committee on the Effects of Atomic Radiation, 2008: Sources and effects of ionizing radiation. Report to the General Assembly with scientific annexes, Vol. II, Annex C, United Nations, Vienna, 44 pp.

U.S. Weather Bureau, 1955: *Meteorology and Atomic Energy.* USAEC, Washington, D.C., 160 pp.

Wang, P. K., 2002: *Ice Microdynamics.* Academic Press, 273 pp.

Warner, F., and R. M. Harrison (Eds.), 1993: *Radioecology after Chernobyl: Biogeochemical Pathways of Artificial Radionuclides.* John Wiley & Sons, 367 pp.

World Health Organization, 2012: Preliminary dose estimation from the nuclear accident after the 2011 Great East Japan Earthquake and Tsunami. World Health Organization, Geneva, 120 pp.

Wyngaard, J. C., 2010: *Turbulence in the Atmosphere.* Cambridge University Press, 393 pp.

Zhang, C, Y. Wang, and K. Hamilton, 2011: Improved representation of boundary layer clouds over the southeast Pacific in ARW-WRF using a modified Tiedtke cumulus parameterization scheme. *Mon. Wea. Rev.,* **139,** 3489–3513.